A&A 491, 131–156 (2008)
DOI: 10.1051/0004-6361:200809409

Astronomy & Astrophysics

Massive star formation in Wolf-Rayet galaxies⋆,⋆⋆

I. Optical and *NIR* photometric results

Á. R. López-Sánchez[1,2] and C. Esteban[1]

[1] Instituto de Astrofísica de Canarias, C/ vía Láctea S/N, 38200 La Laguna, Tenerife, Spain
[2] CSIRO / Australia Telescope National Facility, PO Box 76, Epping, NSW 1710, Australia
e-mail: Angel.Lopez-Sanchez@csiro.au

Received 17 January 2008 / Accepted 2 August 2008

ABSTRACT

Aims. We have performed a comprehensive multiwavelength analysis of a sample of 20 starburst galaxies that show the presence of a substantial population of massive stars. The main aims are the study of the massive star formation and stellar populations in these galaxies, and the role that interactions with or between dwarf galaxies and/or low surface companion objects have in triggering the bursts. In this series of papers, we present our new optical and near-infrared photometric and spectroscopic observations, and complete with data at other wavelengths (X-ray, far-infrared, and radio) available in the literature. In this paper, the first in the series, we analyze the morphology, stellar population age, and star-formation rate of each system.
Methods. We completed new deep optical and *NIR* broad-band images, as well as the new continuum-subtracted Hα maps, of our sample of Wolf-Rayet galaxies. We analyze the morphology of each system and its surroundings and quantify the photometric properties of all important objects. All data were corrected for both extinction and nebular emission using our spectroscopic data. The age of the most recent star-formation burst is estimated and compared with the age of the underlying older low-luminosity population. The Hα-based star-formation rate, number of O7V equivalent stars, mass of ionized gas, and mass of the ionizing star cluster are also derived.
Results. We found interaction features in many (15 up to 20) of the analyzed objects, which were extremely evident in the majority. We checked that the correction for nebular emission to the broad-band filter fluxes is important in compact objects and/or with intense nebular emission to obtain realistic colors and compare with the predictions of evolutionary synthesis models. The estimate of the age of the most recent star-formation burst is derived consistently. In general, the Hα-based star formation rate agrees with the estimates given by independent multiwavelength methods. With respect to the results found in individual objects, we remark the strong Hα emission found in IRAS 08208+2816, UM 420, and SBS 0948+532, the detection of a double-nucleus in SBS 0926+606A, a possible galactic wind in Tol 9, and one (two?) nearby dwarf star-forming galaxies surrounding Tol 1457-437.

Key words. galaxies: dwarf – galaxies: starburst – galaxies: photometry – galaxies: interactions – stars: Wolf-Rayet

1. Introduction

1.1. The nature of Wolf-Rayet galaxies

Wolf-Rayet (WR) galaxies are a subset of emission-line and H II galaxies, whose integrated spectra show broad emission features attributed to the presence of WR stars, indicating that a substantial population of this type of massive star exists in the ionized cluster(s) of the star-formation bursts. The most massive O stars ($M \geq 35\,M_{\odot}$ for $Z_{\odot}$) become WR stars around 2 and 3 Myr after their birth, spending only some few hundreds of thousands of years ($t_{\rm WR} \leq 10^6$ yr) in this phase (Maeder & Meynet 1994) until they explode as type Ib/Ic supernovae (van der Hucht 2001). The minimum stellar mass that an O star needs to reach the WR phase and its duration is dependent on metallicity. There are two important broad features that reveal the presence of WR stars: the so-called blue WR bump (between 4650–4690 Å) and the red WR bump (basically formed by the C IV λ5808 emission line). The broad, stellar, He II λ4686 is the main feature of the blue WR bump. The narrow, nebular He II λ4686 is usually associated with the presence of these massive stars, although it is rarely strong and its origin remains controversial (Garnett et al. 1991; Garnett 2004).

The detection of WR features in the spectrum of a starburst galaxy constrains the parameters that characterize the star-formation burst: the initial mass funtion must be extended to higher masses; the WR/O ratio is relatively large and the burst must therefore be short; and the time elapsed since the last starburst episode occurred must be less than a few Myr. Therefore, WR galaxies offer the opportunity to study an approximately coeval sample of very young starbursts (Schaerer & Vacca 1998).

The blue compact dwarf galaxy He 2–10 was the first object in which WR features were detected (Allen et al. 1976). Osterbrock & Cohen (1982) and Conti (1991) introduced the concept of a WR galaxy, to be *a galaxy whose integrated spectrum has detectable WR broad stellar emission lines emitted*

⋆ Based on observations made with NOT (Nordic Optical Telescope) and INT (Isaac Newton Telescope) operated on the island of La Palma jointly by Denmark, Finland, Iceland, Norway and Sweden (NOT) or the Isaac Newton Group (INT) in the Spanish Observatorio del Roque de Los Muchachos of the Instituto de Astrofísica de Canarias. Based on observations made at the Centro Astronómico Hispano Alemán (CAHA) at Calar Alto, operated by the Max-Planck Institut für Astronomie and the Instituto de Astrofísica de Andalucía (CSIC).
⋆⋆ Tables 2–7, Figs. 1, 2, 4, 6, 8, 10, 12, 14, 16, 18, 20, 22, 24, 26, 28, 30, 32, 33, 35 and Appendices are only available in electronic form at http://www.aanda.org

by unresolved stellar clusters. Kunth & Joubert (1985) performed the first systematic search for WR features in emission-line galaxies: in their sample of 45 extragalactic H II regions they classified 17 as WR galaxies. Kunth & Schild (1986) and Dinerstein & Shields (1986) reported the first detections of the red WR bump. Conti (1991) compiled the first WR catalogue, including 37 objects. Vacca & Conti (1992) developed the first quantitative scheme to estimate WR populations in starbursts using new quality data. The majority of detections of WR features have however been accidental, and have occurred in studies that cover a wide range of topics, from the determination of the primordial He abundance (Kunth & Sargent 1983; Kunth & Joubert 1985; Izotov et al. 1994; Izotov et al. 1997b; Izotov & Thuan 1999; Izotov & Thuan 1998; Thuan et al. 1995), the nature of Seyfert galaxies (Heckman et al. 1997), and starbursts with strong galactic winds (Allen et al. 1976). Guseva et al. (2000) analyzed a sample of 39 objects with heavy element abundances ranging from $Z_{\odot}/50$ to 2 $Z_{\odot}$ and obtained global results for WR galaxies. Buckalew et al. (2005) compared the properties of young star clusters with and without WR stars.

The most recent catalogue of WR galaxies was compiled by Schaerer et al. (1999) and listed 139 members, although this number has since increased (Popescu & Hopp 2000; González-Delgado et al. 2001; Bergvall & Östlin 2002; Contini et al. 2002; Pindao et al. 2002; Lípari et al. 2003; Tran et al. 2003; Fernandes et al. 2004; Izotov et al. 2004; Pustilnik et al. 2004; Jamet et al. 2004; Thuan & Izotov 2005), and these galaxies have even been detected at high z (Villar-Martín et al. 2004). In a study of emission-line galaxies extracted from the Sloan Digital Sky Survey (York et al. 2000) WR features were identified in many star-forming galaxies (Kniazev et al. 2004; Zhang et al. 2007), increasing the number of known WR galaxies to more than 300.

Morphologically, WR galaxies constitute an inhomogeneous class of star-forming objects. They are detected in irregular galaxies, blue compact dwarf galaxies (BCDGs), spiral galaxies (or, more precisely, giant H II regions in the arms of spiral disks), luminous, merging IRAS galaxies, active galactic nuclei (AGNs), and Seyfert 2 and low-ionization nuclear emission-line regions (LINERs) galaxies. Quoting Schaerer et al. (1999), the minimum common property of all WR galaxies is *ongoing or recent star formation that has produced stars sufficiently massive to evolve to the WR stage*.

We note that the definition of WR galaxy is *dependent of the quality of the spectrum, and location and size of the aperture*. The term WR galaxy must therefore be used with caution. The presence of WR features in the spectrum of a starburst *does not* imply that WR stars are present at all locations, but only that a significant population of this type of massive star exits inside the galaxy. Depending on the distance of the object and size of the area analyzed, the region of concern may be a single extragalactic H II region with a few WR stars in a galaxy, a massive star cluster or the nucleus of a powerful starburst galaxy harbouring numerous massive stars (Schaerer et al. 1999). The precise locations of the WR stars usually remain unknown, apart from for the Local Group or other nearby galaxies. The width of the extraction aperture for which the spectrum is extracted can sometimes be too large and the weak WR features diluted by the continuun flux. Furthermore, a starburst galaxy with several star-forming bursts may only show WR features in one of them. Aperture effects and the slit position can therefore play an important role in the detection of WR features (Huang et al. 1999; López-Sánchez et al. 2004a,b; Buckalew et al. 2005; López-Sánchez et al. 2006).

1.2. Aims of this paper series

In dwarf galaxies, starburst phenomena cannot be explained by the wave-density theory because of their low masses, and an alternative mechanism must operate. A proposed alternative mechanism for large-scale starburst formation is gas compression by shocks due to mass loss by means of galactic winds and the subsequent cooling of the medium (Thuan 1991; Hirashita 2000). Other authors however proposed galaxy interactions as a massive-star formation triggering mechanism (Sanders et al. 1988). Interactions appear to play a fundamental role triggering starbursts, both in spiral (Koribalski 1996; Kennicutt 1998), and dwarf and irregular galaxies. In these cases, interactions with nearby giant galaxies are unusual (Campos-Aguilar et al. 1993; Telles & Terlevich 1995), but with low surface-brightness galaxies (Wilcots et al. 1996; Noeske et al. 2001) or H I clouds (Taylor et al. 1996; Thuan et al. 1999; van Zee et al. 2001). Studying a sample of WR galaxies, Méndez (1999) performed an analysis of 13 objects extracted from the catalogue of Conti (1991), finding that 7 are clearly interacting and another 4 show features of interactions. For example, he found a bridge between two galaxies in Zw 0855+06 (Méndez et al. 1999a), prominent tidal tails in Mkn 8 (Esteban & Méndez 1999), star-formation activity induced by an H I cloud in Mkn 1094 (Méndez et al. 1999b) and an intermediate-age merger in Tol 35 (Méndez & Esteban 1999). For the first time, these facts enabled Méndez & Esteban (2000) to suggest that interactions with or between dwarf objects could be the main star-formation triggering mechanism in dwarf galaxies. These authors also noted that the interacting and/or merging nature of WR galaxies can be detected only when both deep, high-resolution images and spectra are available.

Subsequent works (Iglesias-Páramo & Vílchez 2001; Verdes-Montenegro et al. 2001, 2002; Tran et al. 2003) also found a relation between massive star formation and the presence of interaction signatures in this type of starburst. However, a systematic analysis of a significant sample of starburst galaxies containing WR stars was needed to derive more robust statistics and definitive results. We have therefore completed a detailed morphological, photometric, and spectroscopic study of 20 objects, the majority being extracted from the catalogue of WR galaxies published by Schaerer et al. (1999). This study combines deep optical and near-infrared (*NIR*) broad-band and Hα imaging with optical spectroscopy (long-slit and echelle) data. Additional X-ray, far-infrared, and radio data were compiled from the literature. We performed a comprehensive and coherent study of all galaxies using the same reduction and analysis procedures and the same set of equations to determine their physical and chemical properties, with the emphasis of a global analysis of the sample. The main aims are to study the formation of massive stars in starburst galaxies and the role that interactions with or between dwarf galaxies and/or low surface brightness objects have in triggering bursts. The results of this deep analysis of local starbursts would also have an important impact on our knowledge about the galaxy evolution: galaxy interactions between dwarf objects should be more common at high redshifts, as hierarchical formation models of galaxies (i.e. Kauffmann & White 1993; Springer et al. 2005) predict.

1.3. Structure of the study

We analyze our sample of WR galaxies in the following way. In this paper (Paper I), we present the photometric results derived from the optical and near-infrared (*NIR*) broad-band and

Hα images. The aims of the observations in broad-band filters are the following:

1. to analyze the stellar-component morphology of each galaxy, looking for signs of interactions (e.g. arcs, plumes, bridges, and tidal tails) and possible low-surface brightness companion objects. The identification and the localization of these features and external objects with respect to the main galaxies provides clues about their evolution, allowing us to suggest how the star-formation burst was triggered;
2. to perform aperture photometry of each galaxy and its different regions (star-forming knots and emission-free areas) to characterize the stellar population that dominates the bursts and the underlying low-luminosity component. The comparison of the colors with the predictions of population synthesis models permits us to estimate the age of the last star-formation burst.

We completed deep observations in narrow-band Hα filters to study the extension and properties of the ionized gas. The continuum-subtracted Hα images were used to:

1. study the distribution of the ionized gas, and check the physical association of other surrounding star-forming objects with the main galaxy;
2. estimate the Hα luminosity, which indicates the total number of ionized stars in each burst and in the galaxy, as well as the ionized gas mass and the star formation rate (SFR). The total mass of the ionizing cluster can also be estimated;
3. calculate the Hα equivalent width, which is a powerful indicator of the age of the last star-formation burst.

In Sect. 2 we present our observations, some details of the data reduction processes, and some useful relations. A description of the galaxies, the deep optical maps obtained for each system, and the photometric results for all optical and *NIR* broad-band and Hα filters are presented in Sect. 3. Some results found in the photometric analysis of our galaxy sample and its summmary are discussed in Sect. 4.

In the second paper of this series (Paper II), we will present results derived by analyzing our intermediate-resolution spectroscopy. In the final paper (Paper III), we will compile the properties derived using data from other wavelengths and summarize the global analysis combining all available multiwavelength data. It is, so far, the most complete and exhaustive data set of this kind of galaxies, involving multiwavelength results and analyzed following the same procedures. We will discuss the significant role that interactions with or between dwarf galaxies play in the triggering of massive star formation in Wolf-Rayet galaxies.

2. Observations

Our photometric observations are classified into three types: broad-band optical imagery (standard Johnson filters in *U*, *B*, *V*, and *R* bands), narrow-band Hα and adjacent continuum imagery (narrow-band filters centered at the wavelength of the Hα emission line at the redshift of the galaxy), and broad-band *NIR* imagery (filters in *J*, *H* and *K*s bands). We describe our observations, reduction, analysis procedures, and present the selection criteria of our sample of WR galaxies.

2.1. Selection criteria of the sample galaxies

Since we are interested in the analysis of the massive star population (Wolf-Rayet stars) in starburst galaxies, we considered the most recent catalogue of Wolf-Rayet galaxies (Schaerer et al. 1999) as a starting point. As we remarked in the introduction, the WR galaxy catalogue contains an inhomogeneous group of starbursting objects. Our analysis however is mainly focused in dwarf galaxies. Therefore, we did not consider either spirals galaxies or giant H II regions within them, and considered only dwarf objects, such as apparently isolated BCDGs and dwarf irregular galaxies that had peculiar morphologies in previous, shallower imaging. Finally, we chose a sample of dwarf WR galaxies that could be observed from the Northern Hemisphere. The only exception was NGC 5253, for which deep echelle spectrophotometry using 8.2 m VLT was obtained (see López-Sánchez et al. 2007). We also chose two galaxies belonging to the Schaerer et al. (1999) catalogue that were classified as *suspected* WR galaxies (Mkn 1087 and Tol 9), to confirm the presence of massive stars within them. Finally, we also included the galaxy IRAS 08339+6517 because previous multiwavelength results suggested that the WR stars could still be present in its youngest star-forming bursts (see López-Sánchez et al. 2006).

The general properties of our galaxy sample are described in Table 1, where we provide the equatorial coordinates, Galactic extinction, apparent and absolute *B*-band magnitudes, distances (assuming a Hubble flow with $H_0 = 75$ km s^{-1} and $q_0 = 0.5$, and correcting for Galactic Standard of Rest using our spectroscopic data; see Paper II), oxygen abundances (derived from our spectroscopic data; see Paper II), morphological type (derived from NED), and other common names for each system.

2.2. Optical imagery

Images in optical wavelengths were obtained in several observing runs between the years 2000 and 2006, mainly using the 2.56 m *Nordical Optical Telescope* (NOT) located at the *Roque de los Muchachos* Observatory (ORM, La Palma, Spain). However, some observations were completed at the 2.5 m *Isaac Newton Telescope* (INT), located at the ORM, and in the 2.2 m telescope of the *Centro Astronómico Hispano-Alemán* (CAHA) at *Calar Alto* Observatory (Almería, Spain). In Table 2, the telescope, date, number of images, and exposure time for the broad-band optical observations of our galaxy sample are indicated. We observed 18 galaxies in *all* optical broad-band filters, SBS 1054+365 was observed in all filters apart from *R*-band, and only one galaxy (NGC 5253) was not observed for which we adopt data from NED. We also used the photometric data of Mkn 1087 (*U*-band) and POX 4 (*U*, *B* and *V* bands) given by Méndez (1999). The details of these observations are the following:

1. Observations at the 2.56 m NOT. We completed three observing runs at this telescope: January–March 2004, April 2005, and April 2006. We also obtained data during three Spanish Service-Time nights (23 October 2002, 20 January 2003, and 7 January 2006). In all observations, the ALFOSC (*Andalucia Faint Object Spectrograph and Camera*) instrument was used in image mode, with a CCD Loral/Lesser detector 2048 × 2048 pixel array, pixel size of 15 μm. The spatial resolution was 0.19″ pixel^{-1}, and the field of view was 6.3′ × 6.3′.
2. Observations at the 2.2 m CAHA. Two observing runs were completed at this telescope, in December 2000 and November 2004, using the CAFOS (*Calar Alto Faint Object Spectrograph*) instrument in image mode. CAFOS was located at the Cassegrain focus of the telescope. Two

Table 1. Main data of the sample of 20 WR galaxies analyzed in this work.

Galaxy	RA (2000) (h m s)	Dec (2000) (° ′ ″)	$E_G(B-V)^a$	m_B^b	M_B^b	d^c (Mpc)	[O/H]^d (dex)	Type^e	Other names
NGC 1741	05 01 38.4	−04 15 25	0.051	13.59	−20.01	52.5	8.22	pec	HCG 31 AC, Mkn 1089, SBS 0459-043
Mkn 1087	04 49 44.4	+03 20 03	0.063	13.08	−22.14	110.6	8.57*	S0 pec	II Zw 23
Haro 15	00 48 35.9	−12 43 07	0.023	13.82	−20.87	86.6	8.37*	(R)SB0 pec?	Mkn 960
Mkn 1199	07 20 28.3	+33 32 21	0.054	12.98	−20.68	54.0	8.75*	Sc H II	SBS 0720+335
Mkn 5	06 42 15.5	+75 37 33	0.084	14.83	−15.57	12.0	8.07	I? H II	SBS 0635+756
IRAS 08208+2816	08 23 55.0	+28 06 14	0.032	15.10	−21.29	190.0	8.42*	Irr	...
IRAS 08339+6517	08 38 23.2	+65 07 15	0.092	12.94	−21.57	78.3	8.45*	Pec LIRG H II	...
POX 4	11 51 11.6	−20 36 02	0.039	14.56	−18.79	45.5	8.03	H II	IRAS 11485-2018
UM 420	02 20 54.5	+00 33 24	0.036	17.32	−19.55	237.1	7.95	Compact	SBS 0218+003
SBS 0926+606A	09 30 06.5	+60 26 52	0.031	16.45	−17.29	55.9	7.94	BCG, H II	...
SBS 0948+532	09 51 32.0	+52 59 36	0.013	17.93	−18.43	187.4	8.03	Sy	...
SBS 1054+365	10 57 47.0	+36 15 26	0.021	15.46	−14.06	8.0	8.00	NE	...
SBS 1211+540	12 14 02.5	+53 45 18	0.020	17.32	−13.27	13.1	7.65	BCG	...
SBS 1319+579	13 21 10.0	+57 39 41	0.014	15.32	−18.53	28.8	8.05*	H II	...
SBS 1415+437	14 17 01.7	+43 30 13	0.009	15.32	−14.52	9.3	7.58	BCG	...
III Zw 107	23 30 09.9	+25 31 58	0.060	14.36	−20.14	79.6	8.23	Im	IV Zw 153, IRAS 23276+2515
Tol 9	10 34 38.7	−28 35 00	0.065	13.92	−19.26	43.3	8.58	E4: H II	IRAS 10323-2819,ESO 435-42,Tol 1032-283
Tol 1457-262a	15 00 29.0	−26 26 49	0.158	14.44	−19.73	68.1	8.22*	H II	IRAS 14575-2615, ESO 513-IG11
Arp 252	09 44 58.6	−19 43 32	0.049	16.22	−19.35	129.8	8.50*	Gpair pec	ESO 566-7 + ESO 566-8
NGC 5253	13 39 55.9	−31 38 24	0.056	10.09	−17.92	4.0^f	8.28*	Im pec H II	Haro 10

[a] Value of the Galactic extinction (Schlegel et al. 1998); [b] corrected for Galactic and internal extinction; [c] except for NGC 5253, the distances were estimated from our optical spectra and correcting for Galactic Standard of Rest (see Paper II); [d] oxygen abundance, in units of 12 + log(O/H), derived in this work for each galaxy (see Paper II). If several regions were analyzed in the same galaxy (indicated by a star), the highest oxygen abundance derived using T_e is shown; [e] morphological type as indicated by NED; [f] distance obtained by Karachentsev et al. (2004).

different detectors were used: a CCD SITe detector with 2048 × 2048, a pixel size of 24 μm, and 0.53″ pixel^{-1} spatial resolution during the observations in December 2000, and a CCD LORAL detector with 2048 × 2048, a pixel size of 15 μm, and 0.33″ pixel^{-1} spatial resolution for observations in November 2004. Because of the physical size of the filters, only a circular disk with a diameter of 11′ is not vignetted by this instrument.

3. Observations at the 2.5 m INT were completed on 22 September 2003 and 6 October 2005, as well as 19 November 2005 (a Spanish Service-Time night under non-photometric conditions). We used the *Wide Field Camera* (WFC) that consists of 4 adjacent CCDs each an array of 2048×4096 pixels with a pixel size of 15 μm. Located in the primary focus of the telescope, it has a spatial resolution of 0.33″ pixel^{-1}, yielding a field of view of 11.2′ × 22.4′ in each chip. In our observations, only the central chip was analyzed.

The details of the reduction process and analysis of the optical images are described in Appendix A.

2.3. NIR imagery

All *NIR* observations with J, H and K_s filters were completed at the 1.5 m Carlos Sánchez Telescope (CST), located at the Observatorio del Teide (Tenerife, Spain). We used the CAIN camera, which has a mosaic of 256 × 256 pixels sensitive in the 1–2.5 μm wavelength interval consisting of four independent chips of dimensions 128 × 128 pixels, each one controlling one quadrant of the camera. The physical size of each pixel is 40 μm, corresponding to 1″ pixel^{-1} in wide field mode. The total field of view was 4′ × 4′.

We acquired a sequence of exposures at slightly different positions to obtain a clean sky image, following the method described in López-Sánchez et al. (2004a). Table 3 shows the number of individual raw images obtained for each galaxy and filter as well as the date on which they were acquired.

We completed four observings runs at the telescope: September 2002, March 2003, February 2004, and April 2004. Additionally, we also observed on 4 February 2003 and 23 May 2005. Because of the upper limit in declination of the CST (65°), Mkn 5, and IRAS 08339+6517 were not observed. The starburst galaxy NGC 5253 was not observed because it is a southern object. Three galaxies (III Zw 107, SBS 0948+532 and SBS 1211+540) were not observed because of several technical problems and/or bad weather conditions. Therefore, only 14 galaxies of our sample were observed in *NIR* using CST, 13 of them using all filters (Arp 252 was not observed in K_s). For those objects, we did not acquire new *NIR* data, but used instead results given by the *Two Micron All Sky Survey* (2MASS, see Cutri et al. 2000; Jarrett et al. 2000) project. The details of the reduction process and analysis of the NIR images are described in Appendix B.

2.4. Hα imagery

Hα and adjacent continuum images were obtained during the same runs used for the observation of the broad-band images, and therefore using the same telescopes and instrumentation. We chose adequate narrow-band filters (with a *FWHM* of ∼50 Å) to detect the redshifted Hα λ6562.82 emission line taking into account the recession velocity of the object given by the NASA/IPAC Extragalactic Database (NED) and/or our optical spectra. We obtained Hα images for all galaxies in our sample apart from POX 4 and NGC 5253, for which we used the results provided by Méndez (1999) and Meurer et al. (2006), respectively. Table 4 compiles all the data (date, telescope, filters, exposure time, airmasses, and worst seeing) concerning our Hα observations. The quality of these observations is remarkable: the worst seeing of the Hα images for 9 up to 19 (47%) of

the galaxies is lower than 1″. The details of the reduction process and analysis of the Hα images are described in Appendix C.

2.5. Stellar populations

For all galaxies and knots, we compared our optical/*NIR* colors (corrected for extinction and emission of the ionized gas) with the predictions given by three different population synthesis models, STARBURST99 (Leitherer et al. 1999), PEGASE.2 (Fioc & Rocca-Volmerange 1997), and Bruzual & Charlot (2003), to estimate the age of the dominant stellar population of the galaxies, the star-forming regions, and the underlying stellar component. We selected these models because while, the first are based on Geneva tracks, the other two use Padua isochrones (Bertelli et al. 1994) in which thermally pulsing asymptotic giant branch (TP-AGB) phases are included. We assumed an instantaneous burst with a Salpeter IMF, a total mass of 10^6 $M_\odot$, and a metallicity of $Z/Z_\odot$ = 0.2, 0.4 and 1 (chosen in function of the oxygen abundance of the galaxy derived from our spectroscopic data, see Paper II) for all models. Since these models are optimized to study the youngest stellar populations within the galaxies, ages above 500 Myr cannot be measured reliably, but their values are useful for discriminating between young (≤25 Myr), intermediate (100–300 Myr), and old (>500 Myr) stellar populations (see López-Sánchez et al. 2006, for details of the method). We used the W(Hα) of all analyzed star-forming knots to estimate the age of their most recent starbursting episode comparing with the predictions given by the STARBURST99 (Leitherer et al. 1999) models (last column in Table 7), which have a far smaller error (between 0.1 and 0.5 Myr) than the ages derived using broad-band colors (typically, between 2 and 5 Myr for young stellar populations). In Paper II we will show that the ages derived from W(Hα) are in good agreement with those derived from the spectroscopic data. As we conclude in Sect. 4 and Paper III, a proper estimate of the stellar population age for this type of galaxy using broad-band filters is only obtained when bursts and underlying components are independently considered.

3. Results

Tables 5 and 7 provide the optical and *NIR* broad-band, and the Hα photometric results, respectively, of all WR galaxies studied. We estimated the contribution of nebular gas to the broad-band optical filters of all objects with considerable nebular emission using the procedure described in Apendix A; they are provided in Table 6. The underlying component is always indicated by UC. In this section, we present the main photometric results found for each galaxy. Typically, we show two figures per object: a deep image of the galaxy and its surroundings (sometimes derived by combining images in different filters) that includes the identification of all objects/regions and the slit positions used to obtain the spectroscopic data, and a figure showing the contour maps in Hα (continuum subtracted), B, and J (R when lacking *NIR* data). Apart from where otherwise indicated, the external isophote of these contour maps corresponds to a 3σ confidence level detection above the sky level. The names of the knots are identified by letters (A, B, C...); C is usually the central region and/or the brightest knot. MB refers to the main body of the galaxy, which is composed of several independent knots and does not include the low luminosity component. Capital letters indicate regions that we have analyzed using spectroscopy (see Paper II); lower-case letters are regions identified in our images but without spectroscopic data. Knots in galaxies with many star-forming regions (Mkn 1087, IRAS 08208+2816, IRAS 08339+6517, POX 4 and Tol 1457–262) are labelled with numbers, sometimes following the same notation used by previous authors. All regions are clearly identified and named in the deep optical image of each galaxy.

3.1. NGC 1741 – HCG 31 AC

NGC 1741 is the brightest object in the galaxy group HCG 31. Following the nomenclature given by Hickson (1982), NGC 1741 is HCG 31C, but this classification is ambiguous because A and C are clearly interacting, forming a single entity (HCG 31 AC). Our broad-band photometric analysis of NGC 1741 and the galaxies belonging to HCG 31 was presented in López-Sánchez et al. (2004a), but we compile the results here, including a correction for nebular emission that was not considered in that paper.

The continuum-subtracted Hα contour map of HCG 31 compared with the R contour map is shown in Fig. 1. Our image is deeper than that presented by Iglesias-Páramo & Vílchez (1997) and shows the numerous star-forming regions inside the galaxies. The values of the Hα fluxes and the properties derived for each region are compiled in Table 7. We estimate an Hα flux of $(11.0 \pm 0.7) \times 10^{-13}$ erg cm^{-2} s^{-1} for HCG 31AC = NGC 1741. Considering the distance to this object (52.5 Mpc), we derive a star-formation rate of ∼2.9 $M_\odot$ yr^{-1}, a similar value to those obtained using the *FIR* fluxes ($SFR_{\rm FIR} = 3.3$ $M_\odot$ yr^{-1}, $SFR_{60\,\mu{\rm m}} = 2.8$ $M_\odot$ yr^{-1}) and only slightly higher than obtained using the 1.4 GHz radio-continuum luminosity ($SFR_{1.4\ {\rm GHz}} = 2.0$ $M_\odot$ yr^{-1}). The equivalent widths estimated from our Hα map agree with those derived from our spectroscopic data (López-Sánchez et al. 2004a).

3.2. Mkn 1087

Mkn 1087 is a luminous blue compact galaxy that shows several filaments and surrounding dwarf objects, suggesting that it is a group in interaction. Our analysis of Mkn 1087 was presented in López-Sánchez et al. (2004b), but in Table 5 we compile the results of our broad-band photometric analysis after correcting the contribution of the emission lines.

We present the first Hα data available for Mkn 1087 and its surrounding objects, which are indicated in Table 7. The continuum-subtracted Hα contour map of Mkn 1087 compared with the R contour map is shown in Fig. 2. In Hα, we detect only the galaxy main body (MB), the bright knot #7, and some regions towards the north that correspond to the objects #14 and #15 analyzed in our spectroscopic study (López-Sánchez et al. 2004b). We also detect the faint knot #1, the dwarf companion object to the north (N in Fig. 2) and the center of the nearby galaxy KPG 103a. We do not detect knot #2 in our Hα-map, which therefore implies that it should be a background galaxy, but #3, #11, and #12 are all physically associated with Mkn 1087 and are candidate TDGs. The integrated Hα flux of Mkn 1087 is $(4.8 \pm 0.3) \times 10^{-13}$ erg cm^{-2} s^{-1}; its associated star-formation rate is $SFR_{\rm H\alpha} = 5.6 \pm 0.4$ $M_\odot$ yr^{-1}, similar to that derived from its 1.4 GHz luminosity ($SFR_{1.4\ {\rm GHz}} = 4.5$ $M_\odot$ yr^{-1}) but lower than that measured using by the *FIR* fluxes ($SFR_{\rm FIR} = 10.3$ $M_\odot$ yr^{-1}, $SFR_{60\,\mu{\rm m}} = 8.8$ $M_\odot$ yr^{-1}). Our Hα image confirms the star-formation activity in the north dwarf companion object (N) and in KPG 103a (K), the second object having a star formation rate of $SFR_{\rm H\alpha} = 1.8$ $M_\odot$ yr^{-1}. Using the Hα equivalent width, we estimate an age of ∼6 Myr for the most recent burst of star-formation

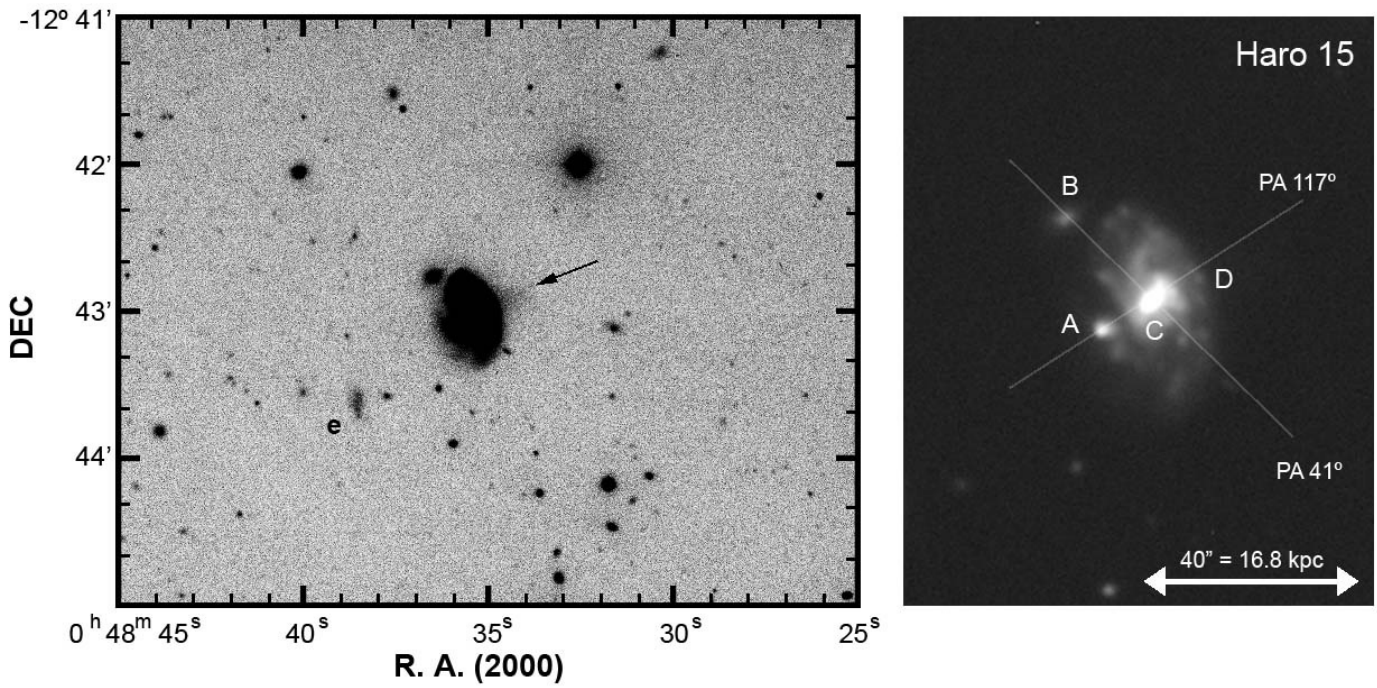

Fig. 3. Deep image of Haro 15 in *R* filter (2.2 m CAHA). (*Left*) The field surrounding the galaxy; the main object image was saturated to enhance those of the weakest objects; one object (e) is identified. A diffuse plume opposite A is indicated by an arrow. (*Right*) Non-saturated image of Haro 15 showing an apparent spiral pattern and the bright regions C (*center*), A and B, as well as the position of knot D. The two slit positions used for the INT long-slit spectroscopy are also shown.

in this object. The $W(\mathrm{H}\alpha)$ of the remaining regions agree with those derived from our spectroscopic data.

3.3. Haro 15

Since Haro (1956) introduced this object into his catalogue of blue galaxies showing emission lines, Haro 15 has been included in numerous analysis of BCG samples at optical (Deeg et al. 1997; Prugniel & Heraudeau 1998; Cairós et al. 2001a,b), *NIR* (Coziol et al. 2001), *FIR* (Calzetti et al. 1994, 1995), UV (Kazarian 1979; Kinney et al. 1993; Heckman et al. 1998), and radio (Gordon & Gottesman 1981; Klein et al. 1984, 1991) wavelengths.

3.3.1. Broad-band photometry

Haro 15 is located at 86.6 Mpc, at which distance 1″ is equivalent to 0.42 kpc. Our deep image (Fig. 3) appears to a spiral galaxy with two nearby objects located at the ESE (knot A) and NE (knot B). Mazzarella et al. (1991) described this system as *strongly interacting separated galaxies, or a single highly perturbed system which may be an advanced merger* because of the brightness of the knot A. Cairós et al. (2001a) followed the same notation. Our images however suggest that it is inappropriate to describe Haro 15 in this way. Region A is located at the edge of the galaxy, 11″ (4.62 kpc) from its center, and B appears to be offset from the spiral disk, suggesting that it is an independent galaxy. Furthermore, two faint regions are found at the WNW (a diffuse plume located opposite to A) and SW (in the direction opposite to B), although this seems to be a background object coincident with the border of the galaxy. At 1′ (25 kpc) to the SE of the center of Haro 15, we find the faint object e, which shows blue colors and Hα emission (Cairós et al. 2001b) indicating that it may be associated with the main galaxy.

Some previous broad-band photometric results were presented in López-Sánchez & Esteban (2003). The center of Haro 15 and regions A and B show blue colors, indicating recent star formation. The *NIR* colors of Haro 15 are in agreement with the previous values given by Hunter & Gallagher (1985), $J-H=0.54$ and $H-K=0.13$. However, as it noted by Cairós et al. (2001a), the contribution of ionized gas to the broad-band filters is important for this object (see Table 6).

3.3.2. Hα photometry

The continuum-subtracted Hα contour map is shown in Fig. 4. The three main structures of the galaxy are clearly identified, although the emission in the north region is more intense than in the south region. We estimated the Hα flux for Haro 15 and regions A and B using this flux-calibrated image, correcting for both extinction and the contribution of the [N II] emission lines. However, our Hα image was not of high quality because the Hα filter used at the 2.2 m CAHA telescope (667/8) has a transmitance of only 14% for the observed Hα wavelength of the galaxy, 6700 Å and, therefore, the errors in this object are higher compared with other galaxies analyzed in this work.

The total Hα flux estimated in Haro 15 is $(4.66 \pm 0.52)\times10^{-13}$ erg cm^{-2} s^{-1}, slightly inferior to that derived by Cairós et al. (2001a), $(6.84 \pm 0.01)\times10^{-13}$ erg cm^{-2} s^{-1}, probably because those authors lacked spectroscopic data and could not correct for [N II] emission. The Hα-based star formation rate is $SFR_{\mathrm{H}\alpha}=3.3\ M_\odot\,\mathrm{yr}^{-1}$, which agrees with that derived using the *FIR* fluxes, $SFR_{\mathrm{FIR}}=2.8\ M_\odot\,\mathrm{yr}^{-1}$, $SFR_{60\,\mu\mathrm{m}}=2.4\ M_\odot\,\mathrm{yr}^{-1}$, and the one obtained from the 1.4 GHz flux, $SFR_{1.4\ \mathrm{GHz}}=4.0\ M_\odot\,\mathrm{yr}^{-1}$. The total mass of ionized gas is $M_{\mathrm{H\,II}}\sim6.2\times10^6\ M_\odot$. Although A is 20 times smaller than the main galaxy, it possesses a SFR three times lower than the global value. This fact and the large measurement of $W(\mathrm{H}\alpha)$ indicate

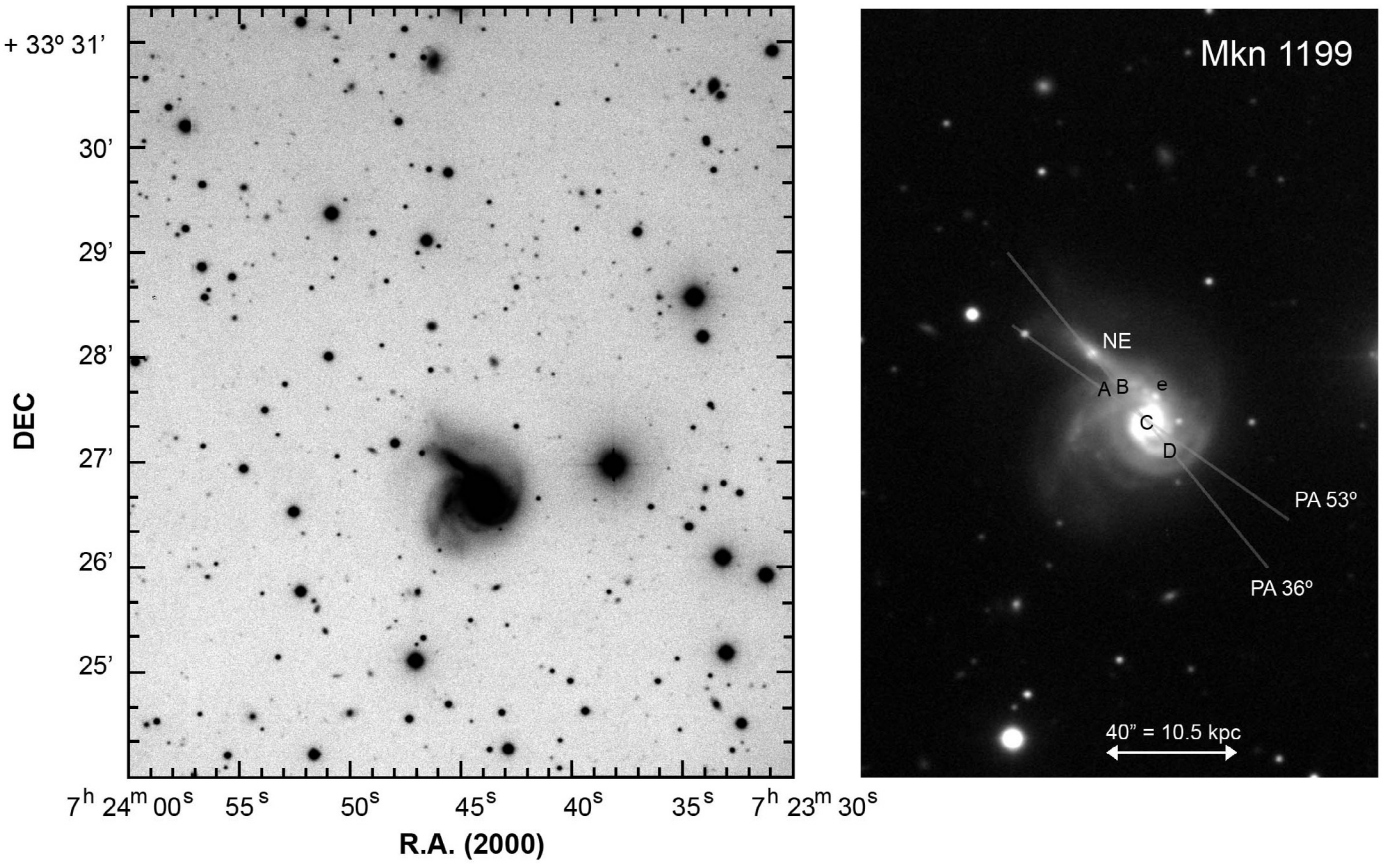

Fig. 5. Deep image of Mkn 1199 in the *R*-band (2.2 m CAHA). At *the left*, the field surrounding the galaxy is shown; the image was saturated to detect the faintest objects. At *the right*, a non-saturated image of Mkn 1199 is shown identifying the regions analyzed in this work and the two slit positions for which the spectroscopic data were acquiered.

that the star formation activity in this region is intense and started recently.

3.4. Mkn 1199

Mkn 1199 shows a clear example of interaction between galaxies. The main body is a Sb spiral galaxy, which is interacting with a dwarf object of elliptical morphology located at the NE. Markarian et al. (1979) included Mkn 1199 in their catalogue of galaxies with UV-excess. Its properties were revisited using both imagery and spectrocopy by Mazzarella & Balzano (1986), Mazzarrella & Boronson (1993), and Kazarian & Martirossian (2001).

3.4.1. Broad-band photometry

Our deep *R*-band image of Mkn 1199 is shown in Fig. 5. The galaxy is located at 54.0 Mpc, and 1″ is therefore equivalent to 0.26 kpc. We observe two systems in interaction: a face-on spiral galaxy (Mkn 1199) and a dwarf elliptical object located at 26″ (6.81 kpc) towards the NE. Between both objects, a prominent curved arm containing several star-formation regions (A, B, e) has developed. Two spiral arms start from the center of Mkn 1199 (C), one turning towards the NE companion and another towards the SW. Region D is located in this latter fainter arm. Another faint spiral arm is located towards the S, being distorted at the NW. The contour maps of our continuum-subtracted Hα, *B* and *J* images are shown in Fig. 6.

The colors obtained for Mkn 1199 and regions within are blue, except for the $V-R$ color where the contribution of old stars is appreciable. We extracted two apertures in the NE companion: one (NE in Table 5) containing all of its flux, which shows red colors indicating that an old stellar population dominates its flux, and another aperture containing light only from its center (NE c), which shows bluer colors and therefore a younger stellar population.

3.4.2. Hα photometry

Figure 6 shows the contour map of our continuum-subtracted Hα image of Mkn 1199. Strong nebular emission is found in its main body and in the center of the NE companion. Several star-forming regions are identified in the NE arms. We do not detect nebular emission in any other object in the field at the radial velocity of Mkn 1199.

Hα and adjacent continuum images were obtained on 20 December 2000 at the 2.2 m CAHA telescope. However, it was a non-photometric night, and under non-photometric conditions, but we completed an approximate flux-calibration using our spectroscopic data. We created a mask rebuilding the slit positions shown in Fig. 5, with a width of 1″ and the appropriate position angle (PA), and measured the number of counts in the combined Hα image. At each slit position we extracted a spectrum considering all emission and integrated the Hα + [N II] flux. We then scaled the counts with respect to those measured in the continuum-subtracted Hα image. The results were consistent, and we used the average value to perform the flux-calibration.

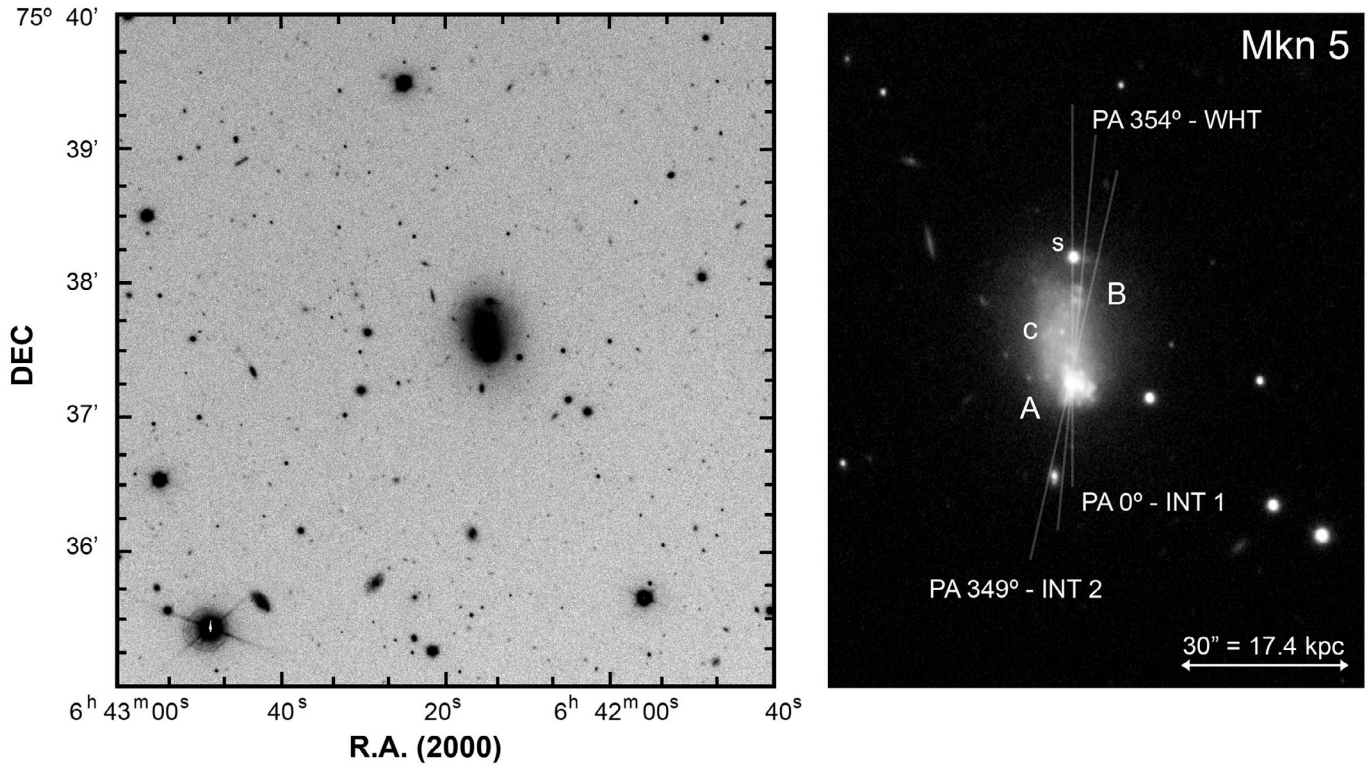

Fig. 7. Deep image of Mkn 5 in *V* filter (2.56 m NOT). *The left image* shows the field surrounding the galaxy; it has been saturated to reveal the fainter objects and the extensive elliptical low brightness component. *At the right*, a non-saturated image of Mkn 5 identifying its main regions: A (with a high star-formation activity), B (star-forming region to the north) and c. A star to the north (s) and the three slit positions used for spectroscopy are also indicated.

The total Hα flux of the system is 1.4×10^{-12} erg cm^{-2} s^{-1}. The Hα-based star formation rate was 3.9 $M_\odot$ yr^{-1}; this is lower than measured using the *FIR* fluxes, $SFR_{\rm FIR} = 4.7\ M_\odot$ yr^{-1} and $SFR_{60\,\mu{\rm m}} = 4.7\ M_\odot$ yr^{-1}, but consistent within the errors, so we consider that our flux calibration is acceptable. However, we were unable to determine equivalent widths because the flux calibration of the adjacent-continuum image was also required.

3.5. Mkn 5

Since Markarian (1967) included this object in his first list of galaxies with UV continua, Mkn 5 has been studied on several occasions because of its peculiar characteristics. It is a dwarf ($M_B \sim -15.6$) and nearby ($v_{\rm rad} \sim 792$ km s^{-1}) low metallicity [12 + log(O/H) ~ 8.1] galaxy showing intense Hα emission and an extensive, regular and elliptical envelope formed by old stars. Mkn 5 is indeed usually classified as a cometary-type BCDG. Its photometric properties were analyzed by Mazzarella & Balzano (1986), Cairós et al. (2001a,b), Gil de Paz et al. (2003), Noeske et al. (2005), and Caon et al. (2005).

3.5.1. Broad-band photometry

Mkn 5 is located at a distance of 12.0 Mpc. At that distance, 1″ is equivalent to 0.58 kpc. Our deep *V* image is shown in Fig. 7 and reveals a field rich in background objects. The low-brightness elliptical component is extended ~30″ along the Mkn 5 major axis. The main area of the galaxy, region A, is located to the south and shows nebular emission. At ~15″ (0.87 kpc) towards the north, another star-forming region (B) is located, but it is fainter than A. Between both regions, an elongated main body hosting some small regions is found.

We analyzed several apertures in Mkn 5, one including all of its flux, and another considering only the main body of the galaxy (MB in Table 5, which excludes the low-surface brightness envelope), regions A, B, and c and the low-brightness component (UC). The photometric results agree with those obtained by Cairós et al. (2001a). We did not observe Mkn 5 in *NIR*, but the colors obtained by Noeske et al. (2005) in *J*, *H*, and *K′* agree with those of our optical data in terms of the predictions of population synthesis models.

Regions A and B show very blue colors and are therefore dominated by young stars, but c is an evolved knot because of its redder colors. The structure observed in A does not have a central condensation but is very irregular. It may be a conglomerate of several neighbouring star-formation regions or due to of an irregular dust distribution. Comparing with population synthesis models, the colors of region A suggest an age lower than 5 Myr for the most recent star-formation burst. As expected, the extensive low-brightness component (UC) shows redder colors, indicating an age older than 1 Gyr (Caon et al. 2005).

3.5.2. Hα photometry

The two independent star-forming regions of Mkn 5 are easily observed in our continuum-subtracted Hα image (Fig. 8). The Hα flux obtained for region B is only 1.4% that derived for region A, where we estimate a value of $f_{\rm H\alpha} = (2.96 \pm 0.08) \times 10^{-13}$ erg cm^{-2} s^{-1}. It is in excellent agreement with the estimate given by Gil de Paz et al. (2003), $f_{\rm H\alpha} = (2.8 \pm 0.3) \times 10^{-13}$ erg cm^{-2} s^{-1}, because these authors also

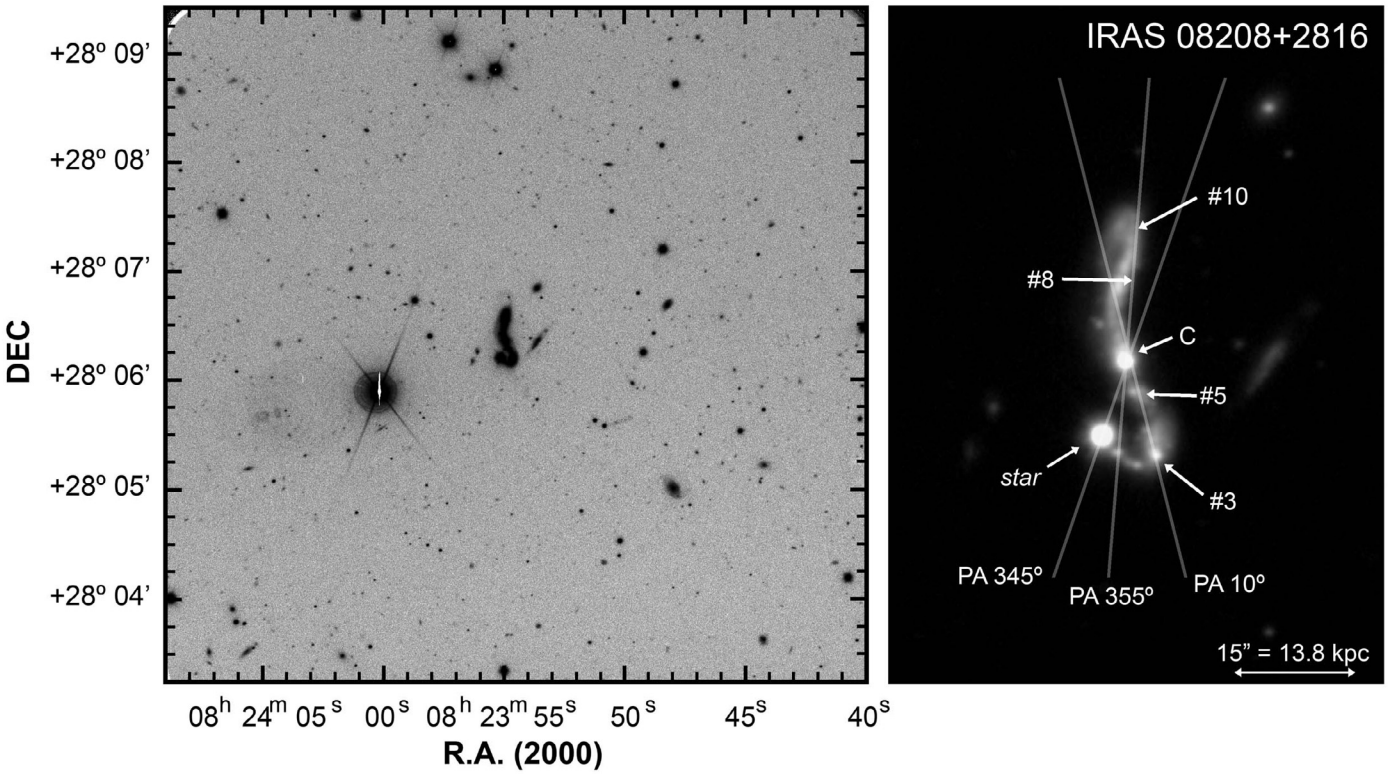

Fig. 9. Deep *V* image of IRAS 08208+2816 (2.56 m NOT). *At the left*, the field surrounding the galaxy is shown; the image has been saturated in order to show the faintest objects. *At the right*, a non-saturated image combining the data in *U*, *B* and *V* filters is shown. The slit positions used to obtain the spectroscopic data are indicated. The most important regions (those studied by spectroscopy) are named, as well as a bright star in the end of the southern tail.

corrected for extinction and [N II] contribution, which is practically negligible in this case. The number of O7V equivalent stars needed to explain the Hα luminosity is ~3750. The star-formation rate of this region is $SFR_{\mathrm{H}\alpha} \sim 0.04\ M_{\odot}\,\mathrm{yr}^{-1}$. The IRAS satellite only detected this galaxy at 60 μm; its associated star-formation rate was $SFR_{60\,\mu\mathrm{m}} \sim 0.07\ M_{\odot}\ \mathrm{yr}^{-1}$. Mkn 5 is no detected at 1.4 GHz but Hopkins et al. (2002) provided an upper limit for its flux, for which we computed $SFR_{1.4\,\mathrm{GHz}} < 0.06\ M_{\odot}\,\mathrm{yr}^{-1}$. All of these values are in agreement with the Hα-based SFR. The age derived from W(Hα) confirms that the most recent starburst episode happened less that 5 Myr ago.

3.6. IRAS 08208+2816

IRAS 08208+2816 is an object listed in the 15th survey of galaxies with UV excess emission performed by the *Kiso* 1 m Schmidt telescope (Takase & Miyauchi-Isobe 1992). Perryman et al. (1982) analyzed the peculiar morphology of the system with CCD imaging. It was identified by the IRAS satellite as a luminous-infrared galaxy, and its *FIR* data and redshift estimate were published by Fisher et al. (1995).

3.6.1. Broad-band photometry

IRAS 08208+2816 has a distance of 190 Mpc at which 1″ corresponds to 0.92 kpc. Our deep *V*-filter image is shown in Fig. 9, where an object with a size of 33″ (30.4 kpc) and extending along the north-south direction is found close to a bright star ($m_B \sim 13$). A non-saturated image reveals a galaxy with a bright center (C) and two apparent tails that rise in opposite directions: the southern tail has a size of 13″ (12 kpc), a PA of ~20°, and ends just at the bright star, and a northern tail, with size of 18″ (16.6 kpc), and AP ~ 350°, which seems to be curved towards the east. Several star-forming regions are found throughout both tails: the most important (those analyzed using spectroscopy) are indicated in Fig. 9.

The seeing of our images in the *U*, *B*, and *V* bands was excellent, 0.7″, therefore we delimited the different regions well. All have detectable Hα emission, as is evident in Fig. 10 (left). As expected for objects with nebular emission, their colors are blue, especially towards the center. We were unable to find any emission-free area inside the galaxy, and therefore could not analyze the properties of the underlying stellar component. However, the colors of the northern tail imply that an older stellar population is present within the star-forming regions.

3.6.2. Hα photometry

IRAS 08208 + 2816 hosts strong nebular emission, its total Hα flux is $f_{\mathrm{H}\alpha} = (3.3 \pm 0.3) \times 10^{-13}$ erg cm^{-2} s^{-1}. Considering the distance to the galaxy, more than one million O7V equivalent stars are needed to explain its Hα luminosity. This value confirms the intense star-formation activity that the galaxy has experienced, which is supported by the high values of ionized hydrogen mass, $M_{\mathrm{H\,II}} = (2.1 \pm 0.2) \times 10^{7}\ M_{\odot}$, and star formation rate, $SFR_{\mathrm{H}\alpha} = 11 \pm 1\ M_{\odot}\,\mathrm{yr}^{-1}$. The H$\alpha$-based *SFR* is identical to those derived using *FIR* fluxes, i.e. $SFR_{\mathrm{FIR}} = 11 \pm 1$ and $SFR_{60\,\mu\mathrm{m}} = 9.7 \pm 0.8\ M_{\odot}\,\mathrm{yr}^{-1}$, although the value derived from the 1.4 GHz radio-continuum flux is slightly higher $SFR_{1.4\ \mathrm{GHz}} = 16.4 \pm 0.7\ M_{\odot}\,\mathrm{yr}^{-1}$. The 1.4 GHz thermal flux amounts to less than 3% of the total flux at these wavelengths. The Hα equivalent widths agree with those obtained in our

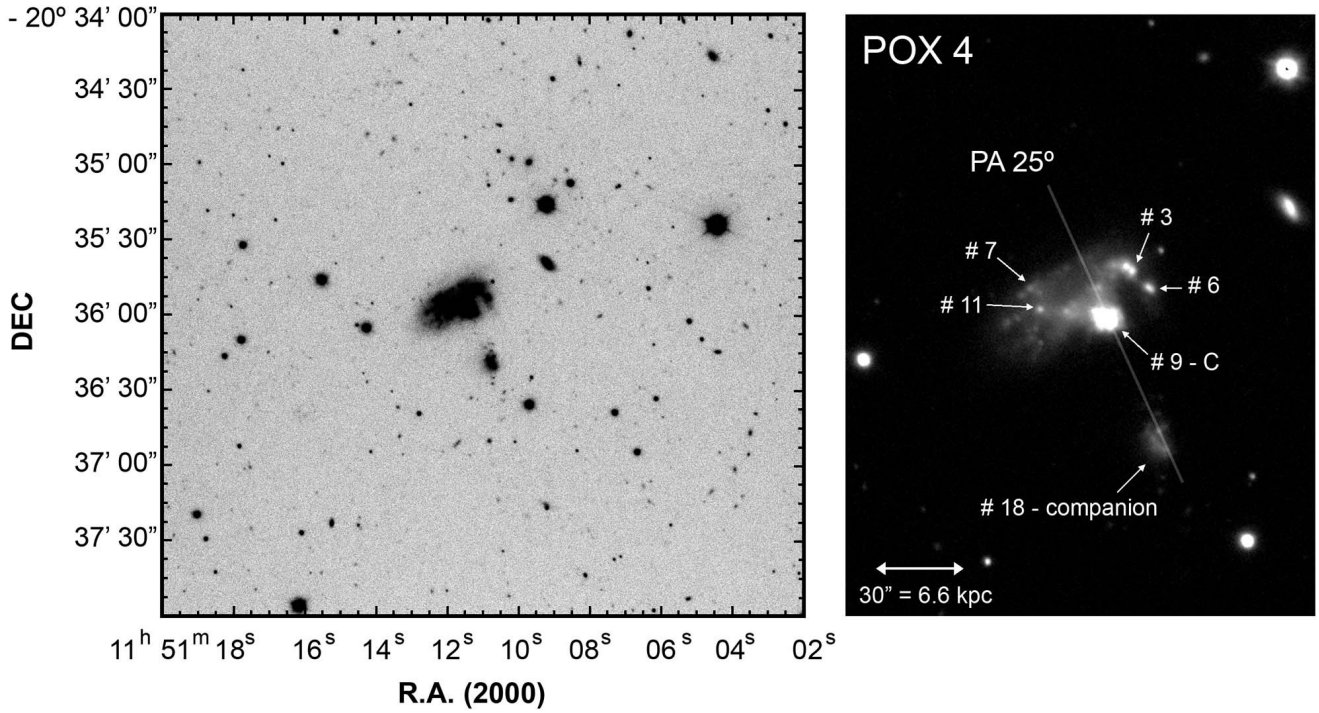

Fig. 11. Deep *R* image of POX 4 (2.56 m NOT). The field surrounding the galaxy is shown *on the left*; the image was saturated to reveal the faintest objects. *On the right*, a non-saturated image of POX 4 is shown. All important regions (following the names given by Méndez & Esteban 1999) and the slit position used to obtain the spectroscopic data at the 4.2 m WHT are indicated.

spectroscopic analysis, and imply an age of ∼5 Myr for the most recent star-formation burst in its youngest regions (C and #5). Assuming $Z = 0.4\ Z_\odot$ and $M_\star = 10^6\ M_\odot$, STARBURST 99 models (Leitherer et al. 1999) provide a total luminosity of $L_B = 2.73 \times 10^8\ L_\odot$ for a 5 Myr-old starburst. Comparing with the total luminosity of IRAS 08208+2816, $L_B = 5.12 \times 10^{10}\ L_\odot$, a total stellar mass of $M_\star \sim 1.9 \times 10^8\ M_\odot$ was derived. This value is in excellent agreement with the estimate given by the Díaz et al. (1999) relation, $M_\star \sim 1.7 \times 10^8\ M_\odot$.

3.7. IRAS 08339+6517

IRAS 08339+6517 is a luminous infrared and Lyα-emitting starburst galaxy that has a dwarf companion object at a projected distance of 56 kpc. It was studied by observations of a wide range of wavelengths because of its peculiar properties: a compact bright nucleus (Margon et al. 1988), abundant molecular gas (Wiklind 1989), Lyα emission and absorptions in C IV λ1550 and Si IV λ1400 emission lines (González-Delgado et al. 1998; Kunth et al. 1998), significant X-ray emission (Stevens & Strickland 1998), and an elongated H I tidal tail in the direction of the dwarf companion galaxy (Cannon et al. 2004). We acquired new photometric and spectroscopic observations to study its morphology, distribution of ionized gas, chemical composition, kinematics, SFR, and stellar populations, and to search for WR features in its younger bursts. Our analysis was published by López-Sánchez et al. (2006) but, to indicate the data used for all galaxies in our sample, we compile the photometric results in Tables 5 and 7.

3.8. POX 4

POX 4 is an interesting BCDG first listed in the *Palomar Objective-prism X survey* (Kunth et al. 1981). Telles et al. (1997) described an object showing extensive external isophotes and a ring of three or four star-forming regions surrounding a bright knot. Méndez & Esteban (1997) indicated the presence of low-intensity asymmetric wings (with maximum velocities between ±200 km s^{-1}) in the profiles of the optical emission lines. Méndez & Esteban (1999) used broad-band optical and Hα images, and high-resolution spectroscopy to propose that it was a low-mass ring galaxy formed after the pass of a faint companion object. POX 4 was included in the analysis of BCGs in *B*, *R*, and Hα bands performed by Gil de Paz et al. (2003) and Gil de Paz & Madore (2005).

3.8.1. Broad-band photometry

POX 4 is located at 45.5 Mpc; at that distance, 1″ is equivalent to 0.22 kpc. Our new deep *R* image of POX 4 and its surroundings (Fig. 11) shows an irregular galaxy morphology with a luminous compact region (#9) surrounded by an arc of several bright knots at its north. We analyzed only the brightest regions identified by Méndez & Esteban (1999), #3, #6, #7, #9 (center), and #11. An independent dwarf galaxy (*companion* or #18) is located at 21″ (4.64 kpc) towards the SW.

We adopted the *U*, *B*, and *V* data given by Méndez & Esteban (1999) to obtain the optical and *NIR* magnitudes and colors of POX 4 (Table 5). We corrected the data for extinction by assuming that the value of $E(B-V)$ derived in #9 was applicable to all regions apart from #18. The correction for nebular emission is important in this galaxy because of its brightness and extension (Fig. 12). Although the colors are blue, their comparison with theoretical models indicates the existence of an older (age ≥300 Myr) stellar population underlying the bursts. The most recent star-bursting episode in #9 occurred ∼3.5 Myr ago. Although the companion object (#18) shows Hα emission, it was dominated by a 200–300 Myr-old stellar population.

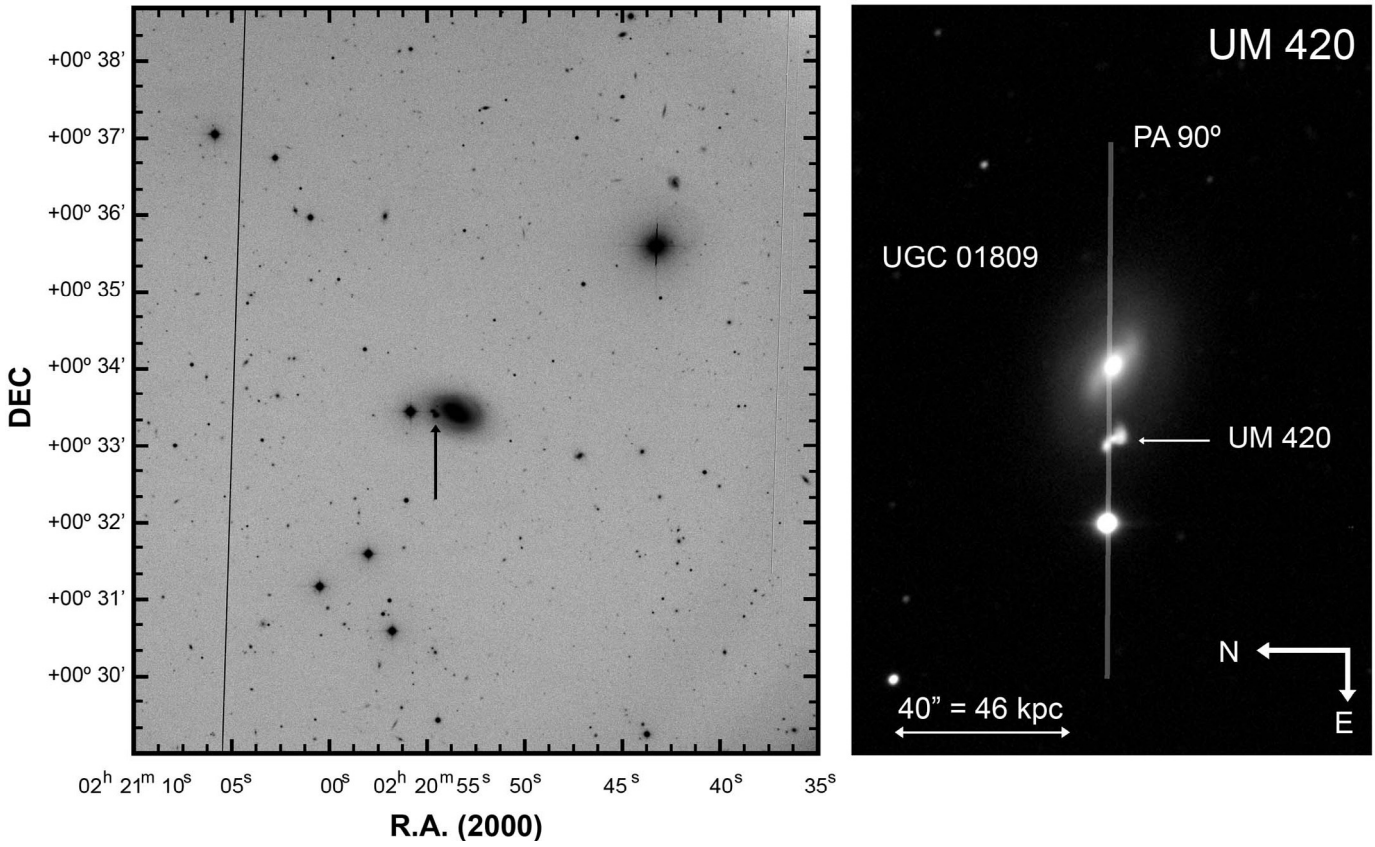

Fig. 13. (*Left*) Deep image of UM 420 (pointed at with an arrow) and UGC 1809 (the spiral galaxy to the west of UM 420) in *R*-band (2.5 m INT). It has been saturated to show the faintest objects. (*Right*) Deep non-saturated image of UM 420 in the *B*-band (2.2 m CAHA). All objects and the slit position used to spectroscopy at 4.2 m WHT are indicated. Notice that North is at left.

3.8.2. Hα photometry

We reanalyzed the continuum-subtracted Hα image of POX 4 presented by Méndez & Esteban (1999) (Fig. 12). We analyzed our spectroscopic data and derived a more precise distance to the galaxy (they assumed 47.3 Mpc). Our Hα fluxes, compiled in Table 7, were roughly 6% higher than those determined by Méndez & Esteban (1999). The total Hα flux that we measured for POX 4 was $(15.5 \pm 0.5) \times 10^{-13}$ erg cm^{-2} s^{-1}, slightly higher than that found by Gil de Paz et al. (2003), $(9.4 \pm 0.8) \times 10^{-13}$ erg cm^{-2} s^{-1}. Assuming a distance of 45.5 Mpc, we estimated that $SFR_{\rm H\alpha} = 3.05 \pm 0.10$ $M_\odot$ yr^{-1}, an order of magnitude higher than expected on the basis of the *FIR* and 1.4 GHz fluxes, i.e. $SFR_{60\,\mu{\rm m}} = 0.31$ $M_\odot$ yr^{-1} and $SFR_{1.4\,{\rm GHz}} = 0.26$ $M_\odot$ yr^{-1}. Furthermore, the thermal flux at 1.4 GHz is high, almost 45% of the total flux at these frequencies, but usually it is less than 10% in starburst galaxies (Dopita et al. 2002). Perhaps, our Hα flux is overestimated. If true, our W(Hα) values may also be overestimated, which would explain the discrepancy between the ages derived from them and broad-band colors by comparing with theoretical models.

3.9. UM 420

The galaxy UM 420 was detected in the survey of emission-line extragalactic objects performed by the University of Michigan (MacAlpine & Lewis 1978). Photometric studies of UM 420 are found in Salzer et al. (1989a) and Campos-Aguilar et al. (1993).

3.9.1. Broad-band photometry

UM 420 is the farthest galaxy analyzed in this work: its radial velocity is 17 500 km s^{-1} and it is therefore located at 237 Mpc, at which distance 1″ is equivalent to 1.15 kpc. Our deep *V* image is shown in Fig. 13. UM 420 is located just 16.5″ towards the east of a bright spiral galaxy named UGC 1809, for which the NED provides a value of 7306 km s^{-1} for the radial velocity of this last object. Therefore, it lies at only 97 Mpc, far closer than UM 420. We observe UM 420 behind the external areas of the UGC 1089 disk. An *essential note* given by the NED indicates that UM 420 is probably an H II region in UGC 1809, but we see that this is clearly not the case.

Despite its distance, our images reveal that UM 420 has an irregular and elongated morphology orientated at PA ~ 45°, with two long regions extending in different directions from the brightest central region. The edge of the southern region appears to extend towards the west. The total length of UM 420 is ~7.2″ (8.3 kpc). There is a bright star 18″ towards the south of UM 420, but it does not interfere with our photometric analysis.

The absolute magnitude of UM 420, $M_B = -19.55$, indicates that it is not a dwarf object. Despite the good flux calibration of the images and corrections for both extinction and nebular emission, we observe some discrepancies in the photometric values of UM 420: although the $U - B$ color is blue, the remaining colors are not. This fact is probably due to the contamination induced by the external regions of the spiral disk of UGC 1809 (see Fig. 14), which is dominated by older stars than those present in UM 420.

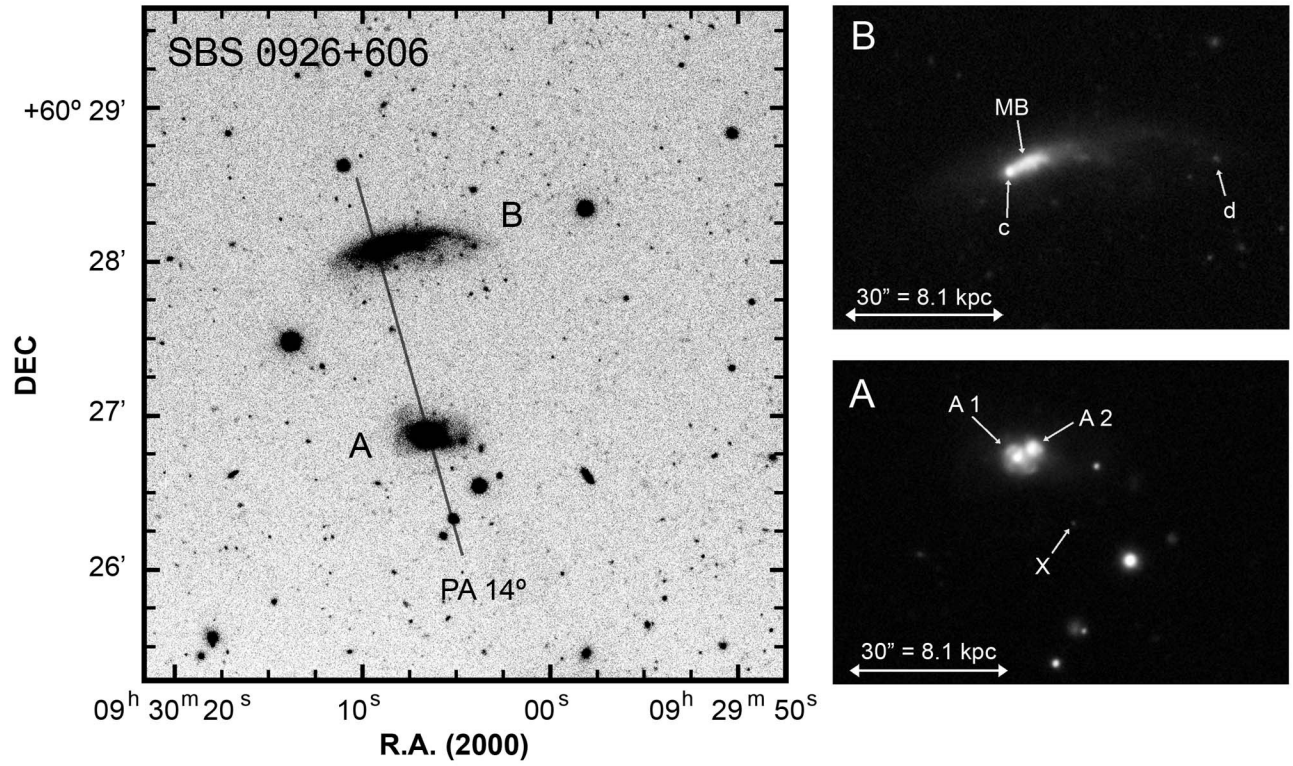

Fig. 15. Deep image of the pair of galaxies SBS 0926+606 combining the U, B and V images (2.56 m NOT). At the left, the field surrounding the galaxies is shown. The image was saturated to detect the faintest objects, some of them are identified, as well as the slit position used at 4.2 m WHT to acquire the spectroscopic data. The non-saturated images *at the right* show the internal structure of A (*down*, revealing its double nucleus) and B (*top*, showing the intense knot c).

3.9.2. Hα photometry

This is the first time that UM 420 is analyzed using Hα imagery. Figure 14 shows the contour map of our continuum-subtracted Hα image compared with the contour maps for B and J. The Hα-continuum contribution of UM 420 was determined by taking into account both non-saturated stars and the disk of UGC 1809. We observe that the Hα emission completely dominates the flux output of UM 420, for which we estimate a Hα flux of $f_{\mathrm{H}\alpha} = (6.95 \pm 0.43) \times 10^{-14}$ erg cm^{-2} s^{-1}. More than 340 000 O7V equivalent stars would be required to generate this luminosity. The Hα-based SFR is 3.7 ± 0.2 $M_{\odot}$ yr^{-1}, which is higher than obtained from 1.4 GHz data, $SFR_{1.4\ \mathrm{GHz}} = 1.9 \pm 0.9$ $M_{\odot}$ yr^{-1}. The non-thermal contribution to the 1.4 GHz flux is 90%. The high W(Hα) value, 980 Å, indicates how recently (4.3 Myr) the last burst of star formation occurred.

3.10. SBS 0926+606

SBS 0926+606A is a BCDG listed in the *Second Byurakan Sky Survey* (Stepanian 1994 and references within). It is a pair of nearby objects denoted by A (the compact galaxy in which the WR feature is detected) and B (IRAS 09263+6039, a more elongated object located 73 arcsec to the north of A) of the same radial velocity. Some photometric measurements were given by Bicay et al. (2000) and Pustilnik et al. (2001).

3.10.1. Broad-band photometry

Figure 15 shows our deep image of SBS 0926+606 combining the data in U, B, and V filters. It is located at 55.9 Mpc, at which distance 1″ is equivalent to 0.27 kpc. Figure 15 is probably the deepest image obtained of the system so far. It reveals two irregular dwarf ($M_B \sim -17.3$) objects: SBS 0926+606B is a cometary-shape galaxy, with a bright region (c) located at the eastern tip of a bright elongated structure (MB). The galaxy is embedded in an extensive low-brightness component (B_{UC}) that shows two tails. A knot at the end of the northern tail (d) appears non-stellar and has blue color. On the other hand, SBS 0926+606A (the galaxy classified as WR) shows two bright central structures (A1 to the east and A2 to the west). These separated by only 2.6″ (0.7 kpc), are blue in color and have strong Hα emission. The non-saturated image reveals three curved structures starting from A1, one reach A2. An irregular low-luminosity component (A_{UC}), which extends to a significant distance from the double central nucleus, is also found.

Object A has a blue color, as expected for a BCDG. Comparing with evolutionary synthesis models, we estimate an age of 5 Myr for the most recent burst episode. The colors of its low-luminosity component are redder, indicating that it consists mainly of an older stellar population (of age higher than 300 Myr). SBS 0926+606B is also shows in color but the star formation is not as intense as in A, appart from the small region c and d. Object d may be a tidal dwarf galaxy candidate, although due to its faint magnitude ($M_B \sim -12.1$), it would probably not be a kinematically independent entity. The low-luminosity component of SBS 0926+606B is also red in color.

We remark that object X, although barely detected in B, is brighter than other objects in J. It is extremely reddened,

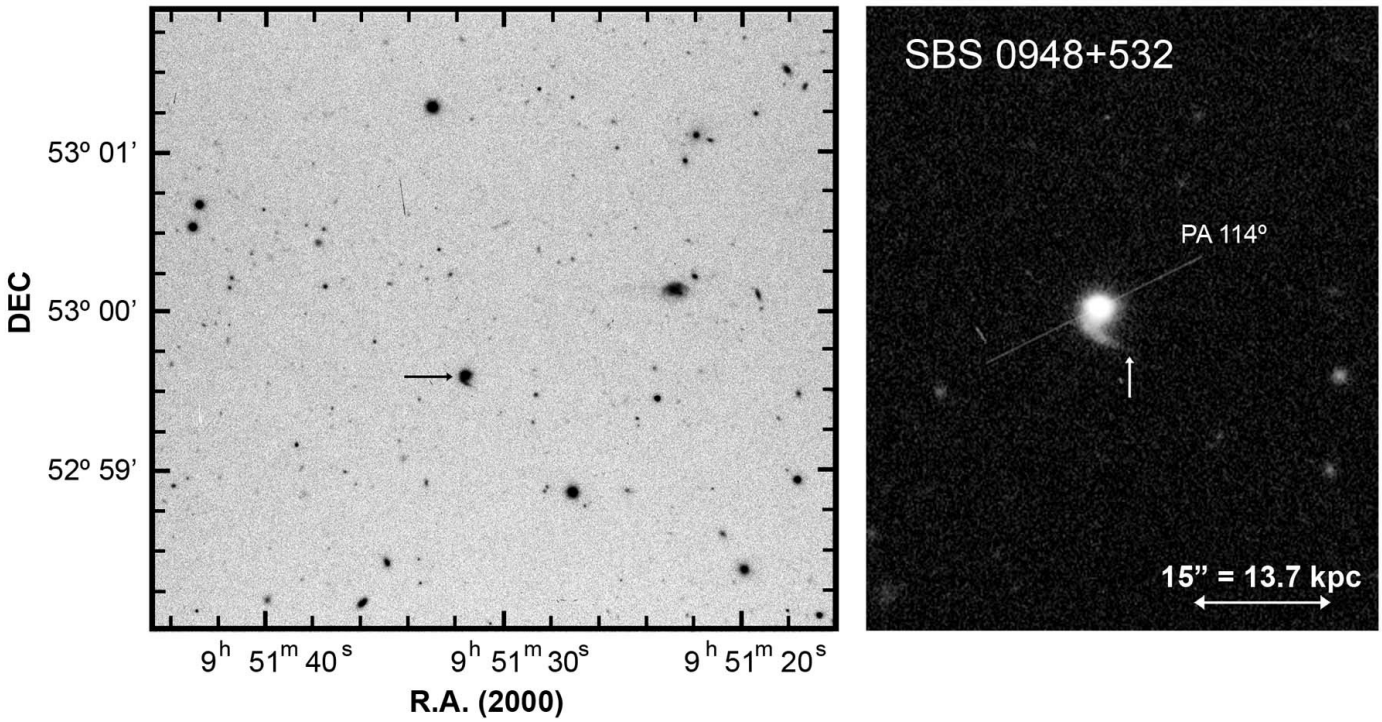

Fig. 17. Deep image of SBS 0948+532 combining the images in U, B, V, and R (2.56 m NOT). *On the left*, the field surrounding the galaxy is shown. *On the right*, the non-saturated image of SBS 0948+532 includes the slit position used to obtain the spectroscopic data at 4.2 m WHT. The end of the tail is indicated by an arrow.

$V - J \sim 4.4$ and $V - K_s \sim 6.2$. Because of its Galactic latitude (43°), it is probably a high-redshift galaxy.

3.10.2. Hα photometry

The contour map of our continuum-subtracted Hα image of both galaxies are shown in Fig. 16. Galaxy A shows its double nucleus that is embedded in an elliptical envelope and orientated in a different direction to that observed in broad-band filters. Its total Hα flux is $(2.52 \pm 0.12) \times 10^{-13}$ erg cm^{-2} s^{-1} and more than 69 000 O7V equivalent stars would be required to explain its Hα luminosity. We also derive $SFR_{H\alpha} = 0.75 \pm 0.04\ M_\odot\ yr^{-1}$, higher than expected on the basis of the *FIR* and 1.4 GHz data ($SFR_{60\mu m} = 0.19\ M_\odot\ yr^{-1}$ and $SFR_{1.4\ GHz} = 0.24\ M_\odot\ yr^{-1}$). The age of the most recent star-forming burst derived from the W(Hα) is the same as that estimated using broad-band colors (5 Myr).

Galaxy B shows an elongated structure that coincides with the MB region described in broad-band filters, showing an eastern compact condensation. Although the surface brightness is low (lower than the 3σ significance detection level of the sky level), a weak Hα plume is detected towards the south, aligned perpendicularly to the MB. If this feature is real, it suggests that a galactic wind exists of in this object. The knot d identified in broad-band filters at the end of the tail, is not observed in the Hα image. The total Hα flux in galaxy B is $(6.31 \pm 0.56) \times 10^{-14}$ erg cm^{-2} s^{-1}, four times lower than derived in galaxy A, and its SFR is $SFR_{H\alpha} = 0.19 \pm 0.02\ M_\odot\ yr^{-1}$.

3.11. SBS 0948+532

SBS 0948+532 is a BCDG belonging to the *Second Byurakan Survey* (Markarian & Stepanian 1984). It is so compact that in the *Palomar Sky Survey* it is indistinguishable from a blue star, and Markarian & Stepanian (1984) suggested therefore that it was a Seyfert-type galaxy.

3.11.1. Broad-band photometry

SBS 0948+532 has a distance of 187.4 Mpc and is the second farthest object in our sample. At that distance, 1″ is equivalent to 0.91 kpc. Our deep image of SBS 0948+532, which has a seeing of 0.6″, combining the data of all broad-band optical filters is shown in Fig. 17. It shows a star-like spherical object of size 2.3″ (2.1 kpc). Our deep R image reveals a faint tail emerging from the SE of the galaxy that turns towards the SW, reaching a distance of 4.6″ (4.2 kpc) from the center.

The correction for nebular emission was performed following the standard procedure. However, the high equivalent widths found in the brightest emission lines of this object indicate that the contribution to the V filter is high, $\Delta m_{V,e} = 1.48$. We consider that this value is unrealistic; the colors derived by assuming this value are inconsistent and do not match predictions of population synthesis models. Equation (A.3) is possibly inappropriate for objects of high equivalent widths in its emission lines, or we are overestimating the equivalent widths. Using results derived for similar objects analyzed in this work, we assumed $\Delta(B - V)_e \sim 0.7$ and $\Delta(V - R) \sim -0.6$.

Considering its absolute B-magnitude, $M_B = -18.43$, SBS 0948+532 is a dwarf object. Its colors extremely very blue, with $U - B \sim -1.2$ and is the bluest object analyzed in this work. This reflects both the strength and youth (~2 Myr) of the starburst. It is interesting to note that, except for $V - R$ (probably contaminated by the underlying old stellar population), the colors become bluer when we increase the size of the region, suggesting that star formation is occurring not only in its

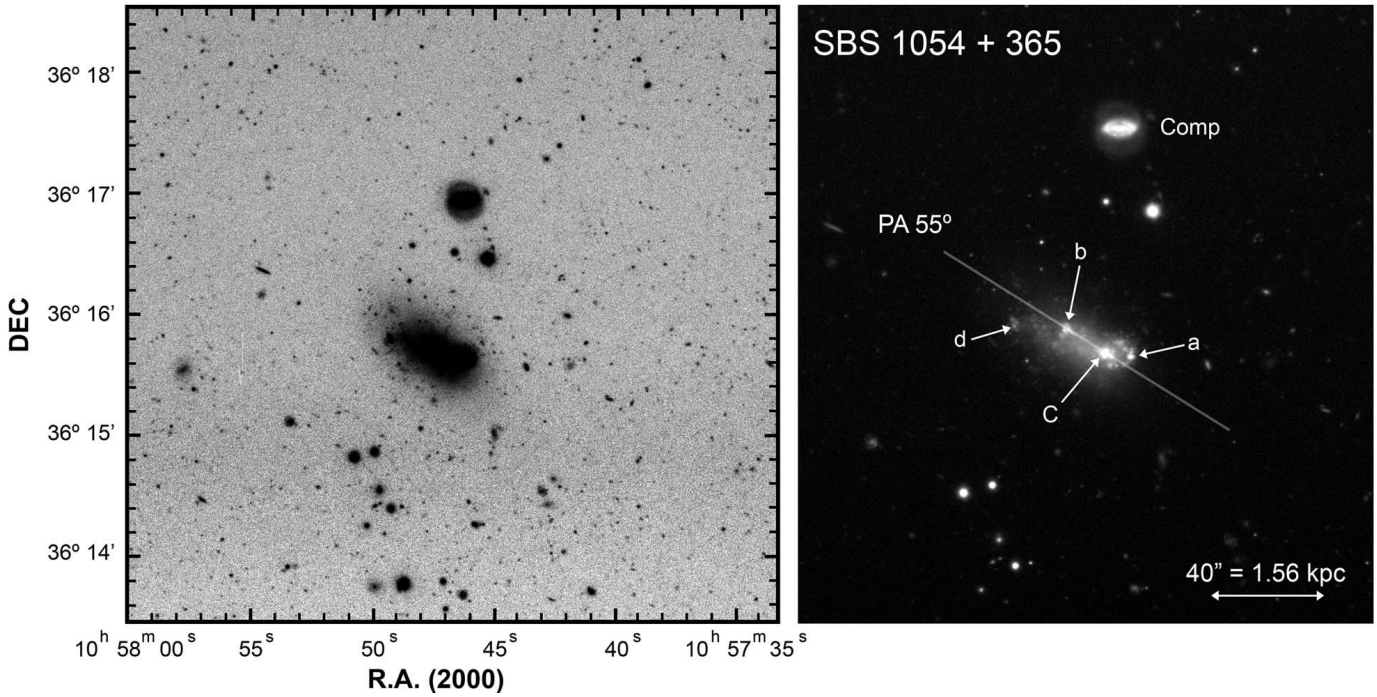

Fig. 19. Deep image of SBS 1054+364 obtained by adding all exposures in U, B and V filters (2.56 m NOT). *To the left*, the field surrounding the galaxy is shown. The image was saturated to detect the faintest objects and the extensive low-luminosity component surrounding SBS 1054+365. The right non-saturated image indicates the slit position used to obtain the spectroscopic data using the 2.5 m INT, as well as the position of several regions inside the galaxy and a nearby object labelled as Comp.

center but over the entire system. However, the colors determined for the tail are red, indicating that it is dominated by an older stellar population of age between 50 and 200 Myr. We did not observe it in *NIR* bands and it is not detected by 2MASS because of its faint magnitude (m_R = 17.99), so we could not analyze its *NIR* colors.

3.11.2. Hα photometry

The continuum-subtracted Hα map (Fig. 18) shows a spherical object without any remarkable features, although its seeing (~1.4″) is more than twice as good as that of the broad-band optical images. The total Hα flux derived for SBS 0948+532 is $f_{\mathrm{H}\alpha} = (1.86 \pm 0.07) \times 10^{-13}$ erg cm^{-2} s^{-1}, which translates to a high luminosity and star formation rate because of galaxy distance. We compute $SFR_{\mathrm{H}\alpha} = 6.21 \pm 0.23\ M_{\odot}\ \mathrm{yr}^{-1}$. This is the first estimate of the star-formation rate in this galaxy because of the lack of *FIR* and 1.4 GHz data. More than 570 000 O7V equivalent stars would require to be present to explain its Hα luminosity.

3.12. SBS 1054+365

SBS 1054+365 is a nearby (V_{rad} ~ 603 km s^{-1}) and poorly studied BCDG. It was classified as the galaxy pair VV 747 in the catalogue of interacting galaxies performed by Vorontsov-Velyaminov (1959, 1977) because of the detection of a nearby companion object about 1′ to the north. There is no additional information about this companion galaxy, named 2MASX J10574661+3616582 by the NED. SBS 1054+365 has a radial velocity similar to that observed in the edge-on spiral galaxy NGC 3432 (UGC 5986, V_{r} = 616 km s^{-1}), located at 67.1′ (1.6 Mpc of projected distance) from SBS 1054+365 (García-Ruiz et al. 2002). They probably therefore belong to the same group.

3.12.1. Broad-band photometry

SBS 1054+365 is located at only 8.0 Mpc. At that distance, 1″ is equivalent to 39 pc. Figure 19 shows a deep image combining all the exposures in the U, B, and V bands. The seeing was excellent and 0.8″. The image reveals an elliptical-shape object of size 55″ (2.15 kpc) and 26″ (1.01 kpc), embedded in a low-luminosity component. Although more extended than the bright elliptical internal region, it is not orientated in the same direction. Several blue and Hα-emitting regions are found inside the galaxy main body. The brightest region, C, is located at its western border. Several star-forming regions constitute a semi-ring structure (a), which delineate the western limit. Towards the NE, at 16″ (0.62 kpc) from C, bright knot b is located. Region d is found at 33″ (1.29 kpc) from C, just at the eastern border, and 77″ towards the north of SBS 1054+364, 2MASX J10574661+3616582 is located (Comp in Fig. 19). Two lobes perpendicular to an elliptical-shape structure formed by a ring and a central bar are clearly identified. As said, there are no pre-existing observations of this object, which is classified as *galaxy* by NED.

Although we detect many background objects in the field, they are especially numerous surrounding SBS 1045+365. They may therefore be physically associated with the galaxy. This feature is also observed in other galaxies of our sample such as, for example, Mkn 5.

The absolute magnitude of SBS 1054+365 (M_B = −14.06) confirms that it is a dwarf galaxy. Its brightest region has blue colors, indicating an age lower than 5 Myr for its dominant stellar population. The remainder of the objects have blue colors, apart from the low luminosity component dominated by an

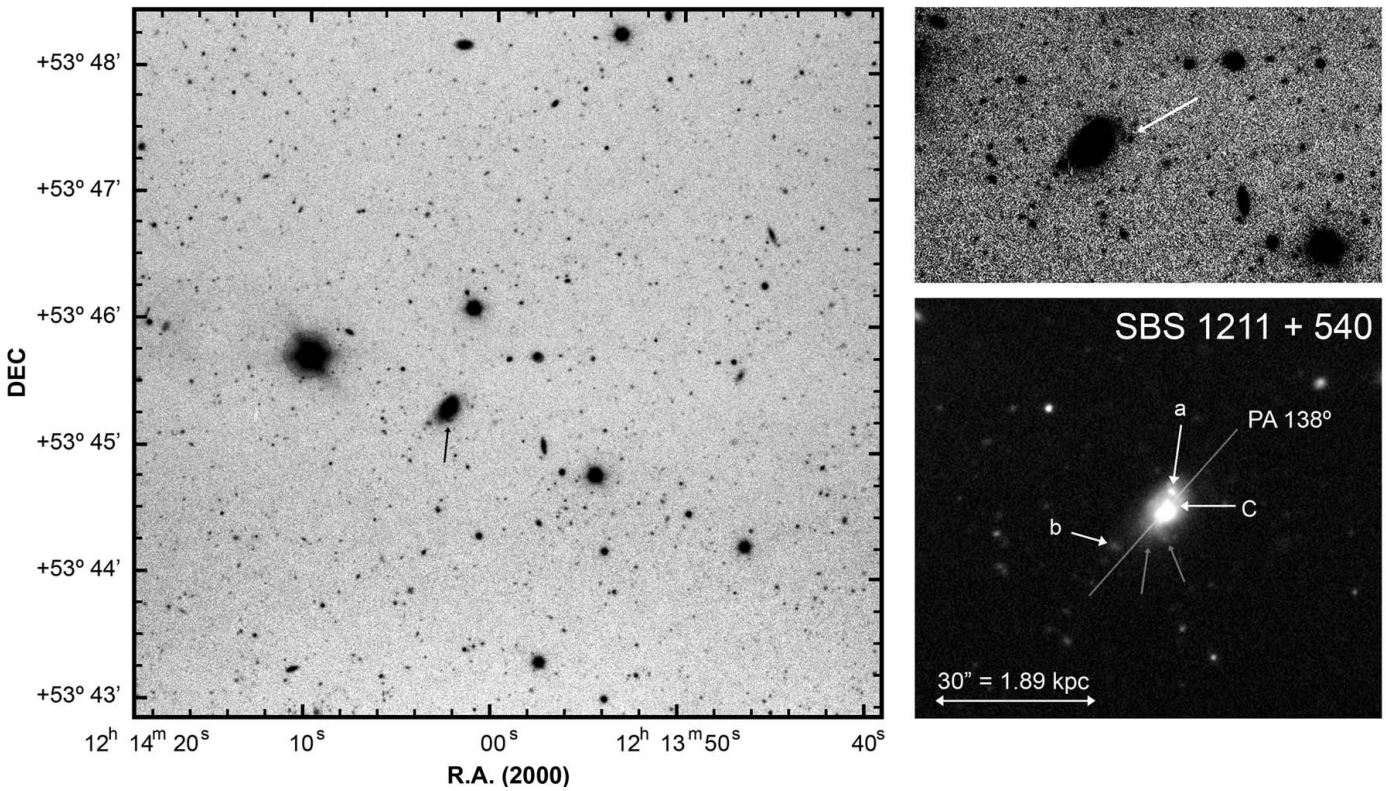

Fig. 21. Deep image of SBS 1211+540 combining all *U*, *B*, *V* and *R* data (2.56 m NOT). *At the left*, the field surrounding the galaxy is shown; the image was saturated to observe the faintest objects. SBS 1211+540 is identified by an arrow. *At the bottom right*, a non-saturated image of the galaxy indicates the regions analyzed in this work and the slit position used to obtain the spectroscopic data at the 4.2 m WHT. Two gray arrows point to two faint plumes to the south. *The top right image* shows a very saturated image of the galaxy, a very faint plume located at the NW area is indicated by an arrow.

old (ages ≥500 Myr) stellar population. The companion object shows optical and *NIR* colors consistent with evolved stellar populations except in its central region (Comp C), for which we estimate an age between 100 and 200 Myr. Its *NIR* magnitudes and colors are similar to that derived from 2MASS ($J-H \sim 0.63$ and $H-K_s \sim 0.38$).

3.12.2. Hα photometry

Practically all the nebular emission of SBS 1054+365 originates in its western region (Fig. 20), in particular from C and a. We identify a new knot (*e*) with Hα emission at the SW of the central region. Faint Hα-emission is also found in region *b*, which consists of two different knots, but there is no emission in *d*. The companion galaxy does not show any Hα emission, indicating either that it has no trace of ionized gas or has a different redshift than SBS 1054+365 (and hence both objects are not physically associated). The *FWHM* of the Hα filter constrains the redshift between $z = 0$ to $z \sim 0.0027$ (810 km s^{-1} ~ 10.8 Mpc). We believe that this interesting extragalactic object is more distant than SBS 1054+365, but spectroscopic data would be required to confirm this proposal.

The total Hα flux for SBS 1054+365 is $(5.87 \pm 0.22) \times 10^{-13}$ erg cm^{-2} s^{-1}. The number of O7V equivalent stars needed to explain its luminosity is ~3300. The star formation rate is $SFR_{H\alpha} \sim 0.04\ M_\odot\ yr^{-1}$, similar to that found using *FIR* data, $SFR_{FIR} \sim 0.01\ M_\odot\ yr^{-1}$ but is one order of magnitude higher than expected on the basis of the 1.4 GHz flux, $SFR_{1.4\ GHz} \sim 0.002\ M_\odot\ yr^{-1}$. The equivalent widths agree with those derived from spectroscopy, confirming an age of 5 Myr for the most recent starbursting episode.

3.13. SBS 1211+540

The BCDG SBS 1211+540 was identified by Markarian et al. (1985). Pustilnik et al. (2001) noted that the galaxy has a disturbed morphology with a nearby bright companion object.

3.13.1. Broad-band photometry

SBS 1211+540 lies at 13.1 Mpc, hence 1″ corresponds to 63 pc. Our deep image, that has a seeing of 0.7″ (Fig. 21), reveals a central knot (C) with a size of 3.3″ (208 pc) embedded in an elliptical low-luminosity component that has a size of 17″ × 10″ (1.07×0.63 kpc). Towards the N, at around 4.2″ (265 pc) from C, the bright object *a* is located. It appears to be connected to the central regions by a faint arc. In the opposite direction, another arc-like structure is found, extending outside the galaxy from its S region (indicated by an arrow in Fig. 21 left). We detect another faint plume towards the SE, reaching knot b located at 11″ (700 pc). A saturated image (top right image in Fig. 21) reveals another faint arc-like plume in its NW area.

We have no *NIR* data of SBS 1211+540 because this galaxy was not observed at 1.5 m CST and is not included in the 2MASS survey. The absolute *B*-magnitude of the galaxy, $M_B = -13.27$, indicates that it is a dwarf galaxy. Its optical colors agree with an object dominated by a young stellar population; the blue colors of C indicate an age lower than 5 Myr for the most recent star-formation burst. The $V-R$ color however

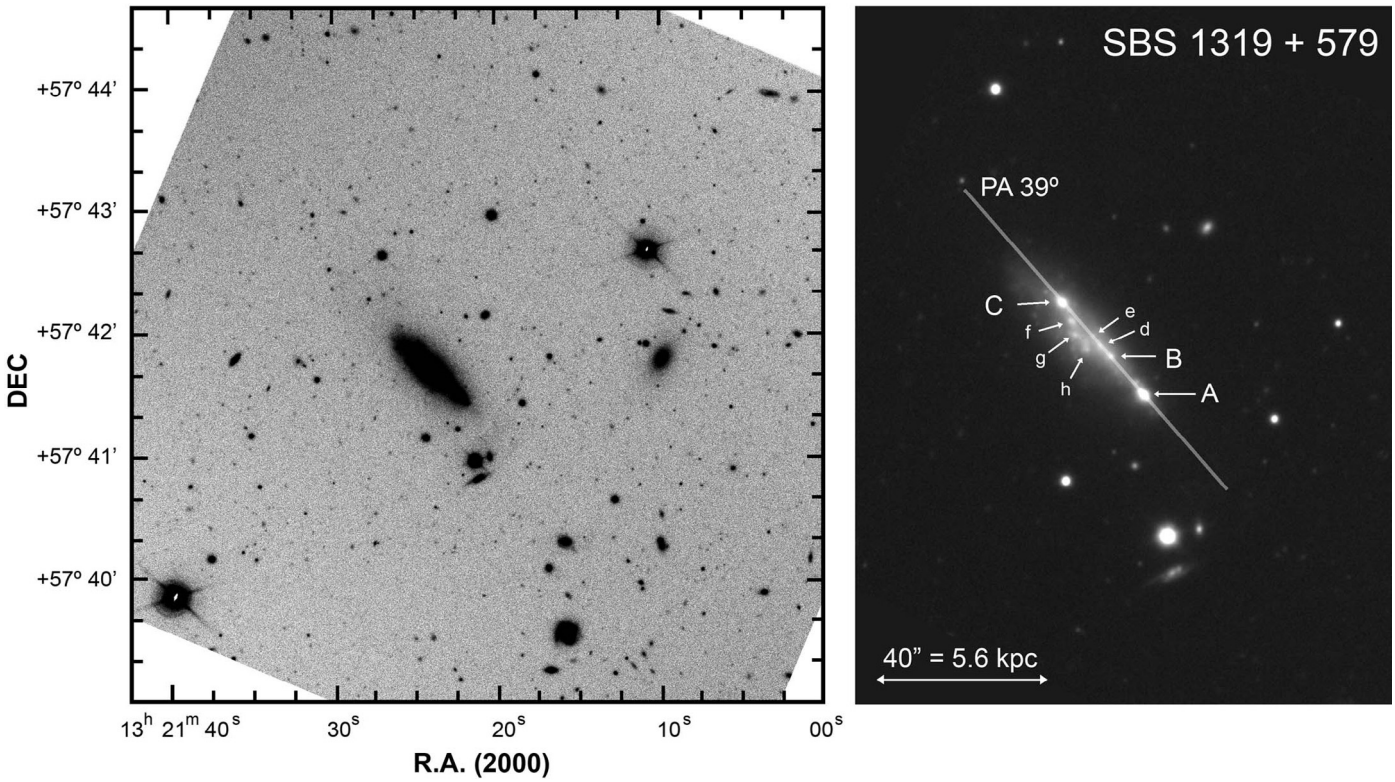

Fig. 23. Deep image of SBS 1319+579 in *V* filter (2.56 m NOT). *On the left*, the field surrounding the galaxy is shown. The image was saturated to show the faintest objects. *On the right*, a non-saturated deep image combining our *U*, *B*, *V*, and *R* data (2.56 m NOT) is shown. It includes the names of the most relevant regions inside the galaxy and the slit position used to obtain the spectroscopic data at the 4.2 m WHT. Regions A, B, and C are the same as the regions analyzed by Izotov et al. (1997).

suggests some contamination by an older stellar population. By analyzing the colors of the low-luminosity component, we derive $(B-V)_{\rm UC} = 0.29$ and $(V-R)_{\rm UC} = 0.35$, which are quite red colors suggesting the presence of stars of ages higher than 100 Myr. Object b has a redder color than determined for the low-luminosity component, and is therefore probably a background galaxy.

3.13.2. Hα photometry

Our continuum-subtracted Hα image of SBS 1211+540 is shown in Fig. 22. Comparing with the broad-band *B* and *R* filter images, we observe that the nebular emission is located in its northern region (C and a). We do not detect any Hα emission in knot b and in any other object in the field in the velocity range (0–810 km s^{-1}) covered by our narrow-band filter. The total Hα flux of SBS 1211+540 is $(8.17 \pm 0.31) \times 10^{-12}$ erg cm^{-2} s^{-1}. The number of O7V equivalent stars needed to explain this luminosity is ~1000. The Hα-based SFR is $SFR_{\rm H\alpha} \sim 0.013\ M_\odot\ {\rm yr}^{-1}$. No *FIR* data exists for this galaxy, and only a measurement of the upper limit of the 1.4 GHz luminosity is available, which equals $SFR_{1.4\ {\rm GHz}} < 0.012\ M_\odot\ {\rm yr}^{-1}$, a value close to that determined from our Hα flux. The Hα equivalent widths indicate that the age of the last star-forming burst at its center (~4.7 Myr) is just slightly lower than observed in knot a (~5 Myr).

3.14. SBS 1319+579

SBS 1319+579 is a comet-like BCDG located 5′ (42 kpc) from the beautiful edge-on spiral NGC 5113. Both galaxies have almost identical radial velocities ($V_{\rm r} = 2131$ km s^{-1} for NGC 5113 and $V_{\rm r} = 2060$ km s^{-1} for SBS 1319+579).

3.14.1. Broad-band photometry

Figure 23 shows our deep *V*-band image of SBS 1319+579. The galaxy is located at a distance of 28.7 Mpc, at which 1″ is equivalent to 0.14 kpc. The cometary structure of the galaxy is easily observed, and has a size of 53″ × 21″ (7.52 × 2.94 kpc). Several bright knots are aligned in a row, starting at the SW border (object A following the names given by Izotov et al. 1997) and ending in western object C, located at 30″ (4.2 kpc) from A. Between both objects, regions B, d, and e can be found. Other objects (f, g, and h) are located to the south of C. Our images, the deepest available for this object, suggest an alignment of the A-B-d-e regions and a different alignment of the knots C-f-g-h.

The absolute *B*-magnitude of SBS 1319+579, $M_B = -18.53$, indicates that it corresponds to the magnitude limit of dwarf galaxies. The colors of regions A, B, and C were corrected for the contribution of nebular emission. However, as we found in our analysis of SBS 0948+532, the high equivalent widths of the brightest nebular lines provide high values for this correction in region A; we believe that these values are unreliable, and we therefore assumed the average values indicated in Table 6. The colors derived for the internal regions are blue, especially in A and C, suggesting an age lower than 5 Myr for the dominant young population. The low-luminosity component shows redder colors, indicating that its old stellar population is older than 200 Myr.

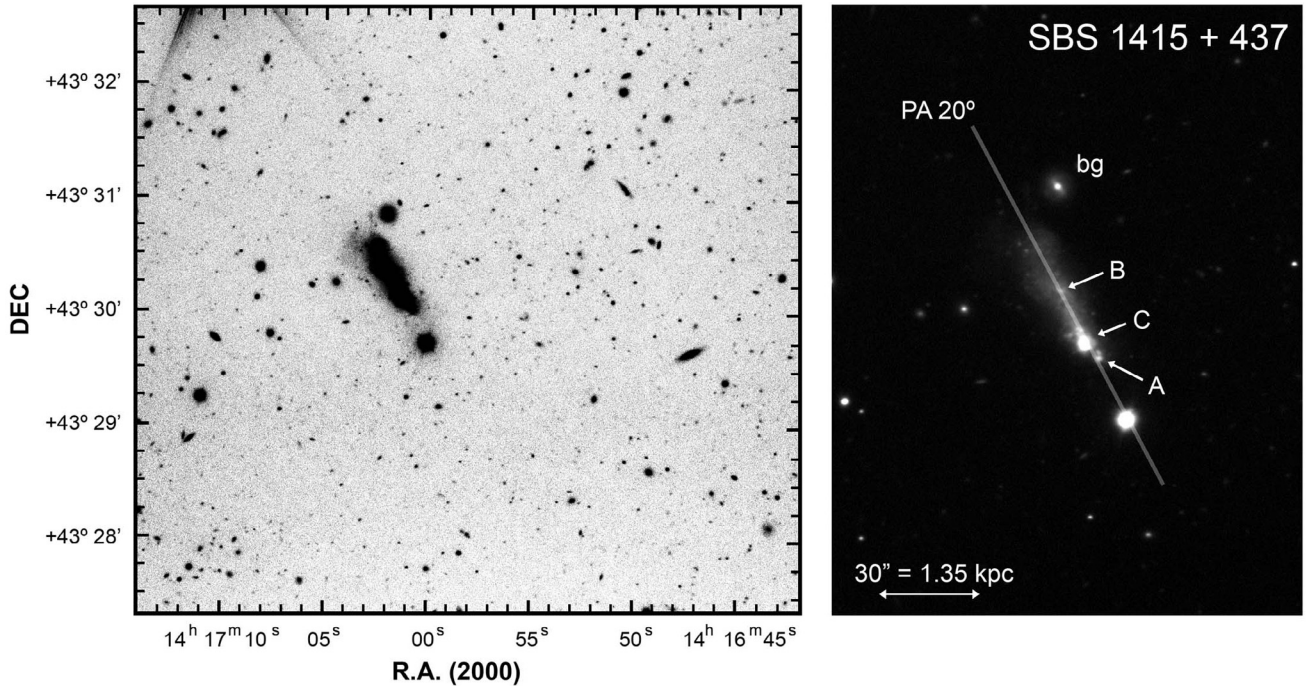

Fig. 25. Deep image of SBS 1415+437 combining all *U*, *B*, *V* and *R* data (2.56 m NOT). *At the left*, the field surrounding the galaxy is shown. The image has been saturated in order to observe the faintest objects. *At the right*, the non-saturated image of the galaxy indicates the most important regions and the slit position used to obtain the spectroscopic data at the 4.2 m WHT.

3.14.2. Hα photometry

The continuum-subtracted Hα emission of SBS 1319+579 is shown in Fig. 24. The apparent disconnection between regions A-B-d-e (SW area) and C-f-g-h (NE) is noticed in this image. At the SE of C, we detect the faint knot i, hardly observed in the broad-band optical filters. No additional Hα-emitting objects were found in the field of the image. The total Hα flux of SBS 1319+579 is $(2.40 \pm 0.15) \times 10^{-13}$ erg cm^{-2} s^{-1}, which is the first estimate for this galaxy. The number of O7V equivalent stars needed to explain its Hα luminosity is ~17 500. We derive $SFR_{\mathrm{H}\alpha} \sim 0.19\ M_{\odot}\,\mathrm{yr}^{-1}$, the first determination of this quantity in this galaxy. The upper limit of the 1.4 GHz flux suggests $SFR_{1.4\ \mathrm{GHz}} < 0.07\ M_{\odot}\,\mathrm{yr}^{-1}$, and our revision of the IRAS maps indicates $SFR_{\mathrm{FIR}} \sim 0.07\ M_{\odot}\,\mathrm{yr}^{-1}$ and $SFR_{60\,\mu\mathrm{m}} \sim 0.04\ M_{\odot}\,\mathrm{yr}^{-1}$, values about three times smaller than $SFR_{\mathrm{H}\alpha}$. The Hα equivalent widths agree with those obtained using our spectroscopic data. We remark that the high equivalent width of object A, $W_{\mathrm{H}\alpha} \sim 1300$ Å, suggests an age of 3.6 Myr for the last star-forming burst.

3.15. SBS 1415+437

SBS 1415+437 is one of the most metal-poor BCDGs known. It was included in the Morphologic Catalogue of Galaxies (MCG) performed by Vorontsov-Velyaminov & Arkhipova (1964) and in the Volume III of the Zwicky catalogue (Zwicky & Herzog 1966). Its photometric properties were analyzed in detail by Guseva et al. (2003). Gil de Paz et al. (2003, 2005) and Gronwall et al. (2004) presented Hα data. Aloisi et al. (2005) observed individual stars and made a color-magnitude diagram of the galaxy using very deep observations obtained using the *Advanced Camera for Surveys* at the HST.

3.15.1. Broad-band photometry

At the distance at which SBS 1415 + 457 is located (9.3 Mpc), 1″ is equivalent to 45 pc. Our deep image (Fig. 25) shows the elongated comet-like structure of the galaxy, which is 45″ (2025 pc) long and 10″ (450 pc) wide at its SW edge (15″ = 675 pc wide at its NE edge). The brightest regions are located towards the SW of the system; the most important is C. At a distance of 6.5″ (290 pc) is located A, whereas B is located 17″ (765 pc) towards the NE of C. The approximately elliptical structure of the galaxy is disrupted towards the east. At 10″ towards the north there is a circular object (bg) with a strong central knot and an apparent bar, which is a background galaxy.

The absolute magnitude of SBS 1415+457 ($M_B = -14.52$) implies that it is a dwarf galaxy. The colors shown by its brightest regions are blue, but they are slightly redder if we consider the flux of all of the galaxy. This fact indicates the existence of a low-luminosity component dominated by older stellar populations. The analysis of the colors in the NE region of the galaxy, which is free of H II regions, confirm the existence of this evolved stellar population. Comparing with the predictions of population synthesis models, we estimate an age of between 150 and 250 Myr for this component, which agrees with the result of Guseva et al. (2003).

3.15.2. Hα photometry

In Fig. 26, we show the contour map of our continuum-subtracted Hα image in comparison with the contour maps in the broad-band *B* and *J* filters. The three main regions are easily distinguished: C and A sharing the same Hα envelope and B detached from them. However, the Hα emission appears to be more extended than the bright region we see in the broad-band images, suggesting the existence of some star-forming regions at the E and W that were not detected before. They are indicated with

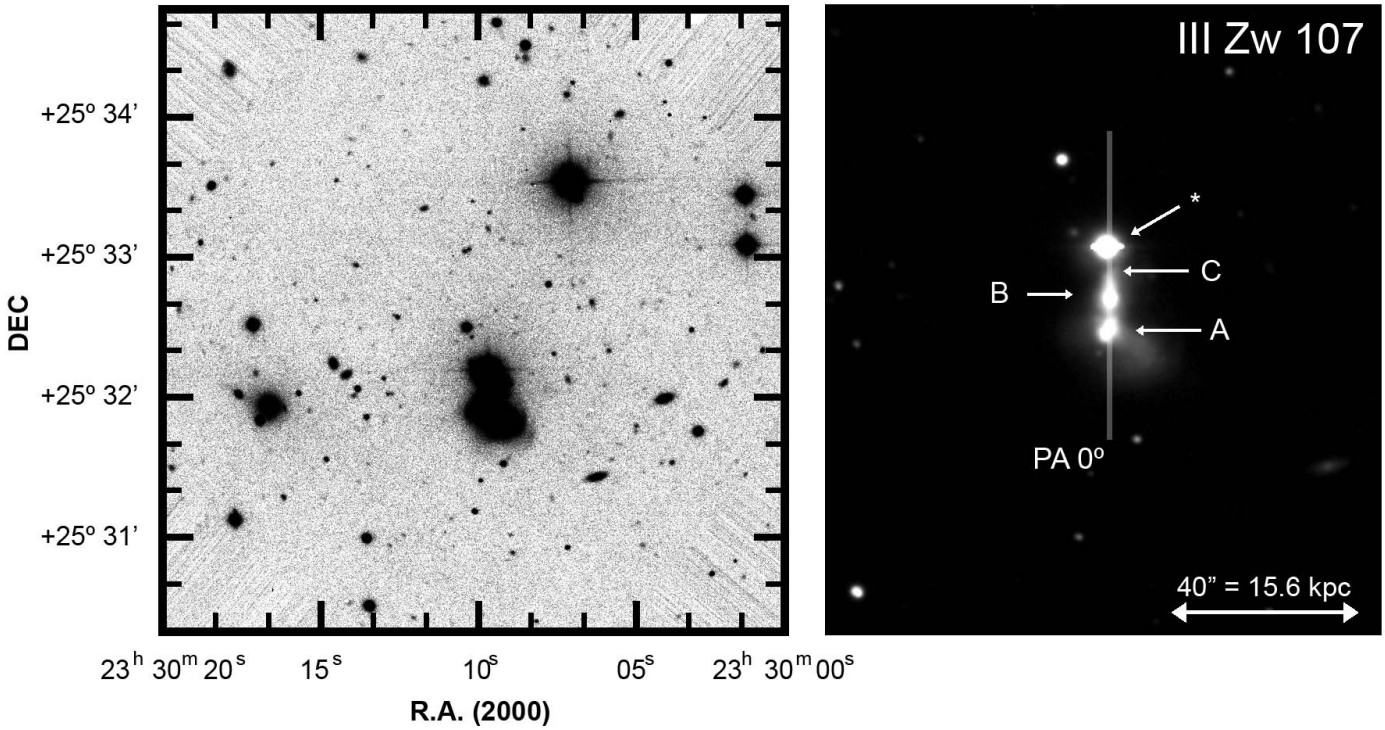

Fig. 27. Deep image of III Zw 107 obtained by adding all exposures in *B* and *R* (2.2 m CAHA) and *U* and *V* (2.5 m INT) broad-band filters. *The left image* was saturated to show the faintest objects surrounding the galaxy, as well as the tail at the south turning to the west. *On the right*, the non-saturated image of the galaxy is shown, indicating the slit position used to obtain the spectroscopic data at the 2.5 m INT.

two arrows in Fig. 26, as well as the position of knot d. The total Hα flux for SBS 1319+437 is $(4.8 \pm 0.2) \times 10^{-13}$ erg cm^{-2} s^{-1}, in excellent agreement with that determined by Gil de Paz et al. (2003), $(5.0 \pm 0.6) \times 10^{-13}$ erg cm^{-2} s^{-1}. The number of O7V equivalent stars is slightly higher than 3600. We derive a star formation rate of $SFR_{\mathrm{H}\alpha} \sim 0.04$ $M_\odot$ yr^{-1}. There are no additional *FIR* and 1.4 GHz data that we can use to obtain an independent estimate of the star formation rate in this object, although the upper limit of the 1.4 GHz luminosity indicates $SFR_{1.4\ \mathrm{GHz}} < 0.01$ $M_\odot$ yr^{-1}. The Hα equivalent widths found in the central objects are high, indicating an age of between 3.5 and 4 Myr for the most recent star-formation burst, in agreement with the age derived from the optical colors of these regions.

3.16. III Zw 107

The galaxy III Zw 107, previously included in the VI Volume of the *Catalogue of Galaxies and of Clusters of Galaxies* performed by Zwicky & Kowal (1968), was named after the *Catalogue of Selected Compact Galaxies and of Post-Eruptive Galaxies* performed by Zwicky (1971), who described it as a *blue post-eruptive osculating pair of compacts with plumes [south-west]*. It is included in the *Survey of emission-line galaxies* performed by the Universidad Complutense de Madrid (Zamorano et al. 1994, 1996). Photometric analyses of III Zw 107 were completed by Moles et al. (1987) and Cairós et al. (2001a,b); these last authors also obtained Hα imagery.

3.16.1. Broad-band photometry

III Zw 107 is located at 79.6 Mpc. At that distance, 1″ is equivalent to 390 pc. Our deep image (Fig. 27) shows a diffuse object showing two independent regions (A and B) close to a bright star. These two bright knots, separated by 6.6″ (2.5 kpc), are embedded in an irregular envelope that is not orientated in the same direction. From southern region A a prominent tail, emerges that reaches a distance of 19″ (7.4 kpc). We note that B is slightly curved, following the orientation of the common envelope. Just to the north of B lies knot C, hardly detected by the broad-band filter imaging but evident in our Hα image and in our spectra. A bright star prohibits the observation of the northern area of III Zw 107.

We analyzed knots B and C by considering them to be the same region (B + C) because they are hardly separated in broad-band filters, but used the average value of the $C(\mathrm{H}\beta)$ to correct this single object for extinction. The absolute *B* magnitude of the object, $M_B = -20.14$, indicates that it is not a dwarf galaxy. The colors of the regions A and B + C are blue, indicating that the dominant young population has an age of between 5 and 10 Myr. However, the colors found in the tail and the low-luminosity component (UC) are redder, implying that an old stellar population (of age ≥500 Myr) is also present in the galaxy.

3.16.2. Hα photometry

The continuum-subtracted Hα image (Fig. 28) of III Zw 107 shows three independent and bright knots corresponding to regions observed in the broad-band filters. Region A is more extended that we expect on the basis of its emission in broad-band filters, the Hα-emission is extended to the east in the opposite direction of the tail, as previously noted by Cairós et al. (2001a). The total Hα flux of III Zw 107 is $(5.29 \pm 0.24) \times 10^{-13}$ erg cm^{-2} s^{-1}, slightly higher than given by Cairós et al. (2001a), $f_{\mathrm{H}\alpha} = (4.16 \pm 0.07) \times 10^{-13}$ erg cm^{-2} s^{-1}. Considering its distance, around 300 000 O7V equivalent stars are needed to explain its total Hα luminosity. We estimate an Hα-based star formation rate of 3.19 ± 0.15 $M_\odot$ yr^{-1}, similar although slightly higher that the values obtained using

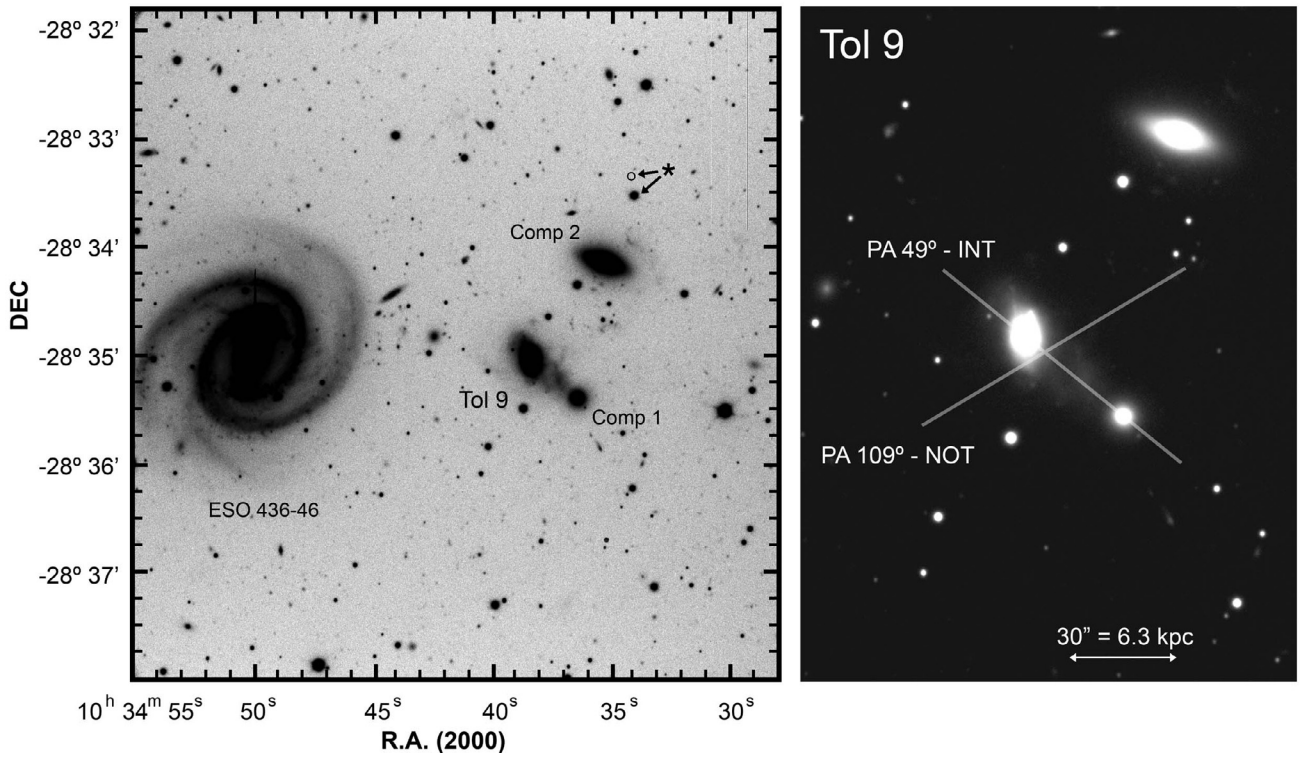

Fig. 29. Deep image of Tol 9 and its surrounding in the *V* filter (2.56 m NOT). *At the left*, a saturated image of the field surrounding the galaxy is shown. Some nearby objects are identified, remarking the beautiful barred spiral ESO 436-46. A star that seems to have a high proper movement is shown with an asterisk (see text). The non-saturated image at the right shows an enlargement of Tol 9. The slit positions used to obtain the spectroscopic data have been included. The slit position observed using the 2.56 m NOT (AP 109°) was intentionally located not crossing the center of Tol 9: its main purpose was the measurement of the velocity field of the extended Hα structure found in the galaxy (see Fig. 30).

the *FIR* fluxes, i.e. $SFR_{\rm FIR} = 2.26 \pm 0.36\ M_\odot\,{\rm yr}^{-1}$ and $SFR_{60\mu{\rm m}} = 2.04 \pm 0.30\ M_\odot\,{\rm yr}^{-1}$. All of these values are higher than the estimate using the 1.4 GHz radio-continuum flux, $SFR_{1.4\ {\rm GHz}} = 1.52 \pm 0.09\ M_\odot\,{\rm yr}^{-1}$. The H$\alpha$ equivalent widths suggest a young age for the most recent star-formation burst (~5.5 Myr in A), although is not as young as this found for other galaxies in this work. The non-thermal flux at 1.4 GHz is almost 92%.

3.17. Tol 9

Tol 9 is an emission-line galaxy discovered by Smith et al. (1976). Its nature was analyzed with Tololo galaxies known to date by Bohuski et al. (1978), who concluded that the emission lines detected in more than 80% of these galaxies appear to be a consequence of massive stars. Wamsteker et al. (1985) detected Hα emission and remarked that Tol 9 interacts with a nearby object. Bergvall & Olofsson (1986) studied Tol 9 using both optical and *NIR* broad-band photometry and spectroscopy. Tol 9 belongs to the Hydra I cluster, also known as Abel 1060 (Richter 1987, 1989). It also belongs to the Klemola 13 (HIPASS J1034-28) group, an H I-rich group following the data provided by the HIPASS survey (Meyer et al. 2004).

3.17.1. Broad-band photometry

Tol 9 is located at 43.3 Mpc, and 1″ is therefore equivalent to 210 pc. Figure 29 shows our deep *V* image of the galaxy and its surroundings identifying all important objects. Following NED, Tol 9 is classified as an E4 galaxy (because of its morphology) but also as H II galaxy (because of its nebular emission). It has an approximate size of 23″ × 14″ (4.8 × 3.0 kpc). As others authors previously noted, it shows a kind of tail at its SW, in the direction of a dwarf nearby companion galaxy (comp 1) that has a spherical shape and is located at 28″ (5.9 kpc). This bridge suggests some kind of interaction between both objects. Tol 9 is also close to another elliptical galaxy located at 56″ (11.8 kpc) towards the NW (comp 2) that appears to show some evidence of disrupted material in its northwest area. We also detect some faint structures perpendicular to the tail of Tol 9, which correspond to the Hα emission that we clearly detect embedded Tol 9 (Fig. 30). The minimum distance between Tol 9 and the spiral ESO 436-46 is 96″ (20.2 kpc).

Tol 9 cannot be classified as a dwarf galaxy because of its absolute magnitude ($M_B = -19.26$). It has bluer colors than the remainder of the objects in the field, although they are not so blue as other objects of this work. Tol 9 hosts a population of young stars with ages lower than 50 Myr, and a ~500 Myr-old underlying stellar component. The companion galaxies (comp 1 and 2) are dominated by old stars, without any recent star formation. The *NIR* colors of these three galaxies (Tol 9, comp 1 and 2) are completely dominated by the emission of the old stellar population. Our *NIR* colors agree with those derived by using both 2MASS and 3.9 m AAT (Ward et al. 1982).

3.17.2. Hα photometry

The continuum-subtracted Hα image (Fig. 30) indicates that Tol 9 contains a large amount of nebular emission. Two opposite structures (#3 and #5) are located almost perpendicular to the tail that connect Tol 9 with comp 1. Besides these objects, several smaller regions, in particular the semi-arc #4 located to

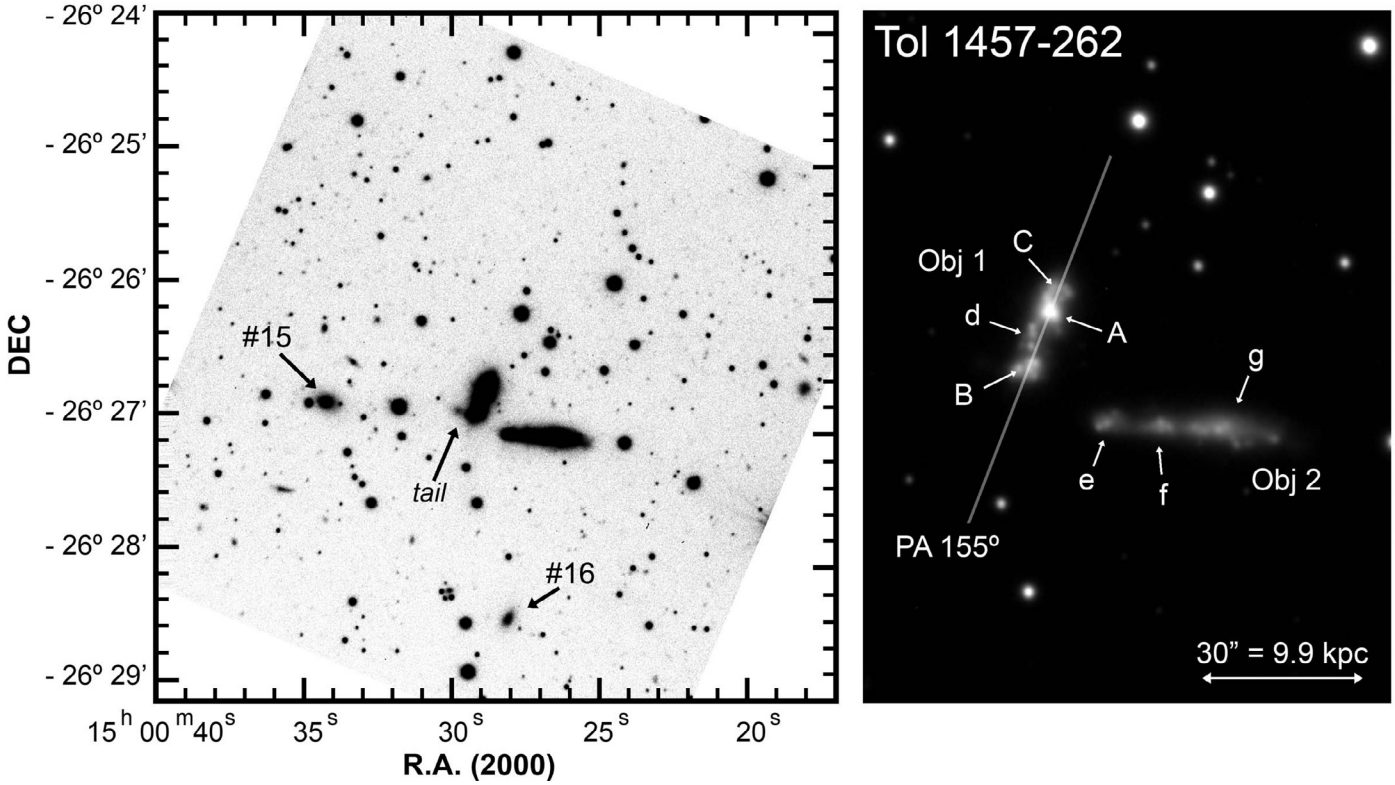

Fig. 31. Deep image of the pair of objects that form Tol 1457-262 created by adding all exposures in *U*, *B*, *V*, and *R* filters (2.56 m NOT). *On the left*, the field surrounding the galaxies is shown. The image was saturated to detect the faintest objects; the most important were identified to be #15 (that shows strong Hα emission) and #16 (probably also associated with the system). A diffuse tail towards the SE of the main object is also indicated. The non-saturated image *on the right* shows the internal structure of the two main objects. The slit position used to obtain the spectroscopic data was indicated, as well as the location of the three regions (A, B, and C) studied by spectroscopy.

the south, are also detected. The center of the galaxy has strong Hα emission, and emission knots #1 and #2 are located to its north. The image seems to show some faint filaments connecting the central region with #5 and #1. At around 38″ (7.9 kpc) towards the NW of Tol 9, faint knot #6, aligned with region #5, is found. The interesting Hα structure discovered in Tol 9 and its lack of detectable emission in broad-band filters suggests the presence of some kind of galactic wind in this galaxy.

The correction for [N II] emission is important in Tol 9, corresponding to 28% of the total Hα flux. Besides the central region and objects indicated in Fig. 30, we also included the flux value of the common envelope (Env in Table 7) of ionized gas surrounding the galaxy. The total Hα flux is $(10.2 \pm 0.7) \times 10^{-13}$ erg cm^{-2} s^{-1}, similar to that derived by Bennett & Moss (1998), $f_{\mathrm{H}\alpha} \sim 8.5 \times 10^{-13}$ erg cm^{-2} s^{-1}. Around 168 000 O7V equivalent stars are needed to explain this Hα luminosity. Its Hα-based star formation rate is $SFR_{\mathrm{H}\alpha} = 1.82 \pm 0.13$ $M_\odot$ yr^{-1}, similar to measurements obtained using the *FIR* and 1.4 GHz radio-continuum data, i.e. $SFR_{60\,\mu\mathrm{m}} = 1.2 \pm 0.1$ $M_\odot$ yr^{-1}, $SFR_{\mathrm{FIR}} < 1.59$ $M_\odot$ yr^{-1} and $SFR_{1.4\ \mathrm{GHz}} = 2.18 \pm 0.04$ $M_\odot$ yr^{-1}. The Hα equivalent width determined for the central region indicates an age of 5.8 Myr for the last star-formation burst. This age is younger than that derived from the optical colors.

We did no detect any nebular emission in the remainder of the objects in the field, appart from a strange nearby star (⋆ in Fig. 29). This object is stellar because the size of its PSF-*FWHM* is equivalent to other stars in the field. The Hα emission is significant. Furthermore, if we compare our image with that given by the DSS (obtained on 10/05/75), we observe that this star has moved around 11″ towards the south, and therefore has a significant proper motion of about 0.37″.

3.18. Tol 1457-262

Tol 1457-262 is a pair of close objects that have significant star formation activity. Its name is derived from the survey performed by Smith et al. (1976) using the 61 cm Curtis Schmidt telescope (CTIO, Chile). Campbell & Terlevich (1984) studied its *NIR* colors, and Arp & Madore (1987) included this object in their *Catalogue of southern peculiar galaxies and associations*.

3.18.1. Broad-band photometry

Tol 1457-262 is located at 68.1 Mpc, at which one arcsec corresponds to 0.33 kpc. Figure 31 shows two close objects (the minimun distance is 12″ = 4 kpc), each one containing several independent bright regions. Names used previously to identify these objects were unclear: following NED, the western object corresponds to Tol 1457-262a (northern region) and Tol 1457-262b (southern region), while Tol 1457-262c and Tol1457-262d are located close to the eastern object. However, other authors use different designations. Taking into account our deep images, we consider *Object 1* (western) to consist of regions A (the brightest), B (at 11″ = 3.6 kpc to the south from A) and C (at 4″ = 1.3 kpc to the north from A). Between A and B we identify other knots, which we name jointly to be *d*. The *object 2* (eastern) is subdivided into *e, f* and *g*. We detect a faint tail starting at the south of *object 1* and going towards the east, out to

a distance of 8.5″ (2.8 kpc). Approximately 68″ (22.4 kpc) in that direction, the circular object #15 of size 8″ (2.6 kpc), can also be found. Our Hα image reveals that is contains significant nebular emission. Located at 83″ (27.4 kpc) towards the south, object #16 also appears to show Hα emission. Therefore, both objects could be physically associated with or close to Tol 1457-262.

For all knots apart from A, the $E(B-V)$ estimated from our spectroscopic data are lower than derived from the Galactic extinction maps; we therefore use the Galactic value to correct for extinction. The absolute B-magnitude computed in the two main objects ($M_B = -19.73$ and -18.97) do not allow us to classify them as dwarf galaxies, but #15 ($M_B = -16.48$) and #16 ($M_B = -14.69$) are indeed dwarf galaxies. The optical colors of all knots are blue, especially region A for which we estimate an age lower than 5 Myr for the last star-forming episode. However, the *NIR* colors (which are similar within the errors to those computed by Campbell & Terlevich 1984) suggest the existence of an important underlying old stellar population. Nebular-free regions (UC) show red colors consistent with the presence of stars older than 500 Myr. Object #15, which contains a significant population of young stars ($U-B \sim -0.25$) and considerable Hα emission, is dominated by an old stellar population. The same situation is found for #16, which contains a dominant old stellar population.

3.18.2. Hα photometry

The comparison of the continuum-subtracted Hα image with the optical/*NIR* images (Fig. 32) indicates the strong Hα emission hosted by Tol 1457-262. Figure 33 (left) shows a detailed map of the Hα emission in these objects. All star-forming regions are identified in this figure: #6 is the region A that we analyzed in both broad-band images and spectroscopy, #3 is region B , #7 is region C, and knots #4 and #5 form region *d*. Knots within *object 1* are not aligned with its main optical axis but form a sinusoidal structure. Concerning *object 2*, two alignments are found within it: #9 (*e* in broad-band filters), #10 (*f*), #11 and #12 to the east, and #13 (composed by two smaller knots) and #14 to the west. Knots #11, #12, #13, and #14 form region *g* analyzed in broad-band filters.

We detect considerable Hα emission in #15 (Fig. 33), indicating that it has a similar radial velocity and is probably physically associated with Tol 1457-262. Surprisingly, it is aligned with the main axis of *object 2* and the optical tail observed at the south of *object 1*. We also detect some nebular emission in #16, at larger distance from Tol 1457-262. Although the signal-to-noise ratio of its Hα emission image is low, we consider the detection to be reliable because the stellar field has disappeared in our net Hα image: only a faint residual signal (with fewer counts than obtained in #16) is found in the brightest star of the field (*star* in Fig. 33 right).

The total Hα flux of Tol 1457-262 (no considering #15 and #16) is $(11.4 \pm 0.6) \times 10^{-13}$ erg cm^{-2} s^{-1}, indicating that more than 465000 O7V equivalent stars are needed to explain its Hα luminosity. The H II mass is $(41 \pm 2) \times 10^6$ $M_\odot$, and its Hα-based star-formation rate is $SFR_{\rm H\alpha} = 5.0 \pm 0.3$ $M_\odot$ yr^{-1}. The SFR derived using the 1.4 GHz flux of $SFR_{1.4\ \rm GHz} = 5.4$ $M_\odot$ yr^{-1} agrees with this value, although it is slightly higher than expected from the *FIR* data, $SFR_{\rm FIR} = 3.7$ $M_\odot$ yr^{-1} and $SFR_{60\,\mu\rm m} = 3.4$ $M_\odot$ yr^{-1}. The non-thermal flux at 1.4 GHz corresponds to almost 97% of the total. The equivalent widths are large (specially for A), representing ages younger than 5 Myr in the last burst episode. All these values confirm the intense star formation activity that all the system is experiencing.

3.19. Arp 252

Arp 252 is an interesting object listed in the *Atlas of Peculiar Galaxies* (Arp 1966) and in the *Morphological Catalogue of Galaxies* (Vorontsov-Velyaminov & Arkhipova 1968), where it is described as a system of two galaxies separated by 55″, in evident interaction, with a long tail at the south. Arp 252 in fact consists of two galaxies: ESO 566-7 (southern object) and ESO 566-8 (northern object). The colors of the tidal tails were analyzed by Schombert et al. (1990).

3.19.1. Broad-band photometry

Arp 252 has a distance of 129.8 Mpc which 1″ is equivalent to 0.63 kpc. Figure 34 shows our deep image identifying the two galaxies ESO 566-8 (A, the brightest) and ESO 566-7 (B), separated by 50″ (31.5 kpc). The two long tidal tails are definitely a consequence of the gravitational interaction between the galaxies. The southern tail (BtS, *B tail South*), which is the most prominent, is twisted and reaches a distance of 45″ (28.4 kpc) from the center of B. The northern tail (At, *A tail*) is less extended and reaches a distance of 38″ (23.9 kpc). BtS seems to be in the projected plane of the sky, but At may have a significant inclination. Some diffuse material (BtN, *B tail North*) and several knots are detected between A and B. The central region of ESO 566-7 (Bcen) has a thin arc starting in its western region, turning to the north, and ending at the south of the eastern areas, after completing an angle of around 210°. ESO 566-8 shows a short, blue, broken plume (region a2 in Fig. 35) located in the opposite direction of BtN.

The central regions of both galaxies have relatively blue color (in comparison with models, the ages are between 10 and 100 Myr old), but their integrated colors (including the tails) are red. The tails are only detected in B, V, R, and J filters; BtS and BtN are also observed in U. Their colors are red, indicating that they consists of stars with ages far older than 500 Myr. However, the knots found between the two galaxies (c) and the end-tip knot in the southern tail (d) have blue colors and nebular emission, indicating that they are forming stars.

3.19.2. Hα photometry

Our continuum-subtracted Hα image of Arp 252 (Fig. 35) reveals that the centers of both galaxies have intense nebular emission. ESO 566-7 (B) consists of two knots with similar intensity (b1 and b2), although a fainter object (b3) is located towards the east. ESO 566-8 (A) shows brighter Hα emission in its central region (a1) but also in a nearby knot (a2) located to the NW. We detect nebular emission perpendicular to the main axis orientation in our optical and *NIR* broad-band images (indicated by a discontinuous line in Fig. 35). This Hα structure may be formed by galactic winds but this should be investigated. Knot c, located in the ionized debris between A and B, shows considerable Hα emission. We also detect nebular emission in object d located at the end of the southern optical tail. Both knots (c and d) are candidate TDGs because of their properties and position in the system.

Galaxy A emits most of the Hα emission of the entire system, almost 93%. The Hα flux that we derive for Arp 252, considering both galaxies, is $(4.5 \pm 0.3) \times 10^{-13}$ erg cm^{-2} s^{-1},

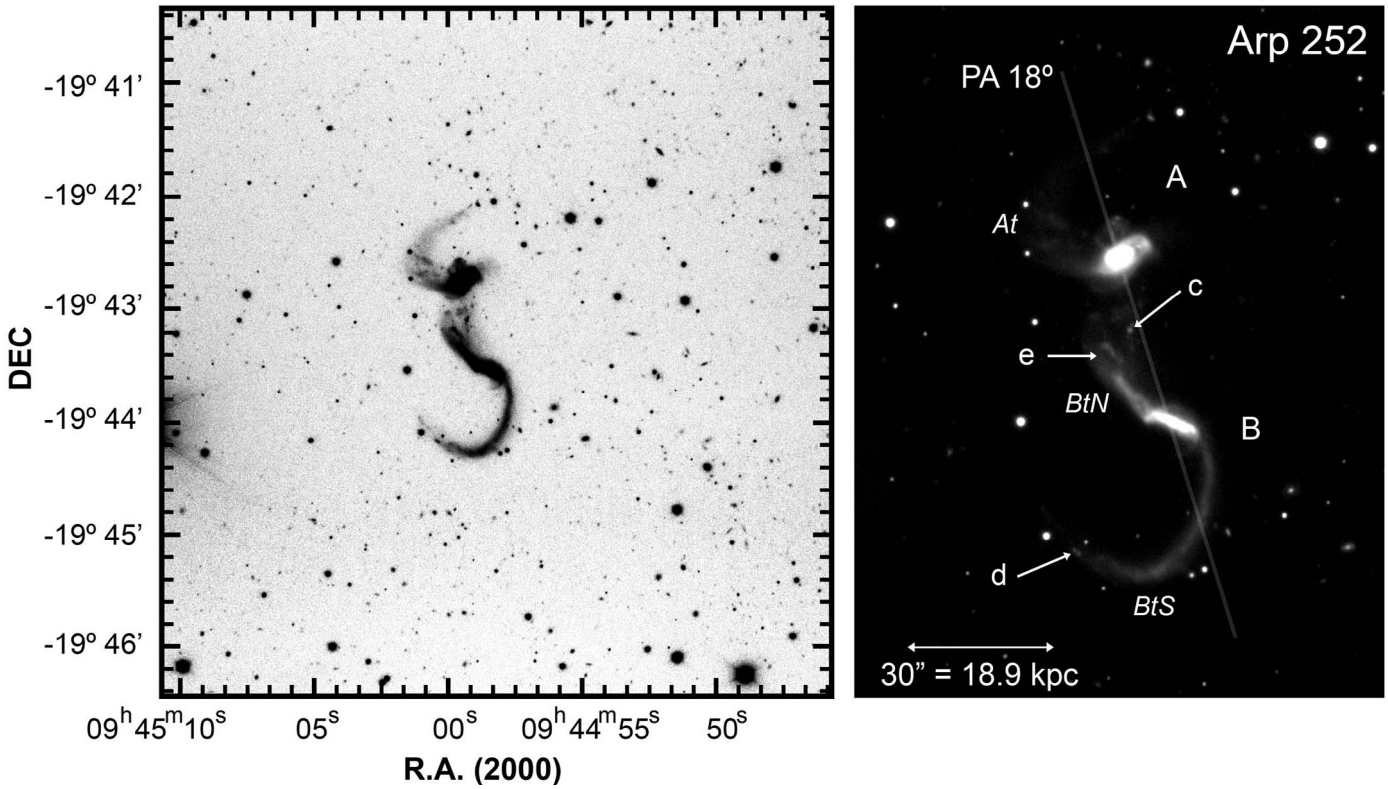

Fig. 34. Deep image of the interacting galaxy pair Arp 252 obtained by adding all exposures in U, B, V, and R filters (2.56 m NOT). *On the left*, the field surrounding the galaxy is shown; the image was saturated to enhance the faintest objects, in particular the two long tidal tails. The non-saturated image *on the right* shows the internal regions of the galaxies A (ESO 566-8) and B (ESO 566-7). The slit position used to obtain the spectroscopic data is also indicated.

which is considerably high considering the distance to the system. More than 660 000 O7V equivalent stars are needed to explain the total Hα luminosity. The total mass of ionized gas, $M_{\rm H\,II} = (13 \pm 1) \times 10^6$ $M_\odot$, and its star-formation rate, $SFR_{\rm H\alpha} = 7.2 \pm 0.5$ $M_\odot$, are also very high. The *FIR* data associated with ESO 566-8 imply star-formation rate values of $SFR_{\rm FIR} = 16.2$ $M_\odot\,{\rm yr}^{-1}$ and $SFR_{60\,\mu{\rm m}} = 15.5$ $M_\odot\,{\rm yr}^{-1}$, while the 1.4 GHz radio-continuum data indicates a higher value of $SFR_{1.4\ {\rm GHz}} = 49$ $M_\odot\,{\rm yr}^{-1}$. Our Hα fluxes are therefore maybe underestimated. ESO 566-8 has the highest 1.4 GHz luminosity of all galaxies analyzed in this wotk. This fact is probable related to the detection of the galaxy at 4.85 GHz (Griffith et al. 1994). The spectral index between both frequencies is $\alpha = -0.23$. The *FIR*-radio correlation is not satisfied in this object, suggesting that, besides the starburst, it hosts another type of activity. The Hα equivalent widths indicate ages of about 5 Myr for the most recent star-forming bursts, hence younger than those estimated from optical colors.

3.20. NGC 5253

NGC 5253 is a nearby (4.0 Mpc, Karachentsev et al. 2004) BCDG that was intensively studied in all wavelengths. Our study focused mainly on deep *Very Large Telescope* echelle spectrophotometry presented by López-Sánchez et al. (2007), but we compile in Tables 5 and 7 its photometric measurements. The data were adapted from the optical/*NIR* and Hα values given by NED and Meurer et al. (2006), respectively, using our spectroscopic values to correct for extinction and nebular emission.

4. Summary

We have presented a detailed photometric analysis in optical/*NIR* broad-band filters and Hα imagery of a sample of 20 Wolf-Rayet galaxies. We have analyzed the morphology of the galaxies, detecting interaction features in the majority (15 up to 20) of them, including disturbed morphology (HCG 31, POX 4, Tol 1457-262), prominent tails (HCG 31, Mkn 1087, IRAS 08208+2816, UM 420, SBS 0948+532, Arp 252), mergers (HCG 31, Haro 15, Mkn 1199, SBS 0926+606A), and other faint characteristic such as plumes or bridges (Haro 15, IRAS 08339+6517, SBS 0926+606B, SBS 1211+540, III Zw 107, Tol 9, Tol 1457-262). Only 5 objects (Mkn 5, SBS 1054+365, SBS 1319+579, SBS 1415+437 & NGC 5253) do not show remarkable optical/*NIR* morphological features.

We have analyzed the optical/*NIR* colors of the galaxies and selected regions/objects within/surrounding them. Magnitudes have been corrected for extinction using the $E(B-V)$ estimated from our optical spectra (and not only for Milky Way extinction as is usual in this type of study). After this study, only 6 galaxies (Mkn 5, SBS 0926+606, SBS 1054+365, SBS 1211+540, SBS 1415+437 and NGC 5253) are strictly dwarf ($M_B^0 \geq -18$), but other 3 (POX 4, SBS 0948+532 and SBS 1319+579) can also be considered dwarf galaxies ($M_B^0 \geq -19$). However, we must keep in mind that the B magnitude of a starburst is increased by several magnitudes during the first 10 Myr with respect to its brightness in the quiescent phase (see López-Sánchez et al. 2004a, Sect. 4.4, for an extended discussion).

We have corrected our broad-band optical colors for the line emission of ionized gas using data provided by our spectra. Figure 36 illustrates this effect. We compare the predictions

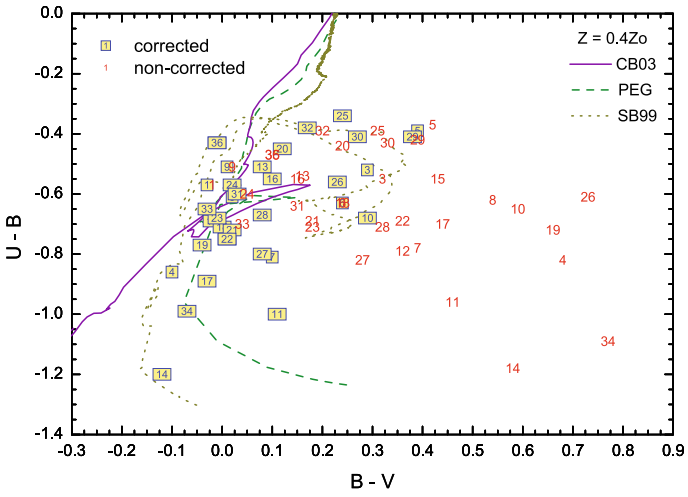

Fig. 36. Color–color diagram comparing the predictions given by evolutionary synthesis models (continous line: BC03 Bruzual & Charlot 2003, models; discontinuous line: PEGASE.2 Fioc & Rocca-Volmerange 1997, models; dotted line: STARBURST99 Leitherer et al. 1999, models), assuming $Z = 0.4\ Z_{\odot}$, with the optical reddening-corrected data obtained from objects of our study. Numbers corresponds to the objects compiled in Table 6. The numbers in boxes represent the position of objects after correction for line emission contribution; numbers without boxes represent the position of the same objects before the correction.

given by evolutionary synthesis models (BC03; Bruzual & Charlot 2003; PEGASE.2; Fioc & Rocca-Volmerange 1997; STARBURST99; Leitherer et al. 1999), assuming $Z = 0.4\ Z_{\odot}$ (the most common value of metallicity for these galaxies) with the optical reddening-corrected data obtained from objects of our study without and with the correction for the emission line contribution (data from Table 6). The effect is evident, in that the data for many objects do not agree with the predictions given by the models but agree after is applied this correction. We remark that this contribution is more important in compact objects and/or objects with intense nebular emission.

We have compared the optical/NIR colors with the predictions given by the theoretical models. We have found a relatively good correspondence (see Fig. 37, top) between the optical data and the models, especially for compact and dwarf objects such as HCG 31 F1 or SBS 0948+532, the ages being consistent with a recent star-formation event (≤100 Myr). However, there are significant differences (~0.2 mag or even higher) in some cases. This discordance is always observed in galaxies hosting a considerable population of older stars (Mkn 1199, Mkn 5, Tol 1457-262 #15 and #16, ESO 566-7), and their luminosities contribute to the $B - V$ color (the U magnitude is barely affected by older stellar populations). We can check this effect by taking into account the colors of the bursts and those derived for the underlying stellar population (this was not possible for all galaxies) separately, as shown in the bottom of Fig. 37, bottom. The correspondence between models and optical data has improved and all inferred ages of the most recent star-formation burst are lower than 25 Myr. We find some discrepances, for example, in Haro 15 and Mkn 1199 (the starburst activity is located at the centre of these galaxies), UM 420 (probably because we are observing this object through the stellar disk of the nearby spiral galaxy UGC 1809; see Fig. 13) and POX 4 (data adapted from Méndez & Esteban 1999, who highlighted the importance of the underlying stellar population). The data corresponding to the underlying component suggest ages higher than 100 Myr. In

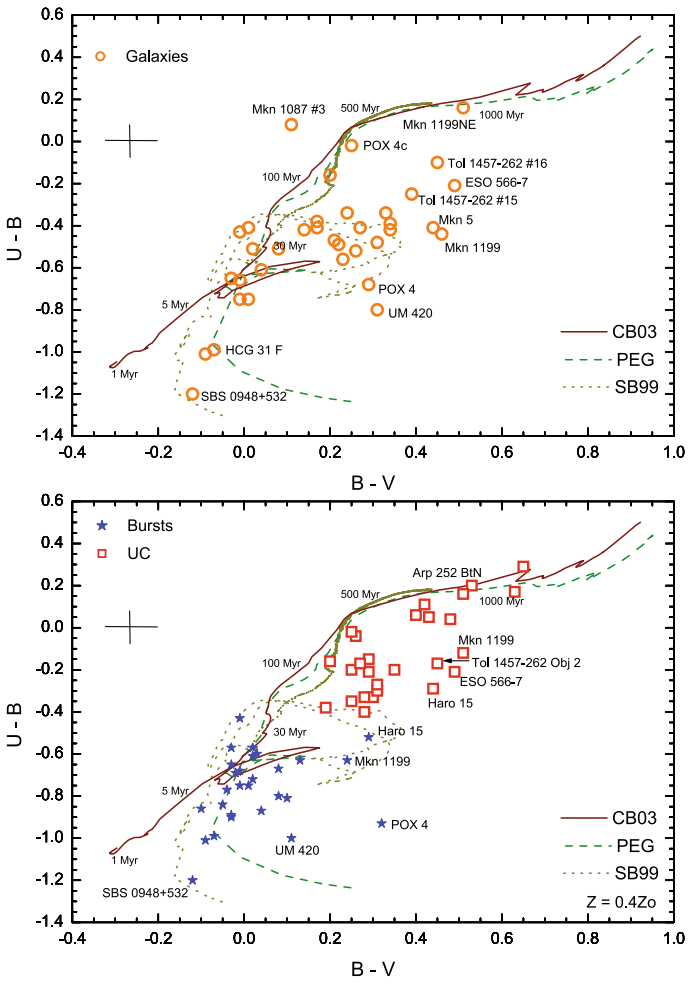

Fig. 37. $U - B$ vs. $B - V$ diagrams comparing the predictions given by evolutionary synthesis models (see Fig. 36) with the colors (corrected for both reddening and contribution of the emission lines) obtained from the galaxies of our sample (*top*) and when the burst (*blue stars*) and underlying component (UC, *red squares*) of each system are considered independently (*bottom*). The cross indicate the typical errors in our data. Some age labels have been included for the BC03 models.

this case, the discrepancies found between models and data are probably caused by a lack of good separation between regions with and without star-formation activity, as a detailed analysis of the surface brightness profiles (i.e. Cairós et al. 2001a; Noeske et al. 2003; Caon et al. 2005) gives.

The agreement between optical/NIR colors of the galaxies and predictions given by theoretical models (Figs. 38, top, and 39, top) is closer than when optical colors alone are considered and indicate older ages than derived from optical colors. This fact is because the older stars dominate the light in the *NIR* range. When bursts and underlying components are considered independently (Figs. 38, bottom, and 39, bottom), their different positions in these diagrams are evident, because the data are in good agreement with the theoretical predictions. We recall that the NIR colors were not corrected for emission-line contribution, but in the bottom of Fig. 39 an arrow indicating this efect is included. The $H - K$ color excess of the bursts in comparison with the models agrees with this effect, $\Delta(H - K) \sim 0.05$, which is similar to that found by Buckalew et al. (2005). However, we found that estimates of the age of the last star-formation episode from NIR colors are slightly older than those obtained from optical colors and significatively older than estimates provided

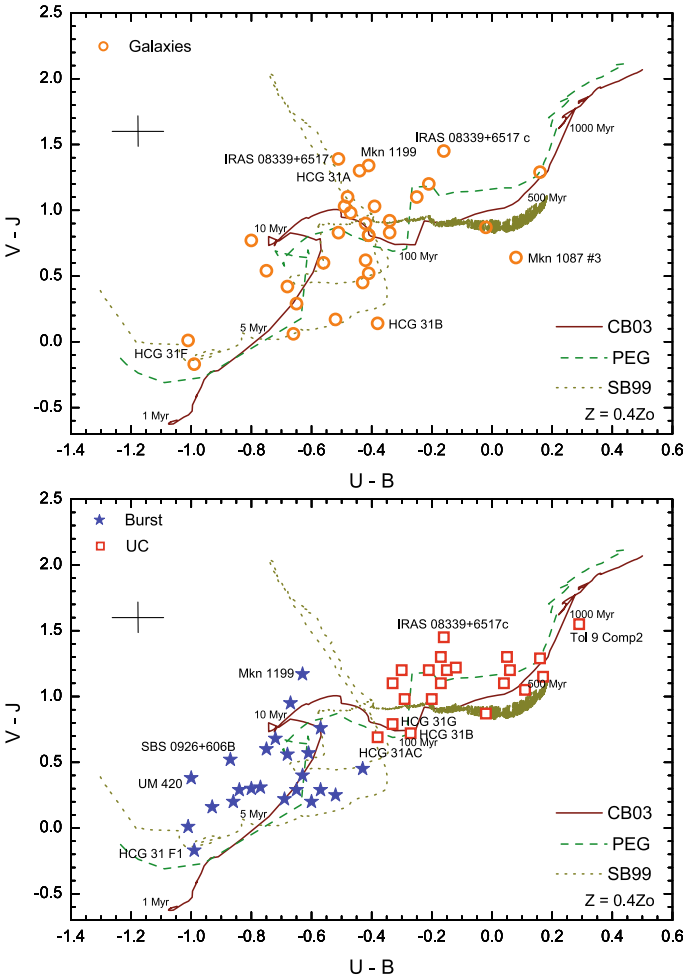

Fig. 38. $V - J$ vs. $U - B$ diagrams comparing the predictions given by evolutionary synthesis models (see Fig. 36) with the colors (corrected for both reddening and contribution of the emission lines) obtained from the galaxies of our sample (*top*) and when the burst (*blue stars*) and underlying component (UC, *red squares*) of each system are considered independently (*bottom*). The cross indicate the typical errors in our data. Some age labels have been included for the BC03 models.

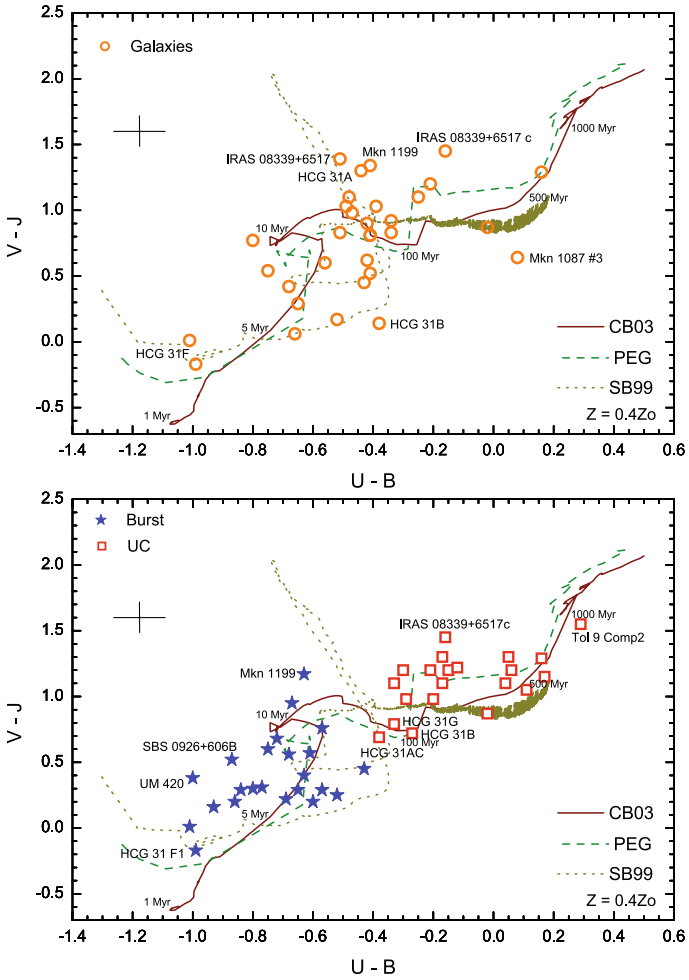

Fig. 39. $J - H$ vs. $H - K_s$ diagrams comparing the predictions given by evolutionary synthesis models (see Fig. 36) with the colors (corrected for both reddening and contribution of the emission lines) obtained from the galaxies of our sample (*top*) and when the burst (*blue stars*) and underlying component (UC, *red squares*) of each system are considered independently (*bottom*). The cross indicate the typical errors in our data. Some age labels have been included for the BC03 models.

by $W(\mathrm{H}\alpha)$. The advantage of using NIR colors in this type of analysis is that we obtain a more accurate estimate of the color of the old stellar populations with ages sometimes higher than 500 Myr.

Using continuum-subtracted Hα maps, we have detected extended ionized gas throughout the galaxies, which is intense in some (HCG 31, Mkn 1087, Haro 15, IRAS 08298+2816, IRAS 08339+6517, POX 4, UM 420, SBS 0926+606, SBS 0948+532, Tol 1457-262). We have found a double-nucleus in SBS 0926+606A, a kind of galactic wind in Tol 9, and one (or two?) nearby star-forming galaxies surrounding Tol 1457-437.

The values of the Hα equivalent widths, $W(\mathrm{H}\alpha)$, derived from the Hα images agree with those obtained from optical spectroscopy (see Paper II). We have estimated the age of the last starbursting episode comparing $W(\mathrm{H}\alpha)$ with the predictions given by STARBURST99 (Leitherer et al. 1999) models. This age estimate is usually younger than obtained using the optical/*NIR* colors. We explain this disagreement as being due to the contribution of older stellar populations in broad-band colors, as we have seen above. After the correction for extinction and contribution of the [N II] $\lambda\lambda$6548, 6583 emission lines, we have computed the Hα flux and luminosity, the mass of ionized gas, the mass of the ionizing stellar cluster, the number of O7V equivalent stars, and the star formation rate in each galaxy and/or Hα-emitting burst. The Hα-based SFR has usually been found to be in agreement with the SFR derived using *FIR* and 1.4 GHz data for the same galaxy. They have however been found to disagree in ESO 566-8 (Arp 252 A), suggesting that, besides the starburst, it hosts another kind of activity. We will discuss the SFR and other Hα-based parameters ($M_{\mathrm{H\,II}}$, $M_\star$) and compare with other properties (i.e. oxygen abundance, H I and total mass, warm dust mass, luminosities) in Paper III.

Acknowledgements. We are indebted to Verónica Melo, Ismael Martínez-Delgado, Mercedes López-Morales, María Jesús Arévalo, Alfred Rosenberg and David Martínez-Delgado for share their observing time with us. Á.R.L.-S. thanks C.E. (his Ph.D. supervisor) for all the help and very valuable explanations, talks and discussions along these years. He also acknowledges Jorge García-Rojas, Sergio Simón-Díaz and José Caballero for their help and friendship during his Ph.D., extending this acknowledge to all people at Instituto de Astrofísica de Canarias (Spain). Á.R.L.-S. *deeply* thanks to Universidad de La Laguna (Tenerife, Spain) for force him to translate his Ph.D. Thesis from English to Spanish; he had to translate it from Spanish to English to complete this publication. The authors are very grateful to A&A language editor, Claire Halliday, for her kind revision of the manuscript. This work has been partially funded by the Spanish Ministerio de Ciencia y Tecnología (MCyT) under project AYA 2004-07466. This research has made use of

the NASA/IPAC Extragalactic Database (NED) which is operated by the Jet Propulsion Laboratory, California Institute of Technology, under contract with the National Aeronautics and Space Administration. This publication makes use of data products from the Two Micron All Sky Survey, which is a joint project of the University of Massachusetts and the Infrared Processing and Analysis Center/California Institute of Technology, funded by the National Aeronautics and Space Administration and the National Science Foundation.

References

Allen, D. A., Wright, A. E., & Goss, W. M. 1976, MNRAS, 177, 91
Allen, S. W. 1995, MNRAS, 276, 947
Aloisi, A., van der Marel, R. P., Mack, J., et al. 2005, ApJ, 631, 45
Arp, H. C. 1966, ApJS, 14, 1
Arp, H. C., & Madore, B. F. 1987, A catalogue of southern peculiar galaxies and associations (Cambridge: Cambridge University Press)
Bergvall, N., & Olofsson, K. 1986, A&AS, 64, 469
Bergvall, N., & Östlin, G. 2002, A&A, 390, 891
Bertelli, G., Bressan, A., Chiosi, C., Fagotto, F., & Nasi, E. 1994, A&AS, 106, 275
Bicay, M. D., Stepanian, J. A., Chavushyan, V. H., et al. 2000, A&AS, 147, 169
Bohuski, T. J., Fairall, A. P., & Weedman, D. W. 1978, ApJ, 221, 776
Bruzual, G., & Charlot, S. 2003, MNRAS, 344, 1000 (BC03)
Buckalew, B. A., Kobulnicky, H. A., & Dufour, R. J. 2005, ApJS, 157, 30
Cairós, L. M., Vílchez, J. M., González Pérez, J. N., Iglesias-Páramo, J., & Caon, N. 2001a, ApJS, 133, 321
Cairós, L. M., Caon, N., Vílchez, J. M., González-Pérez, J. N., & Muñoz-Tuñón, C. 2001b, ApJS, 136, 393
Calzetti, D. 1997, AJ, 113, 162
Calzetti, D., Kinney, A. L., & Storchi-Bergmann, T. 1994, ApJ, 429, 582
Calzetti, D., Bohlin, R. C., Kinney, A. L., Storchi-Bergmann, T., & Heckman, T. M. 1995, ApJ, 443, 136
Campbell, A. W., & Terlevich, R. 1985, MNRAS, 211, 15
Campos-Aguilar, A., Moles, M., & Masegosa, J. 1993, AJ, 106, 1784
Cannon, J. M., & Skillman, E. D. 2004, ApJ, 610, 772
Caon, N., Cairós, L. M., Aguerri, J. A., & Muñóz-Tuñón, C. 2005, ApJS, 157, 218
Cardelli, J. A., Clayton, G. C., & Mathis, J. S. 1989, ApJ, 345, 245
Cedrés, B. 2003, Ph.D. Thesis, Universidad de la Laguna, Spain
Condon, J. J. 1992, ARA&A, 30, 575
Condon, J. J., Cotton, W. D., & Broderick, J. J. 2002, AJ, 124, 675
Conti, P. S. 1991, ApJ, 377, 115
Contini, T., Treyer, M. A., Sullivan, M., & Ellis, R. S. 2002, MNRAS, 330, 75
Cutri, R. M., Nelson, B. O., Huchra, J. P., & Smith, P. S. 2000, BAAS, 32, 1520
Coziol, R., Doyon, R., & Demers, S. 2001, MNRAS, 325, 1081
Deeg, H.-J., Duric, N., & Brinks, E. 1997, A&A, 323, 323
Díaz, A. I. 1999, Ap&SS, 263, 143
Dinerstein, H. L., & Shields, G. A. 1986, ApJ, 311, 45
Dopita, M. A., Kewley, L. J., Heisler, C. A., & Sutherland, R. S. 2000, ApJ, 542, 224
Dopita, M. A., Pereira, M., Kewley, L. J., & Capaccioli, M. 2002, ApJS, 143, 47
Esteban, C., & Méndez, D. I. 1999, A&A, 348, 446
Fernandes, I. F., de Carvalho, R., Contini, T., & Gal, R. R. 2004, MNRAS, 355, 728
Fioc, M., & Rocca-Volmerange, B. 1997, A&A, 326, 950
Fisher, K. B., Huchra, J. P., Strauss, M. A., et al. 1995, ApJS, 100, 69
García-Ruiz, I., Sancisi, R., & Kuijken, K. 2002, A&A, 394, 769
Garnett, D. R. 2004, Lectures on Cosmochemistry: the melting pot of the elements, XIII Canary Islands Winter School of Astrophysics, Puerto de la Cruz, Tenerife, Spain, November 19–30, 2001, ed. C. Esteban, R. J. García López, A. Herrero, & F. Sánchez, Cambridge contemporary astrophysics (Cambridge, UK: Cambridge University Press), 171
Garnett, D. R., Kennicutt, R. C. Jr., Chu, Y.-H., & Skillman, E. D. 1991, ApJ, 373, 458
Gil de Paz, A., & Madore, B. F. 2005, ApJS, 156, 345
Gil de Paz, A., Madore, B. F., & Pevunova, O. 2003, ApJS, 147, 29
González-Delgado, R. M., & Leitherer, C. 1999, ApJS, 125, 479
Gónzalez-Delgado, R. M., Leitherer, C., Heckman, T., et al. 1998, ApJ, 495, 698
González-Delgado, R. M., Heckman, T., & Leitherer, C. 2001, ApJ, 546, 845
Gordon, D., & Gottesman, S. T. 1981, AJ, 86, 161
Gronwall, C., Salzer, J. J., Sarajedini, V. L., et al. 2004, AJ, 127, 1943
Guseva, N., Izotov, Y. I., & Thuan, T. X. 2000, ApJ, 531, 776
Guseva, N. G., Izotov, Y. I., Papaderos, P., et al. 2001, A&A, 378, 756
Guseva, N. G., Papaderos, P., Izotov, Y. I., et al. 2003, A&A, 407, 105
Hamuy, M., Walker, A. R., Suntzeff, N. B., et al. 1992, PASP, 104, 533
Haro, G. 1956, AJ, 61, 178
Heckman, T. M., Gonzalez-Delgado, R., Leitherer, C., et al. 1997, ApJ, 482, 114
Hickson, P. 1982, ApJ, 255, 382
Hirashita, H. 2000, PASJ, 52, 107
Hopkins, A. M., Schulte-Ladbeck, R. E., & Drozdovsky, I. O. 2002, AJ, 124, 862
Huang, J. H., Gu, Q. S., Ji, L., et al. 1999, ApJ 513, 215
Hunt, L. K., Mannucci, F., Testi, L., et al. 1998, AJ, 115, 2594
Hunter, D. A., & Gallagher, J. S. 1985, AJ, 90, 1457
Iglesias-Páramo, J., & Vílchez, J. M. 1997, ApJ, 479, 190
Iglesias-Páramo, J., & Vílchez, J. M. 2001, ApJ, 550, 211
Izotov, Y. I., & Thuan, T. X. 1998, ApJ, 500, 188
Izotov, Y. I., & Thuan, T. X. 1999, ApJ, 511, 639
Izotov, Y. I., Thuan, T. X., & Lipovetski, V. A. 1994, ApJ, 435, 647
Izotov, Y. I., Thuan, T. X., & Lipovetski, V. A. 1997a, ApJS, 108, 1
Izotov, Y. I., Foltz, C. B., Green, R. F., Guseva, N. G., & Thuan, T. X. 1997b, ApJ, 487, L37
Izotov, Y. I., Chaffee, F. H., Foltz, C. B., et al. 1999, ApJ, 527, 757
Izotov, Y. I., Papaderos, P., Guseva, N. G., Fricke, K. J., & Thuan, T. X. 2004, A&A 421, 539
Jamet, L., Pérez, E., Cerviño, M., et al. 2004, A&A, 426, 399
Jarrett, T. H., Chester, T., Cutri, R., et al. 2000, AJ, 119, 2498
Karachentsev, I. D., Karachentseva, V. E., Huchtmeier, W. K., & Makarov, D. I. 2004, AJ, 127, 2031
Kauffmann, G., & White, S. D. M. 1993, MNRAS, 261, 921
Kazarian, M. A., & Martirossian, J. R. 2001, Ap, 44, 171
Kennicutt, R. C. Jr. 1998, ApJ, 498, 541
Klein, U., Wielebinski, R., & Thuan, T. X. 1984, A&A, 141, 241
Klein, U., Weiland, H., & Brinks, E. 1991, A&AP, 246, 323
Kniazev, A. Y., Pustilnik, S. A., Grebel, E. K., Lee., H., & Pramsku, A. G. 2004, ApJS, 153, 429
Kunth, D., & Joubert, M. 1985, A&A, 142, 411
Kunth, D., & Sargent, W. L. W. 1983, ApJ, 273, 81
Kunth, D., & Schild, H. 1986, A&A, 169, 71
Kunth, D., Sargent, W. L. W., & Kowal, C. 1981, A&AS, 44, 229
Kunth, D., Mas-Hesse, J. M., Terlevich, E., et al. 1998, A&A, 334, 11
Landolt, A. U. 1983, AJ, 88, 439
Landolt, A. U. 1992, AJ, 104, 340
Leitherer, C., Schaerer, D., Goldader, J. D., et al. 1999, ApJS, 123, 3 (STARBURST99)
Lípari, S., Terlevich, R., Díaz, R. J., et al. 2003, MNRAS, 340, 289
Loose, H.-H., & Thuan, T. X. 1986, ApJ, 309, 59
López-Sánchez, Á. R. 2006, Ph.D. Thesis, Universidad de la Laguna, Tenerife, Spain
López-Sánchez, Á. R., & Esteban, C. 2003, Rev. Mex. Astron. Astrofis. Conf. Ser., 18, 48
López-Sánchez, Á. R., Esteban, C., & Rodríguez, M. 2004a, ApJS, 153, 243
López-Sánchez, Á. R., Esteban, C., & Rodríguez, M. 2004b, A&A, 428,445
López-Sánchez, Á. R., Esteban, C., & García-Rojas, J. 2006, A&A, 449, 997
López-Sánchez, Á. R., Esteban, C., García-Rojas, J., Peimbert, M., & Rodríguez, M. 2007, ApJ, 656, 168
MacAlpine, G. M., & Lewis, D. W. 1978, ApJS, 36, 587
Maeder, A., & Meynet, G. 1994, A&A, 287, 803
Margon, B., Anderson, S. F., Mateo, M., Fich, M., & Massey, P. 1988, ApJ, 334, 597
Markarian, B. E. 1967, Afz, 3, 55M
Markarian, B. E., & Stepanian, D. A. 1984, Afz, 20, 21
Markarian, B. E., Lipovetskii, V. A., & Stepanian, D. A. 1979, Afz, 15, 363
Markarian, B. E., Stepanian, J. A., & Erastova, L. K. 1985, Afz, 23, 439
Massey, P., Strobel, K., Barnes, J. V., & Anderson, E. 1988, ApJ, 328, 315
Mazzarella, J. M., & Balzano, V. A. 1986, ApJS, 62, 751
Mazzarella, J. M., Bothun, G. D., & Boroson, T. A. 1991, AJ, 101, 2034
Mazzarrella, J. M., & Boronson, T. A. 1993, ApJS, 85, 27
Méndez, D. I. 1999, Ph.D. Thesis, Gas ionizado y formación estelar en galaxias Wolf-Rayet, Universidad de La Laguna, Spain
Méndez, D. I., & Esteban, C. 1997, ApJ, 488, 652
Méndez, D. I., & Esteban, C. 1999, AJ, 118, 2733
Méndez, D. I., & Esteban, C. 2000, A&A, 359, 493
Méndez, D. I., Esteban, C., & Balcells, M. 1999a, AJ, 117, 1229
Méndez, D. I., Cairós, L. M., Esteban, C., & Vílchez, J. M. 1999b, AJ, 117, 1688
Meurer, G. R., Hanish, D. J., Ferguson, H. C., et al. 2006, ApJS, 165, 307
Meyer, M. J., Zwaan, M. A., Webster, R. L., et al. 2004, MNRAS, 350, 1195
Moles, M., García-Pelayo, J. M., del Río, G., & Lahulla, F. 1987, A&A, 186, 77
Noeske, K. G., Iglesias-Páramo, J., Vílchez, J. M., Papaderos, P., & Fricke, K. J. 2001, A&A, 371, 806
Noeske, K. G., Papaderos, P., Cairós, L. M., & Fricke, K. J. 2003, A&A, 410, 481
Noeske, K. G., Papaderos, P., Cairós, L. M., & Fricke, K. J. 2005, A&A, 429, 115
Osterbrock, D. E., & Cohen, R. D. 1982, ApJ, 261, 64

Pérez-Montero, E. 2002, Ph.D. Thesis, Diagnóstico de galaxias H II en el rojo lejano, Universidad Autónoma de Madrid
Perryman, M. A. C., Longair, M. S., Allington-Smith, J. R., & Fielden, J. 1982, MNRAS, 201, 957
Pindao, M., Schaerer, D., González-Delgado, R. M., & Stasińska, G. 2002, A&A, 394, 443
Popescu, C. C., & Hopp, U. 2000, A&AS, 142, 247
Prugniel, P., & Heraudeau, P. 1998, AAPS, 128, 299
Pustilnik, S. A., Kniazev, A. Y., Lipovetsky, V. A., & Ugryumov, A. V. 2001, A&A, 373, 24
Pustilnik, S., Kniazev, A., Pramskij, A., et al. 2004, A&A, 419, 469
Richter, O.-G. 1987, A&AS, 67, 237
Richter, O.-G. 1989, A&AS, 77, 237
Salzer, J. J., MacAlpine, G. M., & Boroson, T. A. 1989a, ApJS, 70, 447
Sanders, D. B., Soifer, B. T., Elias, J. H., et al. 1988, ApJ, 325, 74
Schaerer, D., & Vacca, W. C. 1998, ApJ, 497, 618
Schaerer, D., Contini, T., & Pindao, M. 1999, A&AS, 136, 35
Schaerer, D., Guseva, N. G., Izotov, Yu. I., & Thuan, T. X. 2000, A&A, 362, 53
Schlegel, D. J., Finkbeiner, D. P., & Davis, M. 1998, ApJ, 500, 525
Schombert, J. M., Wallin, J. F., & Struck-Marcell, C. 1990, AJ, 99, 497
Smith, M. G., Aguirre, C., & Zemelman, M. 1976, ApJS, 32, 217
Springel, V., White, S. D. M., Jenkins, A., et al. 2005, Nature, 435, 629
Stepanian, J. 1994, IAU Symp., 161, Astronomy from Wide-Field Imaging, 161, 731
Stevens, I. R., & Strickland, D. K. 1998, MNRAS, 301, 215
Takase, B., & Miyauchi-Isobe, N. 1992, PNAOJ, 2, 399
Taylor, C., Thomas, D., Brinks, E., & Skillman, E. D. 1996, ApJS, 107, 143
Telles, E., & Terlevich, R. J. 1995, MNRAS, 275, 1
Telles, M., Melnick, J., & Terlevich, R. 1997, MNRAS, 288, 78
Tereshchenko, V. M. 2002, AR, 46, 224
Thuan, T. X. 1991, in Massive stars in starbursts, ed. C. Leitherer, N. R. Walborn, T. M. Heckman, & C. A. Norman (Cambridge: Cambridge University Press), 183
Thuan, T. X., & Izotov, Y. I. 2005, ApJS, 161, 240
Thuan, T. X., Izotov, Y. I., & Lipovetsky, V. A. 1995, ApJ, 445, 108
Thuan, T. X., Lipovetski, V. A., Martin, J.-M., & Pustilnik, S. A. 1999, A&AS, 139, 1
Tran, H. D., Sirianni, M., Ford, H. C., et al. 2003, ApJ, 585, 750
Vacca, W. D., & Conti, P. S. 1992, ApJ, 401, 543
van der Hucht, K. A. 2001, 7th Catalog of Galactic Wolf-Rayet stars, NAR, 45, 135
van Zee, L., Salzer, J. J., & Skillman, E. D. 2001, AJ, 122, 121
Vanzi, L., Hunt, L. K., & Thuan, T. X. 2002, A&A, 390, 481
Verdes-Montenegro, L., Yun, M. S., Williams, B. A., et al. 2001, A&A, 377, 812
Verdes-Montenegro, L., del Olmo, A., Iglesias-Páramo, J. I., et al. 2002, A&A, 396, 815
Villar-Martín, M., Cerviño, M., & González-Delgado, R. M. 2004, MNRAS, 355, 1132
Vorontsov-Velyaminov, B. A. 1959, Atlas and Catalog of Interacting Galaxies, Sternberg Institute, Moscow: Moscow State University
Vorontsov-Velyaminov, B. A. 1977, A&AS, 28, 1
Vorontsov-Velyaminov, B. A., & Arkhipova, V. P. 1964, Morphological Catalogue of galaxies, Volume II, Moscow: Moscow State University
Vorontsov-Velyaminov, B. A., & Arkhipova, V. P. 1968, Morphological Catalogue of galaxies, Volume IV, Moscow: Moscow State University
Wamsteker, W., Prieto, A., Vitores, A., et al. 1985, A&AS, 62, 255
Wiklind, T. 1989, A&A, 219, L11
Wilcots, E. M., Lehman, C., & Miller, B. 1996, AJ, 111, 1575
York, D. G., Adelman, J., Anderson, J. E., Jr., et al. 2000, AJ, 120, 1579
Zamorano, J., Rego, M., Gallego, J. G., et al. 1994, ApJS, 95, 387
Zamorano, J., Gallego, J., Rego, M., Vitores, A. G., & Alonso, O. 1996, ApJS, 105, 343
Zhang, W., Kong, X., Li, C., Zhou, H.-Y., & Cheng, F. Z. 2007, ApJ, 655, 851
Zwicky, F. 1971, Catalogue of Selected Compact Galaxies and Post-Eruptive Galaxies, Guemligen
Zwicky, F., & Herzog, E. 1966, Catalogue of galaxies and of clusters of galaxies, Volume III (Pasadena: California Institute of Technology (CIT))
Zwicky, F., & Kowal, C. T. 1968, Catalogue of Galaxies and of Clusters of Galaxies, Volume VI (Pasadena: California Institute of Technology)

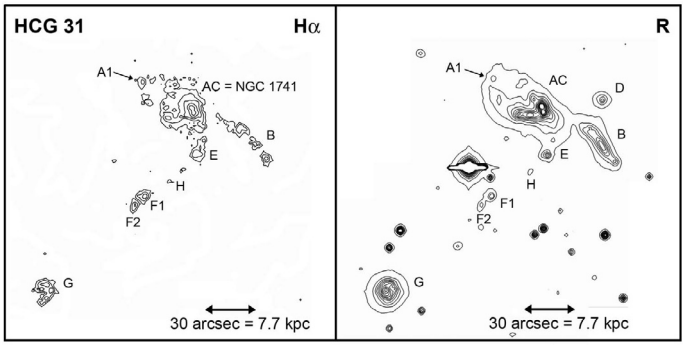

Fig. 1. Contour maps of HCG 31 in net-Hα (*left*) and *R* (*right*). The identification of the regions follows the notation given by López-Sánchez et al. (2004a).

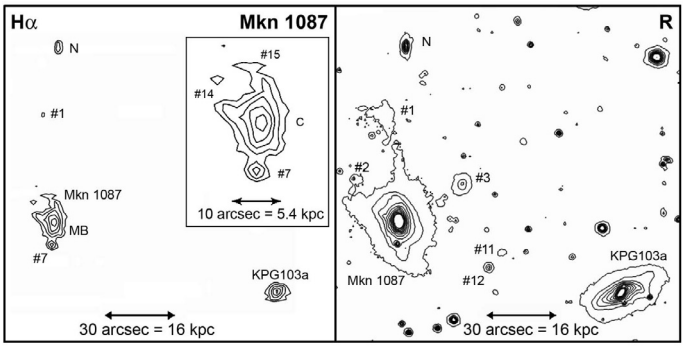

Fig. 2. Contour maps of Mkn 1087 in net-Hα (*left*) and *R* (*right*). The identification of the regions follows the notation given by López-Sánchez et al. (2004b).

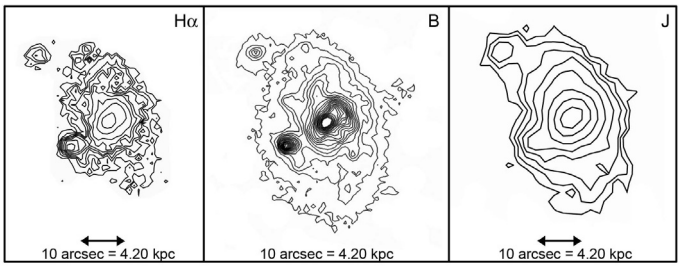

Fig. 4. Contour maps of Haro 15 in net-Hα, *B* and *J*.

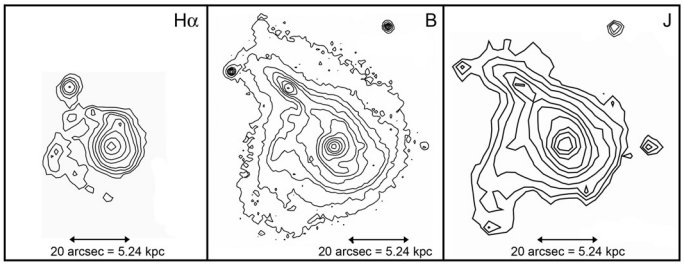

Fig. 6. Contour maps of Mkn 1199 in net-Hα, *B* and *J*.

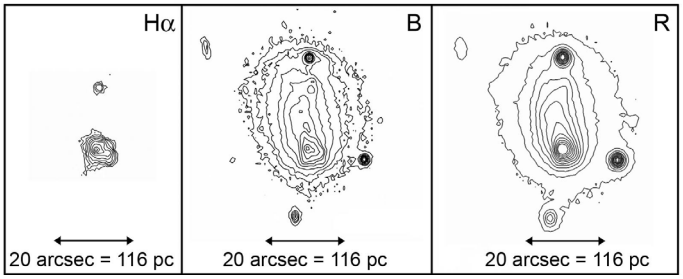

Fig. 8. Contour maps of Mkn 5 in net-Hα, *B* and *R*.

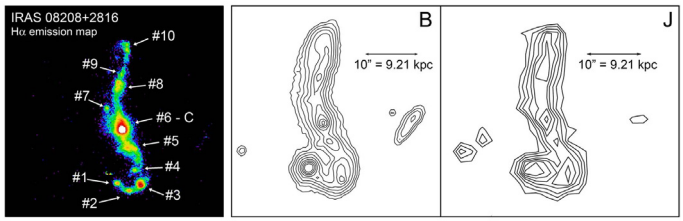

Fig. 10. (*Left*) Continuum-subtracted Hα map indicating all the star-forming regions within IRAS 08208+2816. (*Right*) Contour maps in *B* and *J* bands.

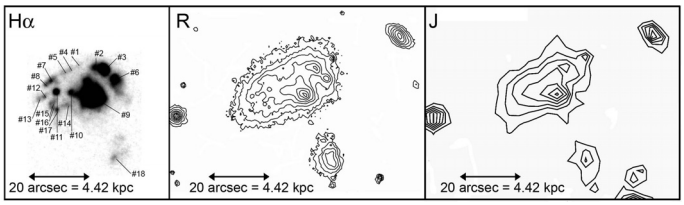

Fig. 12. (*Left*) Continuum-subtracted Hα image indicating all regions identified by Méndez & Esteban (1999) (it is their Fig. 1). (*Right*) Contour maps of POX 4 in *R* and *J* bands.

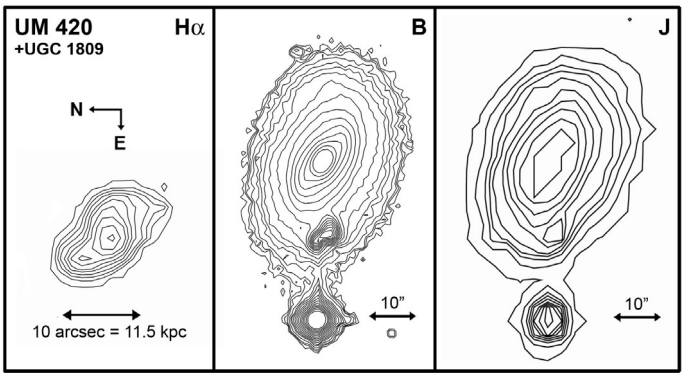

Fig. 14. Contour maps of UM 420 in net-Hα, *B* and *J* images. Notice that the Hα contour map has a differente scale. North is at the left in the three maps.

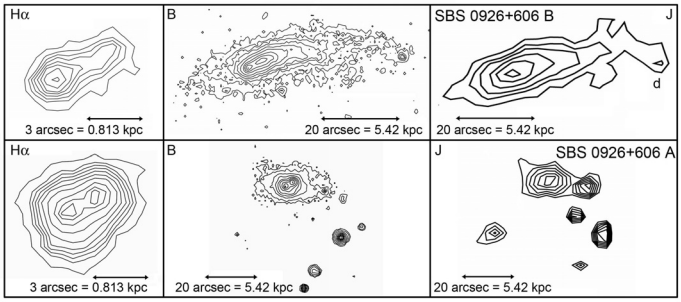

Fig. 16. Contour maps of SBS 0926+606 A (*down*) and B (*top*) in net-Hα, *B* and *J*. Note that the Hα contour maps have a different scale.

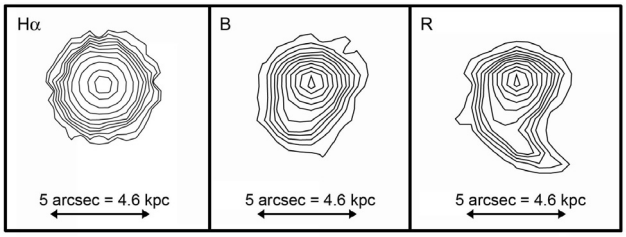

Fig. 18. Contour maps of SBS 0948+532 in Hα, *B*, and *R*. Note that the seeing of the Hα image (~1.4″) is more than twice as good as that of the broad-band filters (~0.6″).

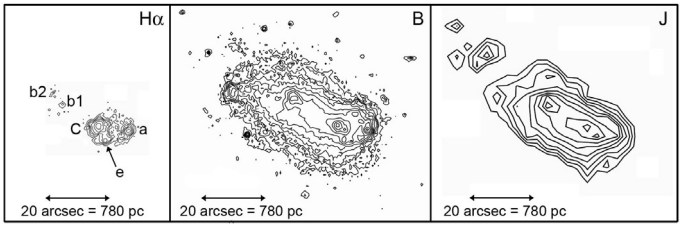

Fig. 20. Contour maps of SBS 1054+365 in net-Hα, *B* and *J*.

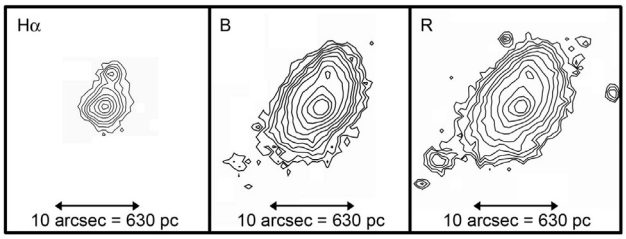

Fig. 22. Contour maps of SBS 1211+540 in net-Hα, *B* and *R*.

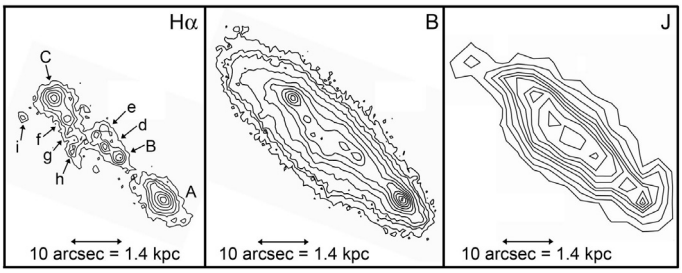

Fig. 24. Contour maps of SBS 1319+579 in net-Hα, *B* and *J*.

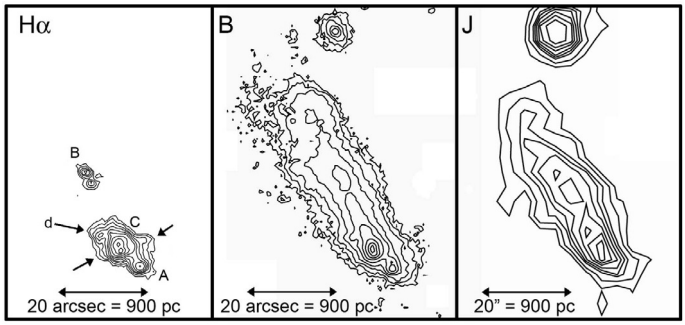

Fig. 26. Contour maps of SBS 1415+437 in net-Hα, *B* and *J*.

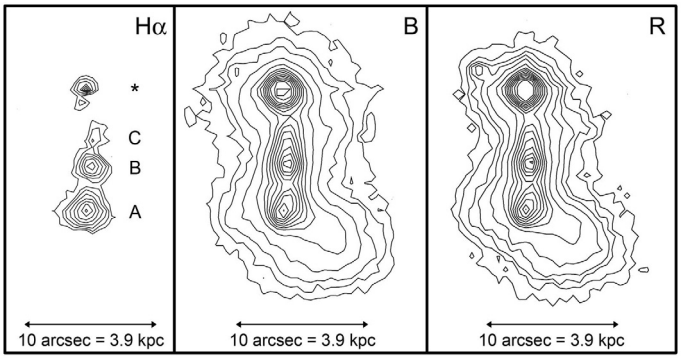

Fig. 28. Contour maps of III Zw 107 in net-Hα, *B* and *R*. Three regions are identified in the Hα map. The northern star could not be well subtracted in the net-Hα map because of its brightness.

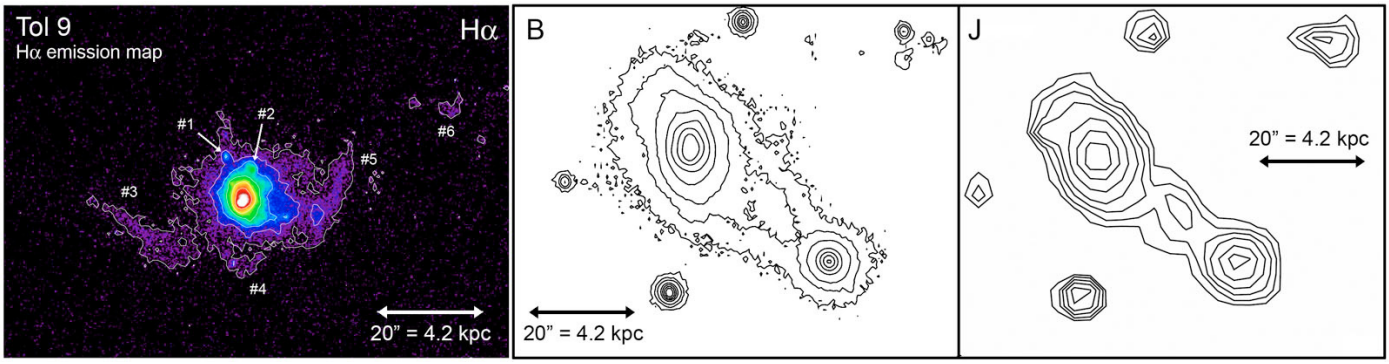

Fig. 30. (*Left*) Continuum-subtracted Hα map of Tol 9 indicating the main regions. (*Right*) Contour maps in *B* and *J*.

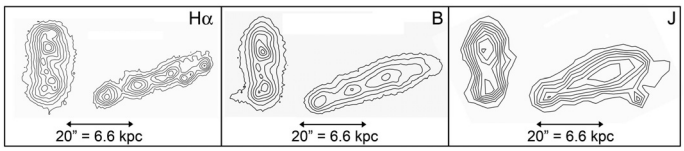

Fig. 32. Contour maps of Tol 1457-262 in net-Hα, *B* and *J*. The external isophote corresponds to 3σ over the sky level.

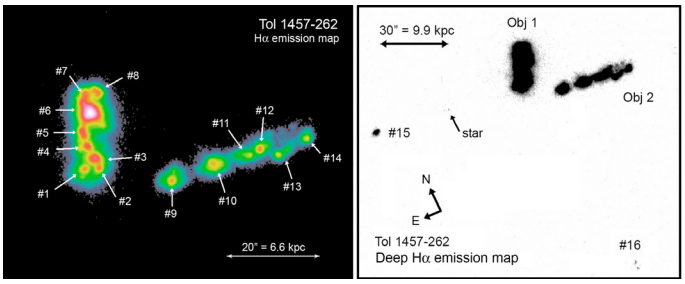

Fig. 33. (*Right*) Continuum-subtracted Hα emission map of Tol 1457-262 and its surroundings. Objects #15 and #16 also host nebular emission. The faint residual image of a bright star (*star*) is also evident. (*Left*) Detail of the Hα emission within the two main objects, identifying all their knots.

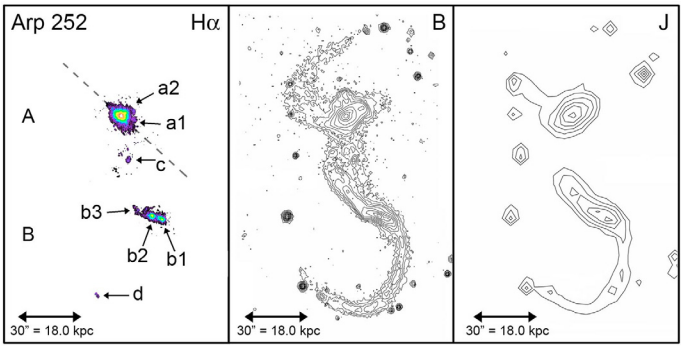

Fig. 35. (*Right*) Contour maps of Arp 252 in *B* and *J* filters. The external isophote corresponds to the 2.5σ detection significance level over the sky level. (*Left*) Continuum-subtracted Hα emission map indicating the most important regions. The main axis of the Hα emission in A is indicated with an discontinuous line and it is almost perpendicular to the main axis of the galaxy.

Table 2. Journal of observations for broad-band optical filters. All exposure times are provided in seconds. Note that in some cases there are several observations per filter. Dates follow the format year/month/day.

Galaxy	*U*			*B*			*V*			*R*		
	Tel.	Date	T. exp	Tel.	Date	T. exp	Tel.	Date	T. exp	Tel.	Date	T. exp
HCG 31	NOT	02/10/23	3×300	NOT	02/10/23	3×300	NOT	02/10/23	4×300	INT	03/09/22	2×200
Mkn 1087	NOT[a]	97/02/06	3×300	NOT	03/01/20	3×300	2CAHA	00/12/19	3×1200	NOT	03/01/20	6×300
Mkn 1199	INT	05/11/19	3×300	2CAHA	04/11/07	3×300	2CAHA	00/12/19	5×400	2CAHA	04/11/07	3×300
	NOT	06/01/07	2×60	INT	05/11/19	3×300	NOT	06/01/07	3×60			
Mkn 5	NOT	04/01/20	3×300	NOT	04/01/20	3×300	NOT	04/01/20	3×300	NOT	05/04/05	3×300
Haro 15	INT	05/11/19	4×300	INT	05/11/19	3×300	2CAHA	00/12/19	3×1200	2CAHA	04/11/06	3×300
	NOT	06/01/07	2×60	NOT	06/01/07	2×60	NOT	06/01/07	2×60			
POX 4	NOT[a]	97/02/06	3×400	NOT[a]	97/02/06	3×300	NOT[a]	97/02/06	3×300	NOT	05/04/03	3×300
UM 420	INT	05/10/06	3×300	INT	05/10/06	3×300	INT	05/10/06	3×300	2CAHA	04/11/06	3×300
IRAS 08208+2816	NOT	04/01/20	3×300	NOT	04/01/20	3×300	NOT	04/01/20	3×300	NOT	05/04/05	3×300
							2CAHA	00/12/19	3×1200			
IRAS 08339+6517	NOT	05/04/03	3×300	NOT	05/04/03	3×300	NOT	04/03/20	2×300	NOT	04/03/20	3×300
SBS 0926+606A	NOT	04/01/20	3×300	NOT	04/01/20	3×300	NOT	04/01/20	3×300	2CAHA	04/11/07	3×300
SBS 0948+532	NOT	05/04/05	3×300	NOT	05/04/03	3×300	NOT	05/04/03	3×300	NOT	05/04/03	3×300
SBS 1054+365	NOT	04/01/20	3×300	NOT	04/01/20	3×300	NOT	04/01/20	3×300	...	...	...
							2CAHA	00/12/19	3×1200			
SBS 1211+540	NOT	05/04/04	3×300	NOT	05/04/04	3×300	NOT	05/04/04	3×300	NOT	05/04/04	3×300
SBS 1319+579	NOT	04/03/20	3×300	NOT	04/03/20	3×300	NOT	04/03/20	3×300	NOT	05/04/03	3×300
SBS 1415+437	NOT	05/04/03	3×300	NOT	05/04/03	3×300	NOT	05/04/03	3×300	NOT	05/04/03	3×300
III Zw 107	INT	05/10/06	3×300	2CAHA	04/11/07	3×300	2CAHA	04/11/07	3×300	INT	05/10/06	3×300
				INT	05/10/06	3×300						
Tol 9	NOT	05/04/05	3×300	NOT	05/04/05	3×300	2CAHA	00/12/19	3×1200	NOT	05/04/05	3×300
Tol 1457-262a	NOT	05/04/03	3×300	NOT	04/03/20	3×300	NOT	04/03/20	3×300	NOT	05/04/03	3×300
Arp 252	NOT	04/03/20	3×300	NOT	04/03/20	3×300	NOT	04/03/20	3×300	NOT	05/04/04	3×300
							2CAHA	00/12/19	3×1200			

[a] Images published by Méndez & Esteban (2000).

Table 3. Log of our *NIR* observations, all completed at CST. Dates follow the format year/month/day.

	J		*H*		K_s	
Galaxy	Date	$N \times$ Exp. Time (s)	Date	$N \times$ Exp. Time (s)	Date	$N \times$ Exp. Time (s)
HCG 31	03/02/04	120×20	03/02/04	240×10	03/02/04	360×5
Mkn 1087	02/09/24	120×20	02/09/24	240×10	02/09/24	360×5
Haro 15	02/09/24	120×20	02/09/24	240×10	02/09/24	360×5
Mkn 1199	03/02/04	120×20	03/02/04	120×10	03/02/04	360×5
Pox 4	04/02/03	180×20	05/05/23	240×10	05/05/23	240×5
UM 420	04/02/02	240×20	04/02/03	360×10	04/02/03	240×5
IRAS 08208+2816	03/03/29	120×20	03/03/29	240×10	03/02/04	240×5
SBS 0926+606A	03/03/26	180×20	03/03/26	360×10	03/03/28	480×5
SBS 1054+365	03/03/28	120×20	03/03/28	360×10	03/03/28	360×5
SBS 1319+579	04/02/02	120×20	04/02/28	240×10	04/02/28	360×5
SBS 1415+437	03/03/26	180×20	03/03/28	360×10	03/03/29	240×5
Tol 9	04/02/03	180×20	04/02/03	360×10	05/04/24	240×5
Tol 1457-262a	04/04/18	120×20	04/04/18	240×10	04/04/19	240×5
Arp 252	04/02/01	180×20	04/02/01	240×10	...	...

Table 4. Log of the Hα observations. Times are indicated in seconds. Dates follow the format year/month/day.

Galaxy	Telescope	Date	Hα Filter	Time	K	Hα cont. Filter	Time	K	Seeing[a] ($''$)
HCG 31	2.2CAHA	04/11/06	667/8	4×300	1.44	683/9	1×300	1.37	1.1
Mkn 1087	2.2CAHA	04/11/06	674/7	4×300	1.21	727/16	2×300	1.23	1.3
Haro 15	2.2CAHA	04/11/06	667/8	3×300	1.65	683/9	1×300	1.73	1.5
Mkn 1199	2.2CAHA	00/12/20	667/8	3×600	1.03	613/12	3×600	1.00	2.2
Mkn 5	NOT	05/04/04	IAC-20	3×300	1.54	IAC-36	2×300	1.55	0.8
POX 4[b]	NOT	97/02/04	IAC-24	3×900	–	NOT-21	3×600	–	1.2
UM 420	2.2CAHA	04/11/06	696/15	3×300	1.26	667/8	1×300	1.30	1.0
IRAS 08208+2816	NOT	04/01/20	IAC-36	3×300	1.02	NOT-21	3×300	1.00	0.6
IRAS 08339+6517	NOT	04/03/20	IAC-19	3×300	1.25	IAC-20	2×300	1.26	0.6
SBS 0926+606A	2.2CAHA	04/11/07	667/8	3×300	1.12	683/9	1×300	1.10	1.4
SBS 0948+532	NOT	05/04/05	IAC-36	3×300	1.10	IAC-19	2×300	1.11	1.4
SBS 1054+365	NOT	04/01/20	NOT-21	4×300	1.06	–	–	–	–
	NOT	04/03/20	–	–	–	IAC-36	2×300	1.04	0.7
SBS 1211+540	NOT	05/04/04	IAC-20	3×300	1.16	IAC-36	2×300	1.19	0.6
SBS 1319+579	NOT	04/03/20	IAC-12	3×300	1.18	IAC-36	2×300	1.20	0.7
	NOT	05/04/03	IAC-12	4×300	1.15	IAC-36	2×300	1.14	0.8
SBS 1415+437	NOT	05/04/03	IAC-20	3×300	1.06	IAC-36	2×300	1.08	0.6
III Zw 107	2.2CAHA	04/11/06	667/8	3×300	1.03	683/9	1×300	1.05	1.0
Tol 9	NOT	06/04/26	IAC-24	3×900	1.85	IAC-36	3×300	2.00	0.9
Tol 1457-262a	NOT	04/03/20	IAC-20	3×300	1.80	IAC-19	3×300	1.85	1.0
Arp 252	NOT	04/01/20	IAC-39	4×300	1.52	IAC-36	3×300	1.55	0.7

[a] The worst value for the seeing is indicated; [b] images from Méndez & Esteban (2000).

Table 5. Results for the broad-band optical/*NIR* photometry of our WR galaxies sample. $E(B-V)$ was determined from the $C(\mathrm{H}\beta)$ calculated from our optical spectra. All magnitudes and colors have been corrected for extinction; optical colors have been also corrected for the emission of the ionized gas. Except for NGC 5253, absolute magnitudes were computed using the distances provided by our optical spectra. See figures for the identification of the different regions inside galaxies.

Object	$E(B-V)$	m_B	M_B	$U-B$	$B-V$	$V-R$	$V-J$	$J-H$	$H-K_s$
HCG 31[d]									
AC[c,d]	0.06 ± 0.02	14.17 ± 0.05	−19.43 ± 0.05	−0.60 ± 0.06	0.03 ± 0.08	0.12 ± 0.08	0.20 ± 0.10	0.13 ± 0.10	0.15 ± 0.12
B[c]	0.18 ± 0.04	14.89 ± 0.05	−18.71 ± 0.05	−0.38 ± 0.08	0.17 ± 0.06	0.06 ± 0.06	0.14 ± 0.10	0.13 ± 0.10	0.12 ± 0.10
E[c]	0.06 ± 0.03	17.84 ± 0.06	−15.76 ± 0.06	−0.65 ± 0.10	−0.03 ± 0.10	0.20 ± 0.09	0.29 ± 0.12	0.05 ± 0.10	0.18 ± 0.12
F1[c]	0.20 ± 0.03	17.84 ± 0.06	−15.76 ± 0.06	−0.99 ± 0.12	−0.07 ± 0.12	−0.04 ± 0.10	−0.17 ± 0.14	0.04 ± 0.17	0.29 ± 0.30
F2[c]	0.09 ± 0.03	19.26 ± 0.06	−14.34 ± 0.06	−1.01 ± 0.12	−0.09 ± 0.12	−0.02 ± 0.10	0.01 ± 0.16	0.08 ± 0.30	0.20 ± 0.50
G[c]	0.06 ± 0.03	14.72 ± 0.05	−18.88 ± 0.05	−0.43 ± 0.09	−0.01 ± 0.08	0.14 ± 0.08	0.45 ± 0.08	0.12 ± 0.10	0.13 ± 0.10
AC_{UC}	0.06 ± 0.02	...	...	−0.38 ± 0.12	0.19 ± 0.10	0.29 ± 0.12	0.69 ± 0.14	0.53 ± 0.16	0.17 ± 0.16
B_{UC}	0.18 ± 0.04	...	...	−0.27 ± 0.12	0.31 ± 0.08	0.23 ± 0.08	0.72 ± 0.10	0.61 ± 0.14	0.19 ± 0.16
G_{UC}	0.06 ± 0.02	...	...	−0.33 ± 0.10	0.28 ± 0.08	0.30 ± 0.08	0.79 ± 0.10	0.52 ± 0.14	0.23 ± 0.16
Mkn 1087[d]	0.17[a]	13.08 ± 0.04	−22.15 ± 0.04	−0.41 ± 0.08	0.17 ± 0.08	0.20 ± 0.08	0.52 ± 0.06	0.20 ± 0.06	0.16 ± 0.06
C[c]	0.14 ± 0.02	14.62 ± 0.03	−20.61 ± 0.03	−0.57 ± 0.06	−0.02 ± 0.06	0.11 ± 0.06	0.31 ± 0.10	0.15 ± 0.10	0.15 ± 0.10
N Comp[c]	0.10 ± 0.02	17.17 ± 0.03	−18.06 ± 0.03	...	−0.05 ± 0.06	0.14 ± 0.10	0.21 ± 0.08	0.18 ± 0.08	0.13 ± 0.08
#1	0.07[a]	18.89 ± 0.05	−16.34 ± 0.05	−0.75 ± 0.15	−0.01 ± 0.10	0.10 ± 0.08	...	...	...
#3	0.07[a]	18.03 ± 0.03	−17.20 ± 0.03	0.08 ± 0.30	0.11 ± 0.06	0.26 ± 0.06	0.64 ± 0.10	0.50 ± 0.20	...
UC	0.17[a]	...	...	...	0.27 ± 0.08	0.29 ± 0.08	0.82 ± 0.10	0.59 ± 0.14	0.27 ± 0.16
Haro 15[c]	0.11[a]	13.82 ± 0.04	−20.87 ± 0.04	−0.52 ± 0.08	0.26 ± 0.08	0.32 ± 0.08	0.17 ± 0.08	0.58 ± 0.08	0.22 ± 0.08
A[c]	0.23 ± 0.02	17.56 ± 0.04	−17.13 ± 0.04	−0.86 ± 0.10	−0.10 ± 0.08	0.13 ± 0.08	0.20 ± 0.08	0.24 ± 0.08	0.18 ± 0.10
B	0.04 ± 0.02	17.72 ± 0.04	−16.97 ± 0.04	−0.39 ± 0.10	0.39 ± 0.08	0.32 ± 0.08	0.54 ± 0.10	0.47 ± 0.08	0.2 ± 0.1
C[c]	0.08 ± 0.02	14.76 ± 0.04	−19.93 ± 0.04	−0.52 ± 0.08	0.29 ± 0.08	0.31 ± 0.08	0.25 ± 0.08	0.38 ± 0.08	0.22 ± 0.08
UC	0.11[a]	...	...	−0.29 ± 0.10	0.44 ± 0.08	0.37 ± 0.08	0.98 ± 0.10	0.56 ± 0.14	0.22 ± 0.18
Mkn 1199[c]	0.15[a]	12.98 ± 0.03	−20.68 ± 0.03	−0.44 ± 0.06	0.46 ± 0.06	0.29 ± 0.06	1.30 ± 0.07	0.55 ± 0.08	0.34 ± 0.08
MB	0.21 ± 0.02	12.99 ± 0.04	−20.67 ± 0.04	−0.53 ± 0.08	0.41 ± 0.08	0.17 ± 0.08	1.12 ± 0.08	0.55 ± 0.08	0.33 ± 0.08
Center (C)	0.21 ± 0.02	13.56 ± 0.04	−20.10 ± 0.04	−0.63 ± 0.08	0.24 ± 0.08	0.15 ± 0.08	1.17 ± 0.08	0.44 ± 0.08	0.26 ± 0.08
NE	0.11 ± 0.02	16.09 ± 0.04	−17.57 ± 0.04	0.16 ± 0.08	0.51 ± 0.08	0.34 ± 0.08	1.29 ± 0.08	0.62 ± 0.10	0.20 ± 0.12
NE c	0.11 ± 0.02	18.12 ± 0.04	−15.54 ± 0.04	−0.45 ± 0.08	0.28 ± 0.08	0.25 ± 0.08	...	...	...
e	0.12 ± 0.03[d]	18.99 ± 0.05	−14.67 ± 0.05	−0.50 ± 0.10	0.39 ± 0.10	0.15 ± 0.10	...	...	...
UC	0.15[a]	...	...	−0.12 ± 0.12	0.51 ± 0.08	0.31 ± 0.08	1.22 ± 0.12	0.65 ± 0.16	0.32 ± 0.18
Mkn 5	0.20 ± 0.02[a]	14.83 ± 0.03	−15.57 ± 0.03	−0.41 ± 0.06	0.44 ± 0.06	0.30 ± 0.06	0.81[e]	0.52 ± 0.03[e]	0.38 ± 0.04[e]
Main Body	0.20 ± 0.02[a]	15.46 ± 0.04	−14.94 ± 0.04	−0.57 ± 0.08	0.39 ± 0.08	0.21 ± 0.08	...	...	...
A[c]	0.18 ± 0.02	16.54 ± 0.04	−13.86 ± 0.04	−0.81 ± 0.08	0.10 ± 0.08	0.12 ± 0.08	...	...	...
B[d]	0.21 ± 0.02	19.13 ± 0.04	−11.27 ± 0.04	−0.48 ± 0.08	0.29 ± 0.08	0.09 ± 0.08	...	...	...
c	0.20 ± 0.02[a]	20.14 ± 0.04	−10.26 ± 0.04	−0.17 ± 0.08	0.43 ± 0.08	0.27 ± 0.08	...	...	...
UC	0.20 ± 0.02[a]	...	...	...	0.45 ± 0.08	0.30 ± 0.08	...	...	...
IRAS 08208+2816[c]	0.17 ± 0.02[a]	15.10 ± 0.03	−21.29 ± 0.03	−0.49 ± 0.06	0.22 ± 0.06	0.35 ± 0.08	1.03 ± 0.08	0.54 ± 0.08	0.22 ± 0.10
#1[c]	0.30 ± 0.03	19.15 ± 0.04	−17.24 ± 0.04	−0.52 ± 0.08	0.19 ± 0.06	0.30 ± 0.12	...	...	...
#2[c]	0.30 ± 0.03	19.22 ± 0.05	−17.17 ± 0.05	−0.55 ± 0.08	0.19 ± 0.06	0.19 ± 0.12	...	...	...
#3[c]	0.33 ± 0.02	16.80 ± 0.03	−19.59 ± 0.03	−0.50 ± 0.08	0.05 ± 0.06	0.05 ± 0.12	0.80 ± 0.12	0.51 ± 0.14	0.26 ± 0.16
#5[c]	0.28 ± 0.02	17.83 ± 0.03	−18.56 ± 0.03	−0.65 ± 0.08	0.07 ± 0.06	0.08 ± 0.12	...	...	...
#6(C)[c]	0.08 ± 0.02	16.91 ± 0.03	−19.48 ± 0.03	−0.61 ± 0.06	0.02 ± 0.06	0.24 ± 0.08	0.57 ± 0.10	0.27 ± 0.08	0.18 ± 0.10
#7[c]	0.10 ± 0.02	20.60 ± 0.03	−15.79 ± 0.03	−0.44 ± 0.06	0.37 ± 0.06	0.39 ± 0.08	...	...	...
#8[c]	0.12 ± 0.02	17.84 ± 0.03	−18.55 ± 0.03	−0.31 ± 0.06	0.30 ± 0.06	0.31 ± 0.08	1.05 ± 0.12	0.53 ± 0.12	0.28 ± 0.14
#9[c]	0.10 ± 0.02	18.42 ± 0.05	−17.97 ± 0.05	−0.20 ± 0.06	0.32 ± 0.06	0.32 ± 0.08	...	...	...
#10[c]	0.08 ± 0.02	18.04 ± 0.04	−18.35 ± 0.04	−0.20 ± 0.06	0.29 ± 0.06	0.35 ± 0.08	...	...	...
IRAS 08339+6517[c,d]	0.16 ± 0.02	12.94 ± 0.04	−21.57 ± 0.04	−0.51 ± 0.08	0.01 ± 0.08	0.26 ± 0.08	1.36 ± 0.06[e]	0.64 ± 0.05[e]	0.23 ± 0.06[e]
Companion[d]	0.13 ± 0.02	16.31 ± 0.04	−18.21 ± 0.04	−0.16 ± 0.10	0.20 ± 0.08	0.26 ± 0.08	1.45 ± 0.12[e]	0.21 ± 0.25[e]	0.68 ± 0.28[e]
POX 4[c]	0.06[d]	14.56 ± 0.01	−18.79 ± 0.01	−0.68 ± 0.03	0.29 ± 0.02	0.32 ± 0.04	0.42 ± 0.08	0.28 ± 0.08	0.15 ± 0.10
#3[c]	0.06[d]	17.88 ± 0.01	−15.41 ± 0.01	−1.00 ± 0.03	−0.06 ± 0.02	0.04 ± 0.04	0.12 ± 0.10	...	...
#6[c]	0.06[d]	18.49 ± 0.02	−14.80 ± 0.02	−0.98 ± 0.04	−0.01 ± 0.04	0.06 ± 0.06	0.08 ± 0.12	...	...
#7[c]	0.06[d]	20.69 ± 0.02	−12.60 ± 0.02	−0.88 ± 0.04	−0.09 ± 0.06	0.11 ± 0.08	...	...	...
#9 (C)[c]	0.06 ± 0.02	15.32 ± 0.01	−17.97 ± 0.01	−0.93 ± 0.03	0.32 ± 0.02	0.10 ± 0.04	0.16 ± 0.12	0.2:	0.2:
#11[c]	0.06[d]	19.19 ± 0.04	−14.10 ± 0.04	−0.65 ± 0.06	0.07 ± 0.02	0.15 ± 0.04	0.49 ± 0.14	...	...
Comp	0.12	17.93 ± 0.03	−15.36 ± 0.03	−0.02 ± 0.06	0.25 ± 0.02	0.30 ± 0.04	0.87 ± 0.10	0.7:	0.3:
UM 420	0.06 ± 0.01	17.32 ± 0.03	−19.55 ± 0.03	−0.80 ± 0.06	0.31 ± 0.06	0.13 ± 0.06[d]	0.77 ± 0.12	0.41 ± 0.12	0.12 ± 0.16
C[c]	0.06 ± 0.01	19.35 ± 0.03	−17.52 ± 0.03	−1.00 ± 0.06	0.11 ± 0.06	0.18 ± 0.06	0.38 ± 0.12	0.32 ± 0.12	0.13 ± 0.16
UGC 1809	0.04[b]	15.02 ± 0.03	−19.92 ± 0.03[e]	0.12 ± 0.06	0.49 ± 0.06	0.50 ± 0.06	1.40 ± 0.10	0.68 ± 0.12	0.28 ± 0.14
SBS 0926+606 A[c]	0.08 ± 0.02	16.45 ± 0.03	−17.29 ± 0.03	−0.75 ± 0.06	0.01 ± 0.06	0.14 ± 0.06	0.54 ± 0.06	0.21 ± 0.06	0.15 ± 0.08
A1[c]	0.08 ± 0.02	17.51 ± 0.03	−16.23 ± 0.03	−0.77 ± 0.06	−0.02 ± 0.06	0.10 ± 0.06	0.34 ± 0.08	0.18 ± 0.08	0.11 ± 0.08
A2[c]	0.08 ± 0.02	17.92 ± 0.03	−15.82 ± 0.03	−0.84 ± 0.06	−0.05 ± 0.06	0.08 ± 0.06	0.29 ± 0.08	0.18 ± 0.08	0.12 ± 0.08
A_{UC}	0.08 ± 0.02	19.15 ± 0.04	−14.59 ± 0.04	−0.20 ± 0.10	0.25 ± 0.08	0.32 ± 0.08	0.98 ± 0.10	0.57 ± 0.10	0.16 ± 0.12
SBS 0926+606 B[c]	0.12 ± 0.02	16.37 ± 0.04	−17.37 ± 0.04	−0.51 ± 0.08	0.08 ± 0.06	0.20 ± 0.06	0.83 ± 0.06	0.29 ± 0.06	0.18 ± 0.08

Table 5. continued.

Object	$E(B-V)$	m_B	M_B	$U-B$	$B-V$	$V-R$	$V-J$	$J-H$	$H-K_s$
Bc[c]	0.12 ± 0.02	18.84 ± 0.04	−14.90 ± 0.04	−0.87 ± 0.08	0.04 ± 0.06	0.11 ± 0.06	0.52 ± 0.12	...	...
B^c_{MB}	0.12 ± 0.02	17.21 ± 0.03	−16.53 ± 0.03	−0.54 ± 0.06	0.13 ± 0.06	0.16 ± 0.06	0.75 ± 0.06	0.20 ± 0.06	0.16 ± 0.08
B^c_d	0.12 ± 0.02	21.60 ± 0.12	−12.14 ± 0.12	−0.58 ± 0.20	0.06 ± 0.12	0.10 ± 0.08	0.80 ± 0.20	...	...
B_{UC}	0.12 ± 0.02	16.69 ± 0.04	−17.05 ± 0.04	−0.33 ± 0.10	0.30 ± 0.08	0.29 ± 0.08	1.10 ± 0.10	0.53 ± 0.10	0.13 ± 0.12
X	0.03[b]	24.4:[d]	...	...	2.4:	1.4 ± 0.2	4.4 ± 0.2	1.07 ± 0.14	0.65 ± 0.18
SBS 0948+532[c]	0.24 ± 0.02	17.93 ± 0.03	−18.43 ± 0.03	−1.20 ± 0.06	−0.12 ± 0.06	0.16 ± 0.06	...	...	...
$r = 1.3''$[c]	0.24 ± 0.02	18.19 ± 0.03	−18.17 ± 0.03	−0.90 ± 0.06	−0.03 ± 0.06	0.07 ± 0.06	...	...	...
$r = 2.3''$[c]	0.24 ± 0.02	17.89 ± 0.03	−18.47 ± 0.03	−1.19 ± 0.06	−0.05 ± 0.06	0.15 ± 0.06	...	...	...
Tail	0.24 ± 0.02	20.59 ± 0.05	−15.77 ± 0.05	−0.40 ± 0.20	0.28 ± 0.09	0.30 ± 0.06	...	...	...
SBS 1054+365	0.02[d]	15.46 ± 0.03	−14.06 ± 0.03	−0.34 ± 0.06	0.33 ± 0.06	...	0.92 ± 0.08	0.38 ± 0.12	0.16 ± 0.15
Main Body[e]	0.02[d]	15.83 ± 0.03	−13.69 ± 0.03	−0.45 ± 0.06	0.23 ± 0.06	...	0.72 ± 0.08	...	...
C[c]	0.02[d]	17.81 ± 0.03	−11.71 ± 0.03	−0.69 ± 0.06	−0.02 ± 0.06	...	0.22 ± 0.10	0.20:	0.14:
a[e]	0.02[d]	18.81 ± 0.03	−10.71 ± 0.03	−0.52 ± 0.06	0.19 ± 0.06	...	0.50 ± 0.12	...	...
b[c]	0.02[d]	18.47 ± 0.03	−11.05 ± 0.03	−0.52 ± 0.06	0.16 ± 0.06	...	0.79 ± 0.12	0.15:	0.10:
d	0.02[d]	19.97 ± 0.03	−9.55 ± 0.03	−0.55 ± 0.06	0.10 ± 0.06	...	0.70 ± 0.12	...	...
UC	0.02[d]	...	...	0.11 ± 0.08	0.42 ± 0.08	...	1.05 ± 0.15	0.7:	...
Comp	0.02[d]	16.84 ± 0.03	...	−0.10 ± 0.06	0.61 ± 0.06	...	...	...	...
Comp C[f]	0.02[d]	17.42 ± 0.03	...	−0.28 ± 0.06	0.49 ± 0.06	...	1.75 ± 0.08	0.66 ± 0.10	0.27 ± 0.15
SBS 1211+540[c]	0.08 ± 0.01	17.32 ± 0.03	−13.27 ± 0.03	−0.61 ± 0.06	0.04 ± 0.06	0.21 ± 0.06	...	...	...
C[c]	0.08 ± 0.01	18.67 ± 0.03	−11.92 ± 0.03	−0.89 ± 0.06	−0.03 ± 0.06	0.13 ± 0.06	...	...	...
a[c]	0.08 ± 0.01	20.53 ± 0.03	−10.06 ± 0.03	−0.71 ± 0.06	0.00 ± 0.06	0.15 ± 0.06	...	...	...
b	0.08 ± 0.01	22.4 ± 0.1	−8.2 ± 0.1	...	0.45 ± 0.15	0.48 ± 0.10	...	...	...
UC	0.08 ± 0.01	...	...	−0.21 ± 0.06	0.29 ± 0.06	0.35 ± 0.06	...	...	...
SBS 1319+579	0.02 ± 0.01	15.32 ± 0.03	−18.53 ± 0.03	−0.39 ± 0.06	0.34 ± 0.06	0.19 ± 0.06	1.03 ± 0.08	0.39 ± 0.12	0.16 ± 0.20
A[c]	0.02 ± 0.01	17.61 ± 0.03	−16.24 ± 0.03	−0.77 ± 0.06	−0.04 ± 0.06	0.02 ± 0.06	0.31 ± 0.12	0.21 ± 0.14	0.15 ± 0.20
B[c]	0.08 ± 0.02	17.41 ± 0.03	−16.44 ± 0.03	−0.45 ± 0.08	0.12 ± 0.06	0.25 ± 0.06	0.88 ± 0.12	0.28 ± 0.16	...
C[c]	0.02 ± 0.01	17.98 ± 0.03	−15.87 ± 0.03	−0.72 ± 0.06	0.02 ± 0.06	0.12 ± 0.06	0.68 ± 0.12	0.25 ± 0.16	0.20:
UC	0.02 ± 0.01	...	...	−0.15 ± 0.08	0.29 ± 0.06	0.33 ± 0.06	1.20 ± 0.20	...	...
SBS 1415+437	0.13 ± 0.02	15.32 ± 0.03	−14.52 ± 0.03	−0.47 ± 0.06	0.21 ± 0.06	0.27 ± 0.06	0.98 ± 0.08	0.35 ± 0.10	0.15:
C	0.13 ± 0.02	16.97 ± 0.03	−12.87 ± 0.03	−0.75 ± 0.06	0.01 ± 0.06	0.08 ± 0.06	0.60 ± 0.12	0.20 ± 0.14	0.1:
a	0.13 ± 0.02	19.04 ± 0.03	−10.80 ± 0.03	−0.68 ± 0.06	0.06 ± 0.06	0.12 ± 0.06	...	...	...
b	0.13 ± 0.02	19.53 ± 0.03	−10.31 ± 0.03	−0.49 ± 0.06	0.18 ± 0.06	0.31 ± 0.06	...	...	...
UC	0.13 ± 0.02	...	− ...	−0.17 ± 0.08	0.27 ± 0.06	0.38 ± 0.06	1.10 ± 0.14	...	...
bg	0.009[b]	19.69 ± 0.03	...	0.33 ± 0.08	1.35 ± 0.06	0.88 ± 0.06	1.22 ± 0.12	0.55 ± 0.14	...
III Zw 107[c]	0.21 ± 0.02	14.36 ± 0.03	−20.14 ± 0.03	−0.42 ± 0.06	0.14 ± 0.06	0.22 ± 0.06	0.62 ± 0.12	0.47 ± 0.20	0.35 ± 0.20
A[c,d]	0.47 ± 0.02	15.67 ± 0.03	−18.83 ± 0.03	−0.68 ± 0.06	−0.01 ± 0.06	0.15 ± 0.06	0.56 ± 0.12	0.36 ± 0.20	0.20 ± 0.20
B+C[c,d]	0.11 ± 0.02	15.75 ± 0.03	−18.75 ± 0.03	−0.57 ± 0.06	0.02 ± 0.06	0.18 ± 0.06	0.76 ± 0.14	0.42 ± 0.20	0.24 ± 0.20
Tail	0.21 ± 0.02	18.66 ± 0.03	−15.84 ± 0.03	−0.15 ± 0.06	0.20 ± 0.06	0.30 ± 0.06	...	...	...
UC	0.21 ± 0.02	...	...	0.06 ± 0.10	0.40 ± 0.08	0.30 ± 0.08	1.2:	...	...
Tol 9[c]	0.31 ± 0.03	13.92 ± 0.03	−19.26 ± 0.03	−0.34 ± 0.06	0.24 ± 0.06	0.22 ± 0.06	0.83 ± 0.08	0.68 ± 0.10	0.27 ± 0.12
UC	0.31 ± 0.03	...	...	0.04 ± 0.10	0.48 ± 0.08	0.33 ± 0.08	1.10 ± 0.20	...	...
Comp 1	0.07[b]	16.78 ± 0.03	−16.40 ± 0.03	0.17 ± 0.08	0.63 ± 0.06	0.39 ± 0.06	1.15 ± 0.10	0.69 ± 0.14	0.29 ± 0.16
Comp 2	0.07[b]	15.33 ± 0.03	−17.85 ± 0.03	0.29 ± 0.06	0.65 ± 0.06	0.52 ± 0.06	1.55 ± 0.10	0.73 ± 0.14	0.30 ± 0.16
Tol 1457-262									
Obj 1[c]	0.16[b]	14.44 ± 0.03	−19.73 ± 0.03	−0.56 ± 0.06	0.23 ± 0.06	0.26 ± 0.06	0.60 ± 0.10	0.51 ± 0.12	0.22 ± 0.12
A[c]	0.57	14.47 ± 0.03	−19.70 ± 0.03	−0.80 ± 0.06	0.08 ± 0.06	0.11 ± 0.06	0.30 ± 0.12	0.38 ± 0.12	0.15 ± 0.12
B[c]	0.16[b]	16.31 ± 0.03	−17.86 ± 0.03	−0.63 ± 0.06	0.13 ± 0.06	0.16 ± 0.06	0.40 ± 0.12	0.35 ± 0.12	0.19 ± 0.14
C[c]	0.16[b]	17.63 ± 0.03	−16.54 ± 0.03	−0.58 ± 0.06	0.26 ± 0.06	0.21 ± 0.06	...	...	...
d[c]	0.16[b]	17.21 ± 0.03	−16.96 ± 0.03	−0.49 ± 0.06	0.19 ± 0.06	0.11 ± 0.06	0.60 ± 0.16	...	...
UC	0.16[b]	...	...	−0.30 ± 0.14	0.31 ± 0.12	0.32 ± 0.08	1.20 ± 0.20	...	...
Obj 2[c]	0.16[b]	15.20 ± 0.03	−18.97 ± 0.03	−0.42 ± 0.06	0.34 ± 0.06	0.36 ± 0.06	0.90 ± 0.10	0.58 ± 0.12	0.27 ± 0.14
e[c]	0.16[b]	17.17 ± 0.03	−17.00 ± 0.03	−0.61 ± 0.06	0.27 ± 0.06	0.36 ± 0.06	1.10 ± 0.20	...	...
f[c]	0.16[b]	16.81 ± 0.03	−17.36 ± 0.03	−0.53 ± 0.06	0.37 ± 0.06	0.33 ± 0.06	1.30 ± 0.20	...	...
g[c]	0.16[b]	15.93 ± 0.03	−18.24 ± 0.03	−0.30 ± 0.06	0.44 ± 0.06	0.41 ± 0.06	1.20 ± 0.20	...	...
UC	0.16[b]	...	...	−0.17 ± 0.14	0.45 ± 0.12	0.53 ± 0.08	1.30 ± 0.20	...	...
#15	0.16[b]	17.69 ± 0.04	−16.48 ± 0.04	−0.25 ± 0.10	0.39 ± 0.08	0.39 ± 0.06	1.10 ± 0.20	...	...
#16	0.16[b]	19.48 ± 0.05	−14.69 ± 0.05	−0.10 ± 0.15	0.45 ± 0.10	0.40 ± 0.06	...	...	...
Arp 252[d]									
A	0.34 ± 0.02	14.69 ± 0.03	−20.88 ± 0.03	−0.48 ± 0.06	0.31 ± 0.06	0.19 ± 0.06	1.10 ± 0.10	0.60 ± 0.12	0.38 ± 0.14[e]
Aa1[c]	0.34 ± 0.02	15.27 ± 0.03	−20.30 ± 0.03	−0.67 ± 0.06	0.08 ± 0.06	0.14 ± 0.06	0.95 ± 0.10	0.48 ± 0.12	...
Aa2	0.34 ± 0.02	17.77 ± 0.03	−17.80 ± 0.03	−0.50 ± 0.06	0.12 ± 0.06	0.17 ± 0.06	1.10 ± 0.20	...	...
c	0.34 ± 0.02	19.89 ± 0.04	−15.58 ± 0.04	−0.75 ± 0.09	0.03 ± 0.07	0.08 ± 0.06	...	...	...
At	0.34 ± 0.02	...	...	...	0.26 ± 0.08	0.24 ± 0.07	...	...	...

Table 5. continued.

Object	$E(B-V)$	m_B	M_B	$U-B$	$B-V$	$V-R$	$V-J$	$J-H$	$H-K_s$
B	0.16 ± 0.03	16.22 ± 0.03	-19.35 ± 0.03	-0.21 ± 0.08	0.49 ± 0.06	0.31 ± 0.06	1.20 ± 0.10	0.71 ± 0.16	0.34 ± 0.20^{e}
Bcen[c]	0.16 ± 0.03	16.51 ± 0.03	-19.06 ± 0.03	-0.41 ± 0.06	0.38 ± 0.06	0.30 ± 0.06	1.00 ± 0.10	0.52 ± 0.12	...
d	0.16 ± 0.03	21.65 ± 0.05	-13.92 ± 0.05	-0.35 ± 0.12	0.23 ± 0.10	0.10 ± 0.08	...	...	...
e	0.16 ± 0.03	19.45 ± 0.04	-16.12 ± 0.04	-0.31 ± 0.09	0.27 ± 0.07	0.20 ± 0.06	...	...	...
BtN	0.16 ± 0.03	17.22 ± 0.04	-18.35 ± 0.04	0.05 ± 0.10	0.43 ± 0.08	0.29 ± 0.06	1.30 ± 0.20	...	...
BtS	0.16 ± 0.03	...	...	0.20 ± 0.12	0.53 ± 0.08	0.39 ± 0.06	...	...	...
NGC 5253[c,d]	0.17 ± 0.03	10.09 ± 0.01	-17.92 ± 0.01	-0.41 ± 0.02	0.27 ± 0.02	0.21 ± 0.02	0.81 ± 0.03	0.53 ± 0.04	0.19 ± 0.05

Notes for Table 5:

[a] Average value of the $E(B-V)$ obtained in objects/regions inside the galaxy.

[b] Using the value for the Galactic extinction given by Schlegel et al. (1998).

[c] The optical colors of this object have been corrected for the emission of the ionized gas, consult Table 6.

[d] Notes 1: **HCG 31** See results in López-Sánchez et al. (2004a), member AC is NGC 1741. **Mkn 1087**: see results in López-Sánchez et al. (2004b). **Haro 15**: using Cairós et al. (2001a) data. **Mkn 1199**: assuming a value similar to the near region B, that has not been analyzed by photometry but by spectroscopy. **Mkn 5**: the colors of this object should be also corrected for emission of the gas, but as we do not have spectroscopic data it was not done. $B-V$ should be slightly lower and $V-R$ slightly higher. **IRAS 08339+6517**: results extracted from López-Sánchez et al. (2006). **POX 4**: using the $E(B-V)$ derived for the central object. **UM 420**: The Hα emission in this object is very important; correcting for our Hα flux $(V-R)\sim0.25$. **SBS 0926+606 X**: the B-magnitude of this object is very uncertain. Its V and K_s magnitudes are $m_V=22.1\pm0.1$ and $m_{K_s}=15.91\pm0.12$, hence it possesses $V-K_s\sim6.2$. **SBS 0948+532**: using the values given by 2MASS, $m_J=16.86$, $m_H=15.92$ and $m_{K_s}=15.31$. **SBS 1054+365**: because of the $C(H\beta)$ derived from our spectrum gives $E(B-V)=0.01$, we use the Galactic value, $E(B-V)_G=0.02$ (Schlegel et al. 1998). **III Zw 107**: using the data for J, H and K_s provided by 2MASS. **Arp 252**: object A is ESO 566-8 and object B ESO 566-7. **NGC 5253**: optical and *NIR* magnitudes extracted from the NED and corrected for extinction using an average value of $C(H\beta)=0.24$ (see López-Sánchez et al. 2007).

[e] NOTES 2: **Mkn 5**: using the data provided by Noeske et al. (2005), who used K' instead of K_s filter. For the low-brightness underlying stellar component, they found $J-H=0.58$ y $H-K'=0.28$. **IRAS 08339+6517:** *NIR* values extracted from 2MASS, see López-Sánchez et al. (2006). **UM 420 / UGC 1809**: calculated using $V_r=7306$ km s^{-1} (given by the NED) and its derived distance, $D=97.4$ Mpc. **SBS 1054+365**: probably, the colors have a small contribution for the nebular component. **Arp 252:** $H-K_s$ color adapted from 2MASS.

[f] NOTES 3: **SBS 1054+365**: Comp C is the central region of the companion object, 2MASX J10574661+3616582.

Table 6. Correction for the contribution of the nebular emission in optical colors. Corrections have been done applying $(X-Y)_e = (X-Y) - \Delta(X-Y)$, being $(X-Y)$ the color derived from photometry, $(X-Y)_e$ the color corrected for emission lines and $\Delta(X-Y)$ the correction given in this table.

Object	$\Delta(U-B)$	$\Delta(B-V)$	$\Delta(V-R)$	$\Delta(V-J)$
HCG 31 AC	−0.04	0.12	−0.07	0.04
HCG 31 B	−0.01	0.03	−0.01	0.04
HCG 31 E	−0.05	0.07	−0.03	0.03
HCG 31 F	−0.10	0.84	−0.47	0.91
HCG 31 G	−0.04	0.11	−0.03	0.10
Mkn 1087 C	0.00	0.01	0.02	0.02
Mkn 1087 N	−0.02	0.02	−0.06	0.04
Haro 15 C	−0.03	0.03	0.00	0.04
Haro 15 ESE	0.04	0.78	−0.67	0.88
Haro 15 NE	−0.02	0.03	−0.01	0.03
Mkn 1199 C	0.00	0.00	−0.07	0.01
Mkn 5 A	−0.03	0.29	−0.18	0.40
IRAS 08208+2816	−0.01	0.20	−0.10	0.20
#1, #2, #3, #5	−0.04	0.17	−0.10	0.19
#6 (C)	−0.01	0.52	−0.47	0.62
#7, #8, #9, #10	−0.01	0.15	−0.09	0.15
IRAS 08339+6517	0.00	0.01	−0.02	0.03
POX 4[a]	−0.03	0.30	−0.05	0.40
UM 420 C	−0.04	0.35	−0.30	0.5
SBS 0926+606 A	−0.04	0.35	−0.17	0.40
SBS 0926+606 B	−0.03	0.08	−0.06	0.10
SBS 0948+532	−0.02	∼0.7	∼–0.6	...
SBS 1054+365 C	−0.14	0.45	...	0.47
SBS 1054+365 d	0.00	0.05	...	...
SBS 1211+540 C	−0.19	0.47	−0.40	...
SBS 1211+540 a[b]	−0.08	0.24	−0.20	...
SBS 1319+579 A	−0.05	∼0.7	∼–0.6	∼0.7
SBS 1319+579 B	−0.01	0.12	−0.12	0.19
SBS 1319+579 C	−0.03	0.16	−0.14	0.37
SBS 1415+437 C	−0.06	0.35	0.06	0.65
III Zw 107 A	−0.03	0.19	−0.08	0.23
III Zw 107 B+C	−0.03	0.03	−0.01	0.03
Tol 9	−0.05	0.07	0.00	0.10
Tol 1457-262[c]	−0.05	∼0.5	∼–0.4	∼0.6
Tol 1457-262 A	−0.02	∼0.2	∼–0.2	∼0.3
Arp 252 Aa1	−0.04	0.24	−0.01	0.32
Arp 252 Bcen	−0.01	0.01	−0.03	0.01
NGC 5253	−0.02	0.06	−0.02	0.04

[a] Because of the strong nebular emission in this object, all regions but the companion object have been corrected using these values; [b] these values have been also used to correct the colors of SBS 1211+540 integrating all its flux; [c] all objects (Obj 1, B, C, d, Obj 2, e, f and g) except region A.

Table 7. Results of the Hα photometry of the galaxies and regions analyzed in this work. The Hα flux is corrected for both extinction and the contribution of the [N II] emission lines. Last column shows the age of the last starbursting episode derived comparing W(Hα) with the predictions given by Leitherer et al. (1999) models.

Object	Flux	Luminosity	$M_{\rm H\,II}$	$M_\star$	*SFR*	W(Hα)	Age
	(10^{-13} erg cm^{-2} s^{-1})	(10^{40} erg s^{-1})	(10^6 $M_\odot$)	(10^6 $M_\odot$)	($M_\odot$ yr^{-1})	(Å)	(Myr)
HCG 31							
A1	0.137 ± 0.015	0.452 ± 0.049	0.067 ± 0.007	0.64 ± 0.07	0.036 ± 0.004	70 ± 30	6.8 ± 0.6
B	0.925 ± 0.078	3.05 ± 0.26	0.453 ± 0.038	8.20 ± 0.69	0.242 ± 0.020	80 ± 20	6.5 ± 0.3
AC[b]	11.00 ± 0.70	36.3 ± 2.3	5.39 ± 0.34	18.2 ± 1.2	2.88 ± 0.18	500 ± 40	4.9 ± 0.1
E	0.452 ± 0.048	1.49 ± 0.16	0.222 ± 0.024	2.62 ± 0.28	0.118 ± 0.013	180 ± 30	5.8 ± 0.2
F1	1.120 ± 0.070	3.70 ± 0.23	0.549 ± 0.034	0.87 ± 0.05	0.293 ± 0.018	1200 ± 100	3.3 ± 0.2
F2	0.406 ± 0.024	1.34 ± 0.08	0.199 ± 0.011	0.28 ± 0.02	0.106 ± 0.006	1100 ± 100	3.4 ± 0.2
G	1.95 ± 0.11	6.43 ± 0.36	0.955 ± 0.054	6.99 ± 0.39	0.511 ± 0.029	220 ± 40	5.5 ± 0.3
H	0.014 ± 0.004	0.045 ± 0.013	0.007 ± 0.002	0.02 ± 0.01	0.004 ± 0.001	420 ± 100	4.8 ± 0.2
Mkn 1087	4.78 ± 0.33	70.0 ± 4.8	10.39 ± 0.72	129 ± 9	5.56 ± 0.38	90 ± 20	6.2 ± 0.1
MB	4.48 ± 0.31	65.6 ± 4.5	9.74 ± 0.67	85 ± 6	5.21 ± 0.36	150 ± 20	6.0 ± 0.1
#1	0.025 ± 0.007	0.365 ± 0.097	0.0541 ± 0.014	0.67 ± 0.18	0.029 ± 0.008	100 ± 30	6.2 ± 0.2
#7	0.274 ± 0.015	4.01 ± 0.22	0.596 ± 0.033	2.79 ± 0.15	0.319 ± 0.017	390 ± 30	5.2 ± 0.2
N	0.155 ± 0.013	2.27 ± 0.19	0.337 ± 0.028	3.34 ± 0.28	0.180 ± 0.015	80 ± 20	6.5 ± 0.3
K	1.58 ± 0.09	23.1 ± 1.3	3.44 ± 0.20	30.1 ± 1.7	1.84 ± 0.11	180 ± 30	5.8 ± 0.2
Haro 15	4.66 ± 0.52	41.8 ± 4.7	6.21 ± 0.69	77 ± 9	3.32 ± 0.37	90 ± 20	6.3 ± 0.3
C	3.23 ± 0.42	29.0 ± 3.8	4.31 ± 0.56	53 ± 7	2.30 ± 0.30	110 ± 20	6.2 ± 0.2
A	1.27 ± 0.16	11.4 ± 1.4	1.69 ± 0.21	6.7 ± 0.8	0.91 ± 0.11	360 ± 50	4.9 ± 0.2
B	0.05 ± 0.02	0.50 ± 0.20	0.07 ± 0.03	1.8 ± 0.7	0.04 ± 0.01	60 ± 25	7.0 ± 0.8
Mkn 1199	14.0 ± 2.1	48.9 ± 7.3	7.3 ± 1.1	140 ± 21	3.9 ± 0.6	...	...
MB	13.6 ± 2.0	47.5 ± 7.0	7.1 ± 1.0	84 ± 12	3.8 ± 0.6	...	...
NE	0.259 ± 0.065	0.90 ± 0.23	0.13 ± 0.03	1.67 ± 0.42	0.07 ± 0.02	...	...
A	0.033 ± 0.010	0.12 ± 0.03	0.02 ± 0.01	0.70 ± 0.21	0.01 ± 0.00	...	...
B	0.064 ± 0.019	0.22 ± 0.07	0.03 ± 0.01	1.35 ± 0.40	0.02 ± 0.01	...	...
e	0.057 ± 0.017	0.20 ± 0.06	0.03 ± 0.01	1.20 ± 0.36	0.02 ± 0.01	...	...
Mkn 5	3.00 ± 0.08	0.582 ± 0.014	0.081 ± 0.010	0.300 ± 0.012	0.046 ± 0.011	400 ± 40	4.9 ± 0.2
A	2.96 ± 0.08	0.510 ± 0.013	0.080 ± 0.010	0.290 ± 0.011	0.040 ± 0.010	442 ± 66	4.8 ± 0.2
B	0.042 ± 0.008	0.072 ± 0.014	0.0011 ± 0.0002	0.017 ± 0.002	0.006 ± 0.001	50 ± 20	7.2 ± 0.8
IRAS 08208+2816	3.29 ± 0.27	142 ± 12	21.1 ± 1.7	166 ± 14	11.3 ± 0.9	170 ± 40	5.8 ± 0.3
#1	0.046 ± 0.004	1.97 ± 0.18	0.29 ± 0.03	1.65 ± 0.15	0.156 ± 0.014	270 ± 50	5.2 ± 0.2
#2	0.058 ± 0.004	2.52 ± 0.18	0.34 ± 0.03	2.68 ± 0.19	0.200 ± 0.014	190 ± 40	5.6 ± 0.3
#3	0.219 ± 0.011	9.46 ± 0.48	1.41 ± 0.07	8.5 ± 0.4	0.75 ± 0.04	230 ± 40	5.3 ± 0.3
#4	0.031 ± 0.004	1.32 ± 0.16	0.20 ± 0.02	1.9 ± 0.2	0.105 ± 0.013	130 ± 40	6.1 ± 0.3
#5	0.279 ± 0.021	12.1 ± 0.9	1.79 ± 0.13	8.0 ± 0.6	0.96 ± 0.07	330 ± 40	5.0 ± 0.2
#6(C)	1.29 ± 0.07	56 ± 3	8.3 ± 0.5	35.0 ± 1.9	4.43 ± 0.24	350 ± 50	5.0 ± 0.1
#7	0.032 ± 0.005	1.38 ± 0.21	0.21 ± 0.03	1.5 ± 0.2	0.110 ± 0.016	180 ± 50	5.7 ± 0.4
#8	0.170 ± 0.017	7.35 ± 0.74	1.09 ± 0.11	12.5 ± 1.3	0.58 ± 0.06	110 ± 30	6.2 ± 0.3
#9	0.067 ± 0.010	2.91 ± 0.44	0.43 ± 0.06	5.9 ± 0.9	0.23 ± 0.04	90 ± 20	6.4 ± 0.4
#10	0.106 ± 0.012	4.58 ± 0.52	0.68 ± 0.08	7.8 ± 0.9	0.36 ± 0.04	110 ± 30	6.2 ± 0.3
IRAS 08339+6517[b]	16.0 ± 0.7	120 ± 6	14.5 ± 0.7	226 ± 10	9.5 ± 0.5	110 ± 10	6.0 ± 0.2
Companion	0.28 ± 0.03	2.1 ± 0.4	0.26 ± 0.03	4.1 ± 0.5	0.17 ± 0.02	31 ± 5	6.7 ± 0.2
POX 4	15.5 ± 0.5	38.4 ± 1.2	5.70 ± 0.18	9.77 ± 0.32	3.05 ± 0.10	910 ± 5	4.5 ± 0.1
#3	0.675 ± 0.027	1.67 ± 0.07	0.25 ± 0.01	0.54 ± 0.02	0.13 ± 0.01	840 ± 10	4.6 ± 0.2
#6	0.380 ± 0.030	0.94 ± 0.07	0.14 ± 0.01	0.24 ± 0.02	0.07 ± 0.01	1110 ± 25	4.0 ± 0.2
#7	0.033 ± 0.004	0.08 ± 0.01	0.01:	0.05 ± 0.01	0.01:	415 ± 20	5.0 ± 0.2
#9-C	11.2 ± 0.4	27.8 ± 1.0	4.12 ± 0.15	7.06 ± 0.25	2.20 ± 0.08	1410 ± 5	3.1 ± 0.1
#11	0.178 ± 0.011	0.44 ± 0.03	0.07:	0.25 ± 0.02	0.04:	450 ± 10	5.0 ± 0.1
Comp	0.127 ± 0.011	0.31 ± 0.03	0.05:	0.79 ± 0.07	0.02:	320 ± 5	5.2 ± 0.2
UM 420	0.695 ± 0.043	46.8 ± 2.9	6.95 ± 0.43	13.75 ± 0.85	3.71 ± 0.23	980 ± 60	4.3 ± 0.2
SBS 0926+606 A	2.52 ± 0.12	9.43 ± 0.45	1.40 ± 0.07	3.59 ± 0.17	0.75 ± 0.04	600 ± 40	4.8 ± 0.2
A1	1.46 ± 0.11	5.46 ± 0.41	0.81 ± 0.06	2.08 ± 0.16	0.43 ± 0.03	670 ± 50	4.7 ± 0.2
A2	1.06 ± 0.09	3.96 ± 0.34	0.59 ± 0.05	1.51 ± 0.13	0.31 ± 0.03	510 ± 60	4.9 ± 0.2
SBS 0926+606 B	0.631 ± 0.056	2.36 ± 0.21	0.35 ± 0.03	4.76 ± 0.42	0.19 ± 0.02	130 ± 20	6.7 ± 0.3
Bc	0.327 ± 0.031	1.22 ± 0.12	0.18 ± 0.02	2.47 ± 0.23	0.10 ± 0.01	220 ± 40	5.9 ± 0.3
SBS 0948+532	1.86 ± 0.07	78.2 ± 2.9	11.61 ± 0.44	18.84 ± 0.71	6.21 ± 0.23	810 ± 30	4.6 ± 0.2

Table 7. continued.

Object	Flux	Luminosity	$M_{\rm H\,II}$	$M_\star$	*SFR*	W(Hα)	Age
	(10^{-13} erg cm^{-2} s^{-1})	(10^{40} erg s^{-1})	(10^6 $M_\odot$)	(10^6 $M_\odot$)	($M_\odot$ yr^{-1})	(Å)	(Myr)
SBS 1054+365	5.87 ± 0.22	0.450 ± 0.017	0.067±0.003	0.23 ± 0.01	0.036 ± 0.001	320 ± 50	5.2 ± 0.2
C	5.16 ± 0.15	0.395 ± 0.011	0.059±0.002	0.20 ± 0.01	0.031 ± 0.001	490 ± 40	4.9 ± 0.1
a	1.30 ± 0.060	0.100 ± 0.005	0.015±0.001	0.05:	0.008:	390 ± 40	5.0 ± 0.2
b1	0.062 ± 0.009	0.005 ± 0.001	...	0.02:	...	40 ± 15	9.8 ± 1.0
b2	0.062 ± 0.009	0.005 ± 0.001	...	0.02:	...	25 ± 20	11 ± 2
e	0.734 ± 0.041	0.056 ± 0.003	0.008:	0.03:	0.004:	270 ± 40	5.5 ± 0.3
SBS 1211+540	0.817 ± 0.031	0.141 ± 0.005	0.021 ± 0.001	0.05:	0.011:	640 ± 40	4.8 ± 0.2
C	0.726 ± 0.026	0.125 ± 0.004	0.019 ± 0.001	0.04:	0.010:	730 ± 50	4.7 ± 0.2
a	0.610 ± 0.030	0.105 ± 0.005	0.016 ± 0.001	0.04:	0.008:	490 ± 60	5.0 ± 0.2
SBS 1319+579	2.40 ± 0.15	2.38 ± 0.15	0.354 ± 0.022	0.78 ± 0.05	0.189 ± 0.012	620 ± 60	4.9 ± 0.2
A	1.480 ± 0.008	1.469 ± 0.008	0.2182 ± 0.0012	0.28 ± 0.02	0.117 ± 0.001	1300 ± 80	3.6 ± 0.4
B	0.107 ± 0.009	0.106 ± 0.009	0.0158 ± 0.0013	0.10 ± 0.01	0.008 ± 0.001	150 ± 30	6.5 ± 0.4
C	0.579 ± 0.041	0.575 ± 0.041	0.0854 ± 0.0060	0.28 ± 0.02	0.046 ± 0.003	320 ± 40	5.3 ± 0.3
d	0.056 ± 0.005	0.056 ± 0.005	0.0083 ± 0.0008	0.06 ± 0.01	0.004	120 ± 30	7.1 ± 0.5
e	0.024 ± 0.003	0.024 ± 0.003	0.0035 ± 0.0004	0.03	0.002	100 ± 30	7.3 ± 0.8
f	0.081 ± 0.006	0.080 ± 0.006	0.0119 ± 0.0008	0.07	0.006	220 ± 30	5.9 ± 0.4
g	0.026 ± 0.003	0.026 ± 0.003	0.0038 ± 0.0004	0.04	0.002	90 ± 30	7.3 ± 0.9
i	0.010 ± 0.002	0.010 ± 0.001	0.0015 ± 0.0002	0.02	0.001	50 ± 20	9.1 ± 1.1
SBS 1415+437	4.78 ± 0.20	0.495 ± 0.021	0.0735 ± 0.0031	0.14 ± 0.01	0.039 ± 0.002	900 ± 60	4.5 ± 0.2
Main Body	4.66 ± 0.19	0.482 ± 0.020	0.0716 ± 0.0029	0.11	0.038 ± 0.002	900 ± 60	4.5 ± 0.2
C	4.10 ± 0.16	0.424 ± 0.017	0.0630 ± 0.0025	0.10	0.034 ± 0.001	1250 ± 60	3.7 ± 0.3
A	0.465 ± 0.022	0.048 ± 0.002	0.0071 ± 0.0003	0.02	0.004	1100 ± 60	4.0 ± 0.3
B	0.121 ± 0.009	0.013 ± 0.001	0.0019 ± 0.0001	0.01	0.001	200 ± 30	6.1 ± 0.2
d	0.096 ± 0.008	0.010 ± 0.001	0.0015 ± 0.0001	...	0.001	550 ± 50	4.9 ± 0.2
III Zw 107	5.29 ± 0.24	40.1 ± 1.8	5.96 ± 0.27	73.9 ± 3.4	3.19 ± 0.15	160 ± 30	5.9 ± 0.3
A	4.22 ± 0.18	32.0 ± 1.4	4.75 ± 0.20	32.5 ± 1.4	2.54 ± 0.11	250 ± 40	5.6 ± 0.3
B	0.965 ± 0.046	7.32 ± 0.35	1.087 ± 0.052	44.4 ± 2.1	0.58 ± 0.03	80 ± 30	6.5 ± 0.5
C	0.101 ± 0.018	0.77 ± 0.14	0.114 ± 0.020	5.6 ± 1.00	0.061 ± 0.011	40 ± 20	7.6 ± 1.4
Tol 9	10.2 ± 0.7	22.9 ± 1.6	3.4 ± 0.2	27.4 ± 1.9	1.82 ± 0.13	130 ± 30	6.0 ± 0.3
C	8.5 ± 0.4	19.0 ± 1.0	2.83 ± 0.14	40 ± 2	1.51 ± 0.08	200 ± 30	5.8 ± 0.2
#1	0.027 ± 0.002	0.061 ± 0.005	0.0091 ± 0.0007	0.13 ± 0.01	0.005 ± 0.001	110 ± 30	6.1 ± 0.2
#2	0.105 ± 0.006	0.236 ± 0.013	0.035 ± 0.002	0.50 ± 0.03	0.019 ± 0.001	180 ± 30	5.8 ± 0.2
#3	0.031 ± 0.004	0.070 ± 0.009	0.0104 ± 0.0013	0.15 ± 0.02	0.006 ± 0.001	110 ± 40	6.2 ± 0.2
#4	0.020 ± 0.003	0.045 ± 0.008	0.0066 ± 0.0011	0.09 ± 0.02	0.004 ± 0.001	140 ± 40	6.0 ± 0.2
#5	0.31 ± 0.04	0.69 ± 0.09	0.102 ± 0.013	1.46 ± 0.19	0.055 ± 0.007	120 ± 40	6.1 ± 0.3
#6	0.002:	0.003:	0.0005:	0.01:	...	80 ± 30	6.3 ± 0.3
Env	0.45 ± 0.04	1.017 ± 0.09	0.151 ± 0.013	...	...	...	...
Tol 1457-262	11.4 ± 0.6	63.3 ± 3.5	9.4 ± 0.5	41 ± 2	5.0 ± 0.3	340 ± 50	5.1 ± 0.2
Obj 1	8.33 ± 0.49	46.2 ± 2.7	6.9 ± 0.4	23.4 ± 1.4	3.7 ± 0.2	430 ± 40	4.9 ± 0.2
#1	0.354 ± 0.032	1.97 ± 0.18	0.29 ± 0.03	2.09 ± 0.19	0.156 ± 0.014	190 ± 30	5.8 ± 0.3
#2	0.319 ± 0.028	1.77 ± 0.16	0.26 ± 0.02	1.59 ± 0.14	0.141 ± 0.012	230 ± 40	5.4 ± 0.3
#3(B)	0.854 ± 0.049	4.74 ± 0.27	0.70 ± 0.04	2.60 ± 0.15	0.38 ± 0.02	410 ± 40	5.0 ± 0.2
#4	0.444 ± 0.040	2.47 ± 0.22	0.37 ± 0.03	1.82 ± 0.16	0.196 ± 0.018	290 ± 40	5.2 ± 0.3
#5	0.550 ± 0.043	3.05 ± 0.24	0.45 ± 0.04	1.57 ± 0.12	0.242 ± 0.019	440 ± 50	4.9 ± 0.2
#6(A)	3.20 ± 0.22	17.8 ± 1.2	2.64 ± 0.18	8.1 ± 0.6	1.4 ± 0.1	650 ± 50	4.6 ± 0.2
#7(C)	0.621 ± 0.050	3.45 ± 0.28	0.51 ± 0.04	1.71 ± 0.14	0.27 ± 0.02	320 ± 40	5.1 ± 0.2
#8	0.482 ± 0.039	2.68 ± 0.22	0.40 ± 0.03	2.41 ± 0.19	0.212 ± 0.017	230 ± 40	5.4 ± 0.3
Obj 2	3.10 ± 0.14	17.21 ± 0.78	2.56 ± 0.12	14.4 ± 0.7	1.37 ± 0.06	250 ± 30	5.2 ± 0.2
#9	0.623 ± 0.036	3.46 ± 0.20	0.51 ± 0.03	3.8 ± 0.2	0.275 ± 0.016	180 ± 30	5.7 ± 0.2
#10	0.833 ± 0.042	4.62 ± 0.23	0.69 ± 0.03	4.2 ± 0.2	0.367 ± 0.019	230 ± 40	5.4 ± 0.2
#11	0.339 ± 0.024	1.88 ± 0.13	0.28 ± 0.02	2.60 ± 0.18	0.149 ± 0.011	140 ± 30	6.0 ± 0.3
#12	0.495 ± 0.038	2.75 ± 0.21	0.41 ± 0.03	2.16 ± 0.17	0.218 ± 0.017	270 ± 40	5.2 ± 0.2
#13	0.244 ± 0.022	1.35 ± 0.12	0.20 ± 0.02	1.76 ± 0.16	0.108 ± 0.010	150 ± 30	6.0 ± 0.2
#14	0.204 ± 0.014	1.13 ± 0.078	0.168 ± 0.012	1.32 ± 0.09	0.090 ± 0.006	170 ± 30	5.8 ± 0.2
#15	0.085 ± 0.007	0.474 ± 0.039	0.070 ± 0.006	0.80 ± 0.07	0.038 ± 0.003	90 ± 20	6.4 ± 0.4
#16	0.006 ± 0.002	0.036 ± 0.010	0.005 ± 0.002	0.10 ± 0.03	0.003 ± 0.001	60 ± 30	7.0 ± 1.0
Arp 252	4.48 ± 0.30	90.3 ± 6.1	13.4 ± 0.9	82.3 ± 4.9	7.2 ± 0.5	...	...
ESO 566-8	4.17 ± 0.28	84.1 ± 5.6	12.5 ± 0.8	45.1 ± 3.0	6.68 ± 0.45	440 ± 40	4.9 ± 0.3
a1	3.82 ± 0.19	77.0 ± 3.8	11.4 ± 0.6	37.2 ± 1.9	6.12 ± 0.30	510 ± 40	4.2 ± 0.4
a2	0.085 ± 0.007	1.72 ± 0.15	0.26 ± 0.02	0.85 ± 0.08	0.136 ± 0.012	460 ± 50	4.8 ± 0.6

Table 7. continued.

Object	Flux	Luminosity	$M_{\rm H\,II}$	$M_\star$	*SFR*	W(Hα)	Age
	(10^{-13} erg cm^{-2} s^{-1})	(10^{40} erg s^{-1})	(10^6 $M_\odot$)	(10^6 $M_\odot$)	($M_\odot$ yr^{-1})	(Å)	(Myr)
ESO 566-7	0.312 ± 0.022	6.3 ± 0.4	0.93 ± 0.07	16.8 ± 1.2	0.50 ± 0.04	90 ± 20	6.1 ± 0.2
b1	0.165 ± 0.010	3.3 ± 0.2	0.49 ± 0.03	8.9 ± 0.5	0.264 ± 0.016	130 ± 20	5.9 ± 0.2
b2	0.140 ± 0.011	2.8 ± 0.2	0.419 ± 0.033	7.5 ± 0.6	0.224 ± 0.018	80 ± 20	6.2 ± 0.2
b3	0.008 ± 0.002	0.17 ± 0.04	0.025 ± 0.007	0.44 ± 0.12	0.013 ± 0.004	50 ± 20	6.4 ± 0.3
c	0.017 ± 0.003	0.34 ± 0.06	0.051 ± 0.009	0.92 ± 0.16	0.027 ± 0.005	500 ± 100	4.5 ± 0.8
d	0.008 ± 0.003	0.16 ± 0.05	0.024 ± 0.008	0.43 ± 0.13	0.013 ± 0.004	50 ± 20	6.4 ± 0.3
NGC 5253[c]	229 ± 11	4.39 ± 0.21	0.651 ± 0.031	2.22 ± 0.11	0.348 ± 0.017	450 ± 5	5.0 ± 0.1

[a] HCG 31AC is NGC 1741.
[b] Values extracted from López-Sánchez et al. (2006).
[c] Data of the Hα flux and W(Hα) extracted from Meurer et al. (2006).

Appendix A: Reduction of the optical broad-band images

All processes concerning the data reduction and analysis were completed at the IAC following the standard procedures (trimming, bias subtraction, flat-fielding, aligning and flux calibration) completed using algorithms in the IRAF[1] environment.

The photometric calibration was obtained via observations of standard photometric Landolt (1983, 1992) stars during the night. The selected stars were usually chosen in star fields where between 3 and 6 photometric objects are located. We obtained the instrumental photometric values for each galaxy or region by integrating all the flux (counts) inside an irregular region *drawn* over the galaxy or region. The region was defined by taking into account both the average value of the sky (which was always subtracted from the flux measured in each region) and the detection threshold signal (obtained by multiplying the standard deviation of the sky by a factor between 2.5 and 3). We used the polygon defined in the *B*-filter to derive the photometric values in all filters. In many cases, several regions inside the same galaxy were analyzed. Sometimes we used the Hα emission map to define those sub-regions, and other times we simply analyzed a particular region that was clearly evident in the *B* images. Furthermore, areas lacking nebular emission were selected to estimate the properties of the low-luminosity component underlying the bursts.

Photometric errors were determined by considering the *FWHM* of the PSF (*Point Spread Function*), sky level, and the flux calibration in each case. We also considered whether small variations in the size of the region affected the photometric values. The principal uncertainty was the flux calibration, except for weak objects or small regions, for which the level and noise of the sky and/or the size of the region were very important.

We corrected al the data for extinction following the detailed procedure explained in Appendix A of López-Sánchez (2006). We used the value of $C(\mathrm{H}\beta)$ derived from our optical spectra to estimate the color excess, $E(B-V)$, and the extinction in each filter, A_X, in each case. In particular, we used the Cardelli et al. (1989) extinction law and assumed $R_V = 3.1$ to find the following useful relations:

$$A_V = 2.145 \times C(\mathrm{H}\beta), \tag{A.1}$$

$$E(B-V) = \frac{A_V}{R_V} = 0.692 \times C(\mathrm{H}\beta), \tag{A.2}$$

as well as the coefficients $A_U/A_V = 1.569$, $A_U/A_V = 1.337$ and $A_R/A_V = 0.751$. We note that we used the appropriate value of $C(\mathrm{H}\beta)$ to correct each region for extinction. For regions without spectroscopic data, we assumed an average value of the color excess obtained in other knots inside the galaxy. Extinction in galaxies with several star-forming regions was corrected by assuming an average value. For independent nearby objects, we considered the Galactic extinction given by Schlegel et al. (1998) and compiled in Table 1.

In many cases, emission lines from nebulae contaminated the photometric results in objects hosting a lot of ionized gas, which is the typical situation in H II galaxies. The contribution of the emission lines to the continuum flux depended on their equivalent widths and on the localization of the emission line with respect to the transmittance curve of the broad-band filter. We corrected the effect induced in the optical broad-band filters for the brightest emission lines following the method described by Salzer et al. (1989a), which considers:

$$\Delta m = -2.5 \times \log\left(1 - \frac{T_l \times W_l}{\Delta\lambda}\right). \tag{A.3}$$

Where T_l is the filter transmittance at the position of the emission line (*without* any redshift correction), W_l is the equivalent width of the emission line (obtained from the spectrum of the object), and $\Delta\lambda$ is the *FWHM* of the transmittance curve of the broad band filter. The emission lines that we considered were: [O II] λ3727 (*U* filter); Hγ and Hβ (*B* filter); [O III] λ4959 (*B* and *V* filters), [O III] λ5007 (*V* filter) and Hα, [N II] λ5863, [S II] λ6719, 31 (*R* filter). For the remainder of the nebular lines, this contribution was not higher than 0.01 mag, and was therefore completely negligible.

Appendix B: Reduction of the *NIR* images

Bright and dark dome flat-field exposures were taken for each filter, and were combined to obtain a good flat-field image. All the reduction processes and the analysis of the data were completed at the IAC using the standard procedures available in the IRAF package, although some reduction (almost all in the *J*-band) were completed in the telescope during the observation runs.

Although during the first *NIR* observations we observed standard stars to perform flux calibration[2], we took advantage of data from the 2MASS project to perform the flux calibration at these wavelengths, which provided excellent results in similar studies (i.e., Noeske et al. 2003, 2005). The advantage of this method is that it is independent of the airmass and the transparency of the night.

In a similar way to the correction for the optical data, we corrected the *NIR* data for extinction by assuming the color excess derived from the $C(\mathrm{H}\beta)$ obtained in our spectroscopic analysis. We assumed that $A_J/A_V = 0.282$, $A_H/A_V = 0.190$, and $A_{K_\mathrm{s}}/A_V = 0.114$. The correction for extinction in *NIR* wavelengths was insignificant (for example, the Galactic extinction was 10 times lower at 2.2 μm that at 0.55 μm) and the $J-H$ and $H-K_\mathrm{s}$ colors were usually corrected by less than 0.1 mag. Even so, the corrections were always completed in this work.

We did not corrected the *NIR* colors for the emission of ionized gas because of the lack of spectroscopic data at those wavelengths. The only important nebular lines are Paβ (*J*-band) and Brγ (*K*-band). However, to compare the colors of the galaxies with theoretical models, which only consider the contribution of the nebular continuum, it should be necessary to correct the data for the emission of the ionized gas. We estimated an average value of the emission line contribution using the results for 24 starbursts by Calzetti (1997) in the UV and *NIR* range (some of them are also WR galaxies) following the *NIR* analysis of 3 WR galaxies studied by Vanzi et al. (2002). These contributions were $\Delta(J-H) \sim -0.09$ and $\Delta(H-K_\mathrm{s}) \sim 0.05$, and are shown by an arrow in the diagrams comparing colors with the predictions given by theoretical models. No *NIR* data was corrected for this effect.

[1] IRAF is distributed by NOAO which is operated by AURA Inc., under cooperative agreement with NSF.

[2] The results of the *NIR* photometry presented in our analysis of Haro 15 (López-Sánchez & Esteban 2003), HCG 31 (López-Sánchez et al. 2004a) and Mkn 1087 (López-Sánchez et al. 2004b) were obtained calibrating the data with standard stars from Hunt et al. (1998).

Appendix C: Reduction of the Hα images

The reduction process of the Hα images was similar to that of the broad-band images. The absolute flux calibration was achieved by taking short exposures of spectrophotometric standard stars taken from Hamuy et al. (1992) or Tereshchenko (2002) at different airmasses. To obtain the continuum-subtracted Hα image, we followed the standard procedure given by Cedrés (2003) and explained in detail in López-Sánchez (2006). A scaling factor between the Hα and the continuum frames was determined using non-saturated field stars. If the *FWHM* of the PSF in both images was not similar, a Gaussian filter was applied to the image of the lower *FWHM*. The finally flux-calibrated and continuum-subtracted Hα image was then produced by subtracting the scaled, continuum frame from the Hα frame.

The Hα flux of each star-forming region was determined following the same procedure explained before for the broad-band filters. We always corrected the flux for extinction and the contribution of the [N II] $\lambda\lambda$6548, 6583 emission lines. Both quantities were derived using our spectroscopic data. Assuming a Cardelli et al. (1989) extinction law with $R_V = 3.1$, the correction for extinction was

$$F^0_{\mathrm{H}\alpha} = F_{\mathrm{H}\alpha} \times 10^{C(\mathrm{H}\beta)\times 0.703}, \tag{C.1}$$

and the [N II] contribution was computed with

$$f_{\mathrm{H}\alpha} = \frac{F^0_{\mathrm{H}\alpha} Tr_{\mathrm{H}\alpha}}{Tr_{\mathrm{H}\alpha} + Tr_{[\mathrm{N\,II}]\,\lambda6548} N_1 + Tr_{[\mathrm{N\,II}]\,\lambda6583} N_2}, \tag{C.2}$$

where $N_1 = $ [N II] λ6548/Hα, $N_2 = $ [N II] λ6583/Hα, and Tr_{el} is the transmitance of the filter at the redshifted emission line (el). This calculation was performed independently for each region/galaxy.

The errors in the Hα flux were estimated by considering the PSF-*FWHM* of the image, the sky level, flux calibration, small variations in the size of the analyzed region and errors in the C(Hβ) and [N II]/Hα ratios. The W(Hα) image was also obtained by following the standard procedure. The ionized hydrogen mass, $M_{\mathrm{H\,II}}$, was derived using the expression given by Pérez-Montero (2002),

$$M_{\mathrm{H\,II}} = 1.485 \times 10^{-35} L_{\mathrm{H}\alpha} \left(\frac{n_{\mathrm{e}}}{100}\right), \tag{C.3}$$

where n_{e} is the electron density (in cm^{-3}) derived from our spectroscopic data, $L_{\mathrm{H}\alpha} = 4\pi d^2 F_{\mathrm{H}\alpha}$ is the luminosity and the result is expressed in solar masses. The number of O7V equivalent stars was estimated considering that the contribution of 1 of these stars to the Hα luminosity is $L_{\mathrm{O7V}}(\mathrm{H}\alpha) = 1.36 \times 10^{37}$ erg s^{-1} (Schaerer & Vacca 1998). We estimated the mass of the ionized stellar cluster, $M_\star$, by applying the expression given by Díaz (1999),

$$\log M_\star = \log Q(\mathrm{H}) - [0.86 \log W(\mathrm{H}\beta) + 44.48], \tag{C.4}$$

that considers the flux of ionizing photons, $Q(\mathrm{H}) = 7.318 \times 10^{11}\ L_{\mathrm{H}\alpha}$, and the H$\beta$ equivalent width, W(Hβ) (derived from our spectroscopic data), which takes into account the evolutionary state of the stellar cluster. The Hα-based star formation rate (SFR) was estimated using the Kennicutt (1998) relation. In the majority of these objects, we compared the Hα-based SFR with the SFR derived from far-infrared (*FIR*) and/or radio data. We used the relation given by Kennicutt (1998) and the *FIR* flux to estimate SFR_{FIR}; the 60 μm monochromatic flux and the Condon (1992) relation to derive $SFR_{60\,\mu\mathrm{m}}$; and the 1.4 GHz luminosity and the Condon et al. (2002) correlation to derive $SFR_{1.4\ \mathrm{GHz}}$. The non-thermal flux at 1.4 GHz was estimated using $f_{\mathrm{H}\alpha}$ and the relation given by Dopita et al. (2002).